Optical and Morphological Studies of Alkali/Alkaline Earth Metal Co-doped Gd_2O_3:Eu Phosphors

Thesis Submitted for the award of

Doctor of Philosophy

By

Ruby Priya
(Registration No. 901612018)

Under the supervision of

Dr. O. P. Pandey

Senior Professor and Head

School of Physics and Materials Science
Thapar Institute of Engineering & Technology, Patiala
Punjab-147004

January, 2021

Declaration

This is to certify that the thesis entitled, **"Optical and Morphological Studies of Alkali/ Alkaline Earth Metal Co-doped Gd_2O_3:Eu Phosphors"** being submitted by me (**Ruby Priya**) in the partial fulfillment of the requirement for the award of the degree of DOCTOR OF PHILOSOPHY in the School of Physics and Materials Science (SPMS), Thapar Institute of Engineering & Technology (TIET), Patiala, Punjab, India is an authentic record of my own work carried out under the supervision and guidance of **Dr. O. P. Pandey**. The matter presented in the thesis has not been in part or full to any other University or Institute for the award of any other degree.

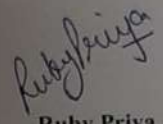

Ruby Priya

This is to certify that the above statement made by the candidate is true to the best of my knowledge.

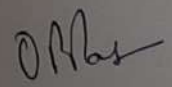

Dr. O. P. Pandey

Senior Professor and Head

School of Physics and Materials Science

Thapar Institute of Engineering & Technology

Patiala, Punjab, India-147004

Table of Contents

ACKNOWLEDGEMENT

Four years of Ph.D. would not have been a life-changing experience without the help of so many incredible individuals whom I met during this journey. It is my honor and privilege to pen down thanks to everyone who supported me during this journey and contributed to crown the final destination.

First and foremost, thank goes to my supervisor ***Dr. O. P. Pandey***, Senior Professor and Head, School of Physics and Materials Science (SPMS), Thapar Institute of Engineering & Technology, Patiala, for giving me space in his ***Functional Materials Lab***. His invaluable support, supervision, compressive and illuminating tutelage assisted at every stage of Ph.D. I consider myself fortunate to work with a very considerate and encouraging professor like him. I give deepest respect for his unwavering support and belief in me. The independence he granted me, helped me to grow as an independent researcher. I am highly thankful to him for providing me bountiful opportunities to appear in National/International events where I learned a lot. I owe my supervisor for all the accomplishments I bagged during the long journey of Ph.D. A very special thank goes to ***Mrs. Sushila Pandey*** for being constant source of moral and encouragement.

I am highly grateful to the members of my Doctoral committee, ***Dr. B. N. Chudasama***, ***Dr. B. C. Mohanty*** and ***Dr. Bonamali Pal*** for their helpful suggestions, insightful comments and discussions during progress monitoring of thesis work. They have always shown their willingness to discuss the research ideas. I bow my sincere thanks to ***Dr. B. N. Chudasama*** and ***Dr. Puneet Sharma*** for giving unlimited access to utilize their lab instruments. I extend my deepest gratitude to all the faculty members of the School of Physics and Materials Science for timely assistance whenever I required. I am also thankful to all the non-teaching staff members of SPMS for their kind help and support in administrative work.

I feel the privilege to acknowledge ***Dr. Sanjay J. Dhoble***, R.T.M. Nagpur University, Nagpur and ***Dr. Vikas Dubey***, Bhilai Institute of Technology, Raipur for their guidance, knowledge sharing and providing access to their lab facilities.

I am extremely thankful to my super seniors ***Dr. Gurbinder Kaur***, ***Dr. Deepak Kumar*** and ***Dr. Suninder Jeet*** for their guidance, discussions, scientific inputs and whole-heartedly willingness to help. I feel privileged to meet them in the initial stage of my PhD. I am highly obliged to my seniors ***Dr. Rameez Ahmad Mir*** and ***Mr. Piyush Sharma*** for their kind support,

motivation and encouragement. I am truly gratified to their prompt help whenever I looked-for. I could always look back for any support during my course of Ph.D. I appreciate the support and friendliness lab atmosphere received from my lab mates and colleagues, ***Dr. Shivani Singla, Damandeep Kaur***, ***Raveena Chaudhary***, ***Sanjay Upadhyay*** and ***Puneet Kumar Sharma, Vikasdeep Singh Mann and Varun Singhal***. I am especially thankful to ***Sandeep Kaur*** for being a moral support in the last days of thesis writing.

I am blessed and thankful to my closest acquaintances ***Swati Sharma***, ***Neeraj Sharma*** and ***Kaushlendra Pandey,*** who have always been my sides for every possible help. A very special thanks to ***Jagroop Kaur*** and ***Yashpreet*** for sharing unforgettable memories. The constant support and encouragement of ***Dr. Shivani Bhatia***, ***Dr. Nardev Bajaj, Harmanpreet Kaur***, ***Paramvir*** and ***Jeetendra Kumar Tiwari*** are highly acknowledged.

No words are adequate to express my indebtedness to my Mother ***Shmt. Sudha Rana*** and Father ***Sh. Ram Krishan Rana*** for their continuous financial and emotional support, understanding, love, affection, prayers and sacrifices. I am highly thankful to my Brother ***Harwinder Rana,*** who provided relentless encouragement, good wishes and moral support. I owe this thesis to my parents and brother.

I would like to extend my gratitude to those whom I might have missed to mention by name, who have directly and indirectly helped me to accomplish my thesis work.

Above all, I thank ***Almighty*** for bestowing ***His*** blessings, mercy and patience to conquer all the difficulties and giving me strength and courage to carry out this work.

Ruby Priya

List of Publications

From Ph.D. Work

1. **Ruby Priya**, Om Prakash Pandey, "***Photoluminescent enhancement with co-doped alkali metals in Gd_2O_3:Eu synthesized by co-precipitation method and Judd Ofelt analysis",*** Journal of Luminescence 212 (2019) 342-353.
2. **Ruby Priya**, O. P. Pandey, ***"Spectroscopic analysis of alkaline-earth metal (Mg, Ca, Sr and Ba) co-doped Gd_2O_3:Eu phosphors synthesized via co-precipitation route"*** Spectrochimica Acta Part A: Molecular and Biomolecular Spectroscopy 231 (2020) 118078.
3. **Ruby Priya**, Om Prakash Pandey, **"*Structural, morphological, luminescent and magnetic studies of CTAB and TOPO assisted Gd_2O_3:Eu phosphors synthesized via co-precipitation route"*** Journal of Alloys and Compounds 847 (2020) 156388.
4. **Ruby Priya,** O. P. Pandey, Sanjay J. Dhoble, "***Review on synthesis, structural and photo-physical properties of Gd_2O_3 phosphors for various luminescent applications***" Optics and Laser Technology 135 (2021) 106663.
5. **Ruby Priya,** Marta Michalska-Domańska, Sanjay Kumar, O.P.Pandey, ***"Morphological and optical studies of Gd_2O_3:Eu nanostructures synthesized via sacrificial template directed co-precipitation route"*** Optics and Laser Technology Optics & Laser Technology 143 (2021) 107357.

Other than Ph.D. Work

1. **Ruby Priya**, Om Prakash Pandey, ***"Hydrothermal synthesis of Eu^{3+}-doped Gd_2O_3 nanophosphors and its Judd-Ofelt analysis"***, Vacuum 156 (**2018**) 283–290.
2. **Ruby Priya,** Ishita Khurana, O. P. Pandey, "***Agro-food waste derived β-Ca_2SiO_4:Eu^{3+} phosphors for near-UV excited light emitting diodes***", Journal of Materials Science: Materials in Electronics 31 (2020) 1912-1928.
3. **Ruby Priya**, Astha Negi, Shivani Singla, O. P. Pandey, "***Luminescent studies of Eu doped $ZnAl_2O_4$ spinels synthesized by low-temperature combustion route***", Optik - International Journal for Light and Electron Optics 204 (2020) 164173.
4. Gurwinder Kaur, Piyush Sharma, **Ruby Priya**, O. P. Pandey, ***"Thermal dehydration kinetics involved during the conversion of gadolinium hydroxide to gadolinium oxide***" Journal of Alloys and Compounds 822 (2020) 153450.

5. Shivani Singla, **Ruby Priya**, Sandeep Kaur, O. P. Pandey, ***"Blue light excited novel Eu doped $CaGd_2ZnO_5$ nanophosphors: Structural and photoluminescent properties"*** Optik - International Journal for Light and Electron Optics 216 (2020) 164830.
6. **Ruby Priya**, Sandeep Kaur, Utkarsh Sharma, O. P. Pandey, Sanjay J. Dhoble, "***A review on recent progress in rare earth and transition metals activated SrY_2O_4 phosphors"*** Journal of Materials Science: Materials in Electronics 31 (2020) 13011–13027.
7. Sanjay J. Dhoble, **Ruby Priya**, N.S. Dhoble, O. P. Pandey, ***"Short review on recent progress in Mn^{4+} activated oxide phosphors for indoor plant light-emitting diodes***" Luminescence, The Journal of Biological and Chemical Luminescence (2021) 1-16.

List of Conferences/Workshops Attended

1. **Ruby Priya**, O. P. Pandey, presented poster entitled, "***Hydrothermal synthesis of Gd_2O_3 phosphors and its Judd Ofelt analysis*"** in *International Symposium on Functional Materials: Energy and Biomedical Applications (ISFM-2018),* held at Shivalik Hotel, Chandigarh, on 13-15th April, 2018.

2. **Ruby Priya**, O. P. Pandey, presented poster entitled, "***Photoluminescent enhancement with alkali and alkaline-earth metal ions co-doping in Gd_2O_3:Eu phosphors prepared by co-precipitation method*"** in *6th International Conference on Luminescence and Its Applications (ICLA-2019),* held at Pt. Ravi Shankar Shukla University, Raipur, Chhattisgarh, on 7-10th January, 2019.

3. **Ruby Priya**, O. P. Pandey, oral presentation entitled, "***Luminescent enhancement with morphology controlled Gd_2O_3:Eu phosphors*"** in *International Conference on Advanced Luminescent Materials (ICALM-2019),* held at Montreal, Canada, on 5-6th August, 2019. (*Bagged Best Oral Presentation Award*)

4. **Ruby Priya**, O. P. Pandey, oral presentation entitled, "***Luminescent and structural properties of Eu doped Gd_2O_3 phosphors for white light emitting diodes*"** in *National Conference on Science, Technology and Emerging Applications of Microscopy (STEAM-2019),* held at Dr. Bhimrao Ambedkar University, Agra, on 11-12th November, 2019.

5. **Ruby Priya**, O. P. Pandey, presented poster entitled, "***Combustion synthesis of red color emitting Eu-doped $CaGd_2ZnO_5$ phosphors*"** in *International Conference on Recent Trends in Renewable Energy and Sustainable Development (ICRTRESD-2020),* held at Bhilai Institute of Technology, Raipur, on 30-31st January, 2020. (*Bagged Best Poster Presentation Award*)

6. **Ruby Priya**, O. P. Pandey, presented poster entitled, "***Agro food waste derived Ca_2SiO_4-Eu phosphors for near UV-excited white light emitting diodes*"** in *International Workshop on Advanced Materials (IWAM-2020),* held at Ras-Al-Khamia, Dubai, on 23-25th February, 2020. (*Bagged Travel Grant Award*)

List of Tables

Chapter 6
Results and Discussion III

Chapter 7
Results and Discussion IV

List of Figures

Chapter 5
Results and Discussion II

Chapter 6
Results and Discussion III

Chapter 7
Results and Discussion IV

PREFACE

Gd_2O_3:Eu is a promising red light-emitting phosphor and holds tremendous potential applications in various optoelectronic and biomedical devices. The present research work is focused on the synthesis of Gd_2O_3:Eu phosphors via co-precipitation route and also to study the different parameters affecting its luminescent properties. The effect of synthesis parameters, doping concentration, role of alkali and alkaline-earth metal co-doping and use of different surfactants/templates on the structural, morphological, optical and luminescent properties of Gd_2O_3:Eu phosphors are studied in detail. The entire thesis work is divided into eight chapters. The state-of-art of each chapter is outlined in the following sections:

Chapter 1 describes the role of rare-earth (RE) oxide phosphors as potential host materials because of their outstanding properties such as large Stoke shifts, physical and chemical stability, long lifetimes and low phonon energy. In this chapter, various terms related to luminescence phenomena and mechanism involved are discussed. Further, luminescence in the rare-earth oxides and lanthanide ions are elucidated. At the end of the chapter, brief introduction of Gd_2O_3, its structures and applications in various fields are elaborated.

Chapter 2 summarizes the literature survey done on Eu doped Gd_2O_3 phosphors. This chapter discusses the state-of-art synthesis of Gd_2O_3:Eu phosphors and various factors affecting its luminescent characteristics. The synthesis of Gd_2O_3:Eu phosphors via different synthesis routes and their consequences on the size, morphology, and phases are discussed. The various parameters such as doping, co-doping, morphology, and phases affecting the luminescence features of the Gd_2O_3 phosphors, are discussed in detail. After peer-review of the existing literature on Gd_2O_3:Eu phosphors, the objectives of the thesis work are proposed.

Chapter 3 presents the experimental details for the synthesis of phosphors and their characterization to analyze their properties. Gd_2O_3 phosphors with varying concentrations of Eu^{3+} ions are synthesized via co-precipitation route, the details of which are discussed in this chapter. The synthesis procedures employed to synthesize the alkali and alkaline earth metals co-doped and surfactant/templates assisted Gd_2O_3:4mol%Eu phosphors have been given. The characterization techniques adopted such as X-ray diffraction (XRD), field emission scanning electron microscopy (FESEM), Fourier transform infrared spectroscopy (FTIR), UV-Visible spectroscopy, and photoluminescence (PL) techniques for structural, morphological, optical, and luminescent studies, respectively are briefly discussed in this chapter.

Chapter 4 gives an insight into the variation in the synthesis parameters that influence the different features of Gd_2O_3:Eu phosphors with alkali metal ions co-doping and their

contribution in the luminescent enhancement. The concentration of the Eu^{3+} ion in the Gd_2O_3 host lattice is varied from 1 to 5 mol%. The maximum PL intensity is obtained for the Gd_2O_3 sample with 4 mol% Eu^{3+} ion concentration, synthesized at pH 10 and calcination temperature 800 ℃, respectively. Further, different concentrations of alkali metal ions are co-doped in Gd_2O_3:4mol%Eu sample to investigate their influence on the structural, morphological, and optical properties. The photometric parameters are analyzed by calculating CIE coordinates and color-coordinated temperature (CCT) values. The radiative and Judd Ofelt parameters (Ω_2, Ω_4) of all the samples are calculated to investigate the luminescent properties further.

Chapter 5 illustrates the effect of alkaline-earth metal (AEM =Mg^{2+}, Ca^{2+}, Sr^{2+}, Ba^{2+}) co-doping on the structural, morphological, and optical properties of Gd_2O_3:Eu phosphors. The concentration of the Eu^{3+} ions is fixed 4 mol% to avoid the chances of the concentration quenching. A varying concentrations of alkali metal ions are co-doped in Gd_2O_3:4mol%Eu host lattice. The photometric parameters, such as CIE coordinates and CCT values are calculated. In order to further probe the luminescent properties and the influence of the alkaline-earth metals on the local environment of the Eu^{3+} ions in the host lattice, spectral parameters are calculated employing Judd Ofelt theory from emission spectra.

Chapter 6 illustrates the role of surfactants to engineer the morphology of and further its effects on altering the luminescent features of the Gd_2O_3:4mol%Eu phosphors. Trioctylphosphine oxide (TOPO) and cetyltrimethylammonium bromide (CTAB) are used as surfactants in different molar ratios during synthesis. The concentration of the surfactants is varied as 1:0.5, 1:1 and 1:2 i.e., metal ion to surfactant ratio during synthesis. The effect of these surfactants on the structural, morphological, and luminescent properties of Gd_2O_3:4mol%Eu phosphors has been studied. The photometric parameters such as CIE and CCT values are calculated for all the samples.

Chapter 7 describes the effect of morphology with the use of different templates and their effect on the optical and luminescent properties of the Gd_2O_3:4mol%Eu phosphors. For this purpose, three water soluble soft templates such as Thioglycerol (TG), Dextran, and Polyvinylpyrrolidone (PVP) are used during the synthesis of the phosphors. The amount of all the templates is varied from 1 to 2.5 wt% during synthesis. The effect of the templates on the structural, morphological, optical and luminescent characteristics of Gd_2O_3:4mol%Eu are studied in detail. The photometric parameters such as CIE coordinates and CCT values are calculated to check their applicability for practical applications.

Chapter 8 summarizes the results obtained in Chapter 4, 5, 6 and 7. The effects of variation in synthesis parameters, co-doping of alkali and alkaline-earth metals and use of

different surfactants/templates on the structural, morphological, optical and luminescent features of Gd_2O_3:Eu phosphors are discussed in this chapter. Based on the conclusions drawn from different findings in the present work, some suggestions to carry out future work in this field are given at the end of this chapter.

CHAPTER 1

INTRODUCTION

Overview

Rare-earth (RE) oxide phosphors are the potential host materials because of their outstanding properties such as large Stoke shifts, physical and chemical stability, long lifetimes and low phonon energy. The color tunability, high efficiency, intense and narrow emission spectra can be achieved by incorporating the lanthanide ions as dopants. Among the various rare-earth oxide phosphors, Gd_2O_3:Eu is an efficient red light-emitting phosphor and finds many applications in optoelectronic devices and also for biomedical applications. The present chapter is fundamentally distributed into three parts. Firstly, various terms and mechanisms involved in the luminescence phenomena are discussed. The second part elucidates the luminescence phenomena in the rare-earth oxides and lanthanides ions. The last section is devoted to the introduction of the Gd_2O_3 host lattice, its structure and applications in various fields.

1.1 Introduction

In the present era, luminescent materials are widely used in artificial solid-state lighting devices such as sensors, field emission displays, optoelectronic devices, cathode ray tubes, bio-sensors, etc. [1–5]. The emergent demand for these devices has imposed challenges to develop materials with proficient color emissions, narrow spectra, high efficiency, and so on. Till now, many oxides, phosphates, sulfides, chloride and fluorides have been explored to develop efficient luminescent materials with fascinating luminescent properties. In the never-ending race to get better luminescent materials, lanthanide-doped oxide materials have attracted significant attention [6–11]. The luminescent materials (phosphors) generally emit light in the visible spectral range when irradiated under different radiations such as electron beam, X-ray radiations, visible and ultraviolet light. These materials are doped with some intentionally added impurity, also known as dopants (**Fig. 1.1**). The type of impurity is based on the application to be followed. Phosphors are generally white in color to prevent the absorption of light by them. The light is emitted by the luminescence phenomena. In phosphors, energy is absorbed by the host lattice or the intentionally added impurity. It is observed that the emission spectra without dopants are often diffused. The emissions in undoped materials are accompanied by lattice defects such as Schottky and Frenkel. Thus, a dopant is required to get sharp, intense, and distinct emission spectra for numerous real-world applications [12]. The emission through impurity ions, also called activators, is accompanied by electronic transitions. In some cases, the intensity of the light emitted by the doped materials is feeble. So, enhancement in the luminescent intensity is achieved by incorporating the second type of impurity called as sensitizers, which helps in the energy transfer to the activator ions, as shown in **Fig. 1.1**. The sensitizers absorb the energy and then transfer to the activators via different energy transfer channels/mechanisms [13–16]. The emission characteristics can be varied with the change in the dopants in the same host lattice. On the other hand, co-dopants such as alkali and alkaline-earth metals are also used to alter the luminescent features due to their role as charge compensators and the creators of oxygen vacancies [16,17]. Thus, luminescent characteristics mainly depend on the type of the host lattice and dopant ions.

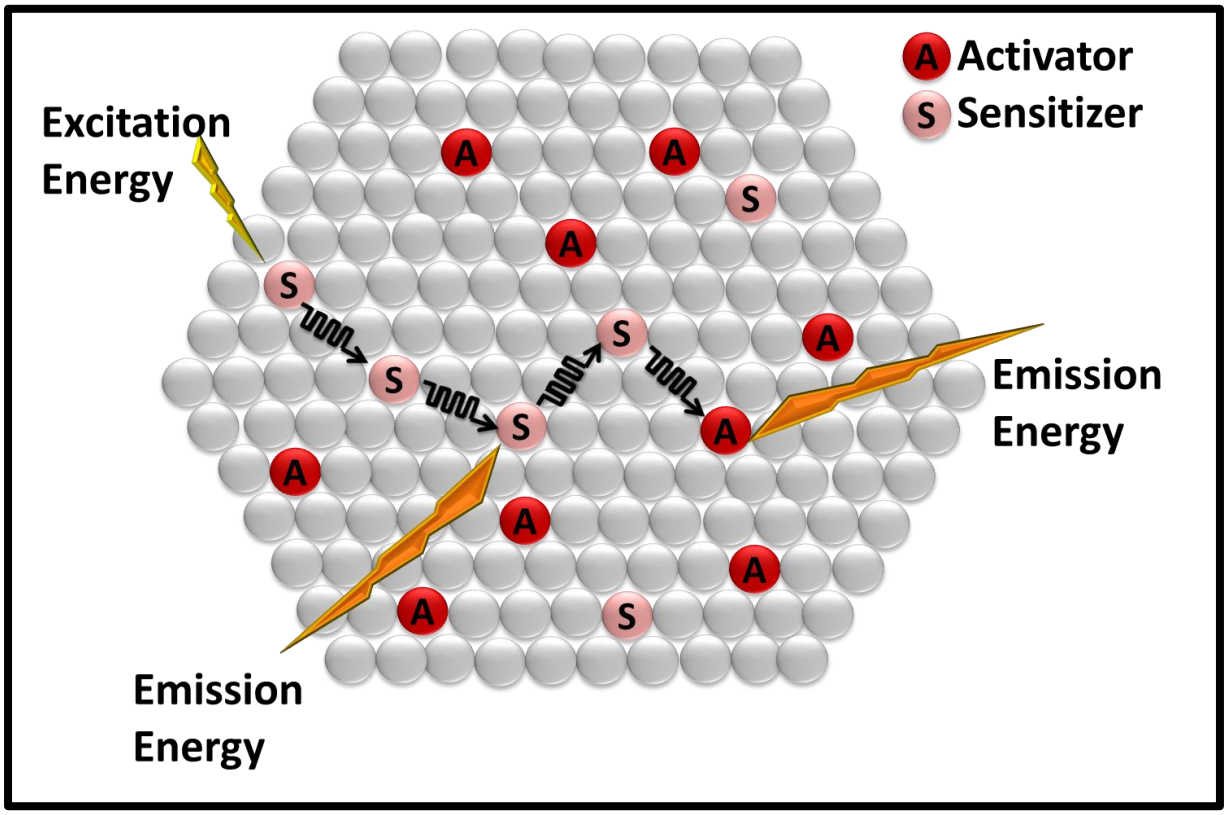

Figure 1.1: Schematic diagram of luminescent material containing activator (A) and sensitizer ions (S).

1.2 Fundamentals of Luminescence

1.2.1 Types of Luminescence

In luminescence phenomena, incident radiations are absorbed by the materials and re-emitted in the form of light. The emission of light is independent of the type of incident light. It depends on the type of host lattice and dopant ions. As already mentioned, if dopant ions are not used, then the emission of light takes place from the defects present in the material; for example, ZnO and $ZnAl_2O_4$ are good examples of materials in which luminescence takes place due to the presence of defects [18,19]. The luminescence phenomena can also be observed in nature such as, glow worms, fireflies, plants and deep-sea creatures. In general, two main processes take place in luminescence, (1) absorption of incident energy to get into the higher excited state and (2) de-excitation to the ground state with radiative emission. Luminescence is further divided into two types, i.e., phosphorescence (more than 10^{-8} sec) and fluorescence (less than 10^{-8} sec) depending on the decay time.

There are many types of luminescence; all are named after the use of different types of incident sources of energy. The different types of luminescence phenomena, their excitation source and applications in various fields are tabulated in **Table 1.1**.

Table 1.1: Types of different luminescence phenomena.

Type	Excitation Source	Applications
Photoluminescence	Electromagnetic radiations	LEDs, fluorescent lamps, display devices
Electroluminescence	Electric current/Electric field	LEDs, flat panel displays
Cathodoluminescence	Electron beam	Field emission displays, cathode-ray tubes
Chemioluminescence	Chemical reaction	Lighting sources in animals and plants, gas sensors, lasing
Thermoluminescence	Exposure to different ion beams and then heating	Dosimetric and biomedical applications
Triboluminescence	Mechanical	Remote sensing

1.2.2 Luminescence Mechanism

In the case of phosphors, host lattice consists of a luminescent center, for example, Gd_2O_3:Eu, Y_2O_3:Dy, and Al_2O_3:Tb [20–22]. In these cases, host lattice is Gd_2O_3, Y_2O_3, and Al_2O_3, while Eu, Dy, and Tb are the activators. In luminescence, the excitation energy is absorbed by the activator (A) and it gets into the excited state (A*). From excited state, the ion returns to the ground state via radiative (R) and non-radiative (NR) emission, as shown in **Fig. 1.2 (a)**. However, NR transitions do not take part in luminescence phenomena. The energy is absorbed by the host lattice itself and converted into the lattice vibrations in the form of heat energy. The loss of energy due to lattice vibrations leads to non-radiative emission. A good host lattice is the one in which there are less energy losses due to heat energy. Thus, to create efficient luminescent material, radiative transitions should be more than non-radiative transitions.

In case, activator ion is weak for energy absorption, sensitizer (S) ion is used. The sensitizer absorbs the energy and gets into the excited state (S*) and from there, energy is transferred to the activator ion via the cross-relaxation process (**Fig**. **1.2 (b)**). Then, activator ion (A) goes to the excited state (A_1^*), which is populated by energy transfer. From A_2^* state, it gets relaxed to the lower excited state (A_1^*) via non-radiative transitions, which prevents the back transfer. Subsequently, activator ion returns to the A state from A_2^* state via radiative emissions (photoluminescence). Thus, sensitizer ion helps in the effective radiative emission.

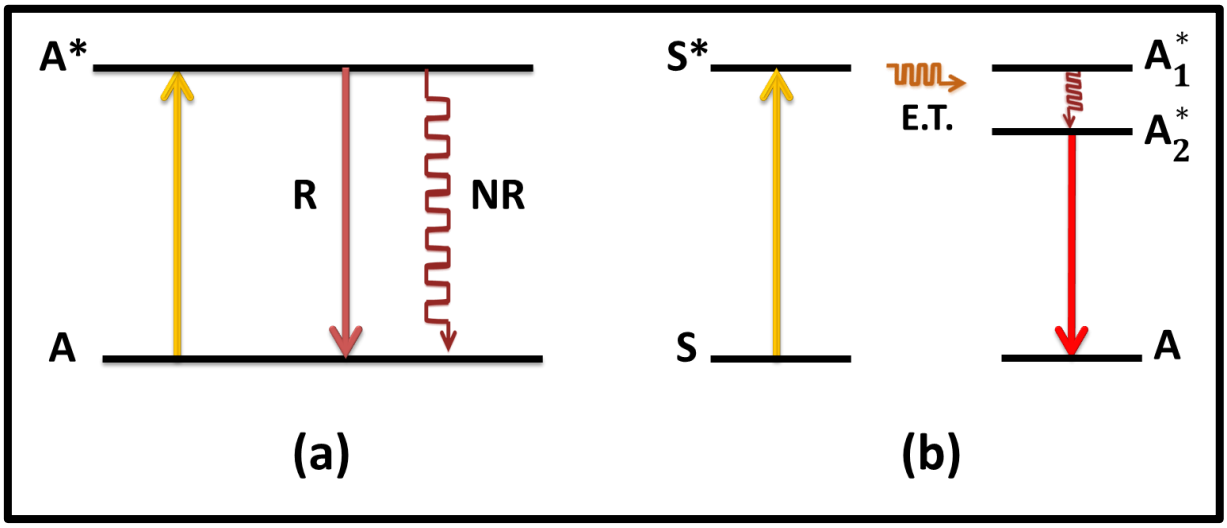

Figure 1.2: (a) Representation of energy level diagram of luminescence ion (A) and (b) energy transfer mechanism [21].

1.2.3 Jablonski Diagram

The different absorption and emission transitions in luminescence are represented by the Jablonski diagram, named after ***Professor Alexander Jablonski***. These are used to explain several excited state molecular processes. In this diagram, vertical lines represent different states and are grouped horizontally by spin multiplicity. Straight arrows are used to represent the radiative transitions and squiggly arrows for non-radiative transitions. The thick lines represent the electronic states and various vibrational states between the electronic states are represented by thicker lines. Once the molecule absorbs the energy, there are various ways in which it can come to the ground state. The various mechanisms involved in the absorption, emission and relaxation processes are represented in the Jablonski diagram as shown in **Fig. 1.3**.

The excited state molecule comes to lower excited state S_1 via non-radiative internal conversion (IC). The transitions which take place between the same spin states from S_1 to S_0, lead to fluorescence. The decay time of the fluorescence is very small in the range of nanoseconds and the transitions are spin allowed. Intersystem crossing (ISC) processes occur in triplet states. When the transition takes place from different spin states, i.e. from T_1 to S_0, the emission is called phosphorescence. The decay time in the case of phosphorescence is larger than the fluorescence i.e., in the range of micro to seconds. This process is spin forbidden. The phosphorescence leads to the persistence luminescence in the materials i.e. afterglow effects.

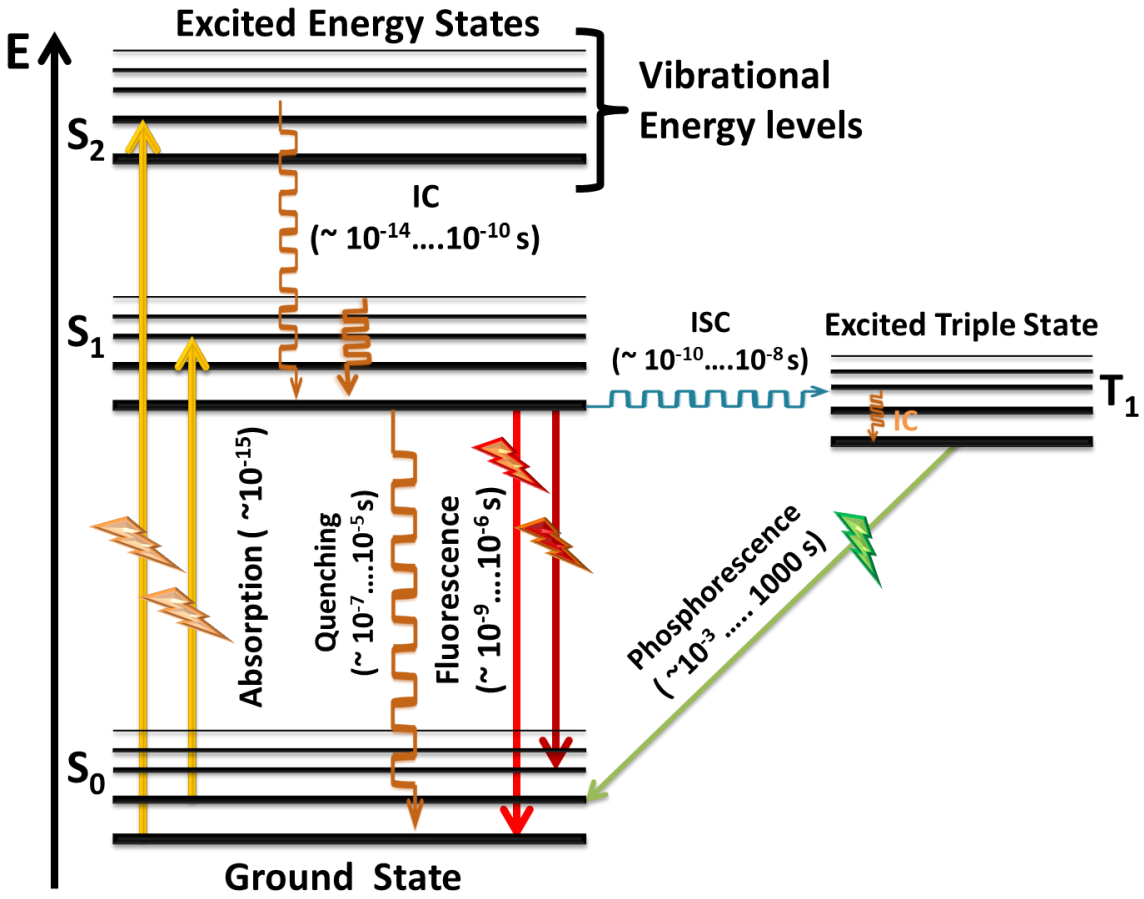

Figure 1.3: Jablonski diagram representing the absorption of light and emission via fluorescence and phosphorescence [23].

1.2.4 Configurational Coordinate (CC) Model

The main constituents of phosphors are host lattice and dopant ion. The excitation and emission spectra of phosphors also depend on the nature of the dopant ion. The shape (narrow or broad) of the optical absorption band can be determined from the CC diagram. In this, the central metal ion is supposed to be at rest, and surrounding ligands move away and come back in the same phase, as shown in **Fig. 1.4 (a).** Moreover, the excitation and ground states are represented by parabolic curves, considering the vibrational motion to be harmonic. **Fig. 1.4 (b)** represents the CC diagram, in which energy (E) versus metal-ligand distance (R) is plotted. This model allows the interaction between the electrons and vibrations of the central ion under consideration. The value $\Delta R = R_0 - R_0'$, is a qualitative parameter. The absorption band is a narrow line if $\Delta R=0$ and ground as well as excited state's parabola lie exactly above each other. The transition probability from the ground ($v=0$) to excited ($v=v'$) state is proportional to

$$\langle e|r|g\rangle \langle \chi_{v'}|\chi_v\rangle \qquad (1.1)$$

where, excited and ground state are represented by e and g symbols, respectively; r is electric-dipole operator and χ represents vibrational wave functions.

The first part of the equation (1.1) is the electronic matrix element and independent of the vibrations. The second part of the equation (1.1) gives vibrational overlap. The intensity of vibration and width/shape of the absorption band are decided by the former and latter part of the equation (1.1), respectively.

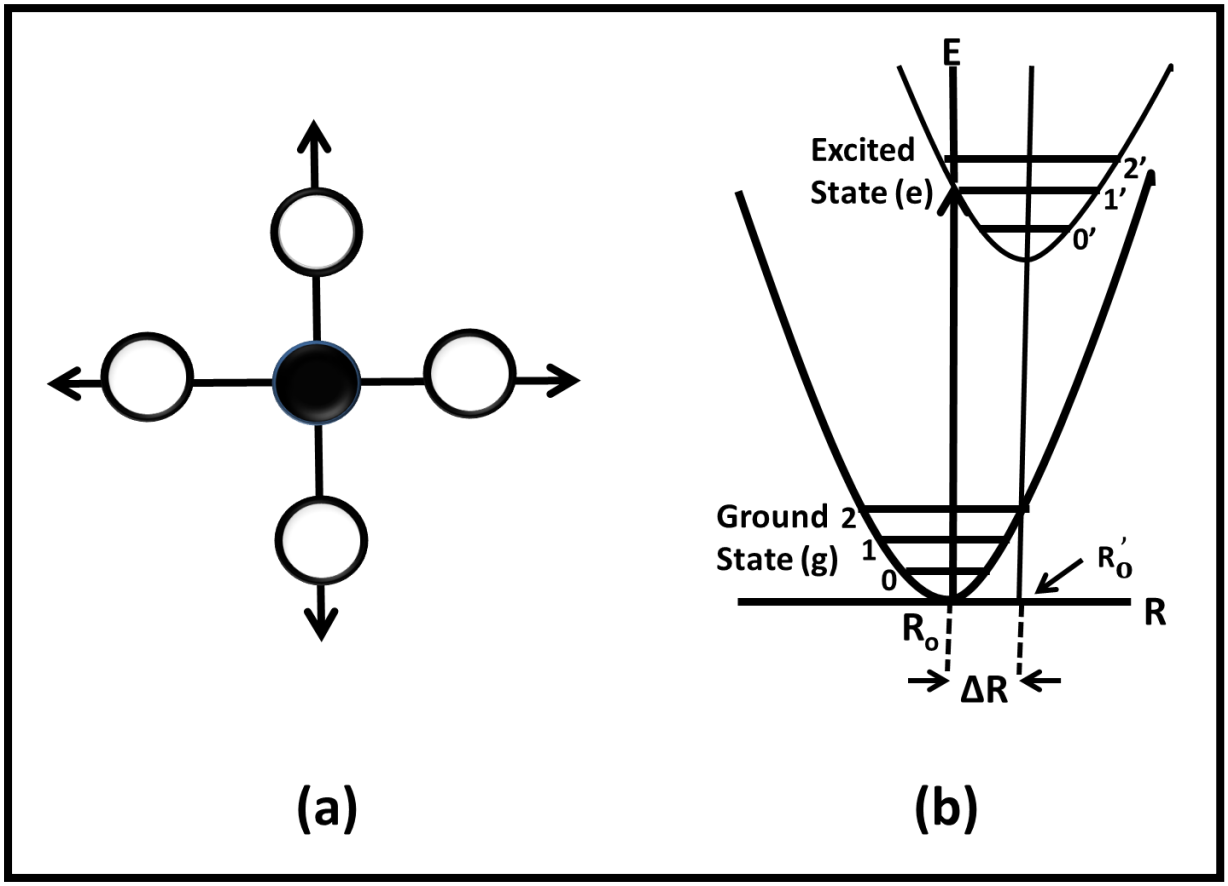

Figure 1.4: (a) Symmetric stretching vibrations of the square planar ligand with center metal cation (in black color) and ligands (in white color) moving to and fro w.r.t. the central cation and (b) Configurational coordinate diagram [24].

If ΔR=0, the vibrational overlap is maximum for ν=0 to ν'=0, and this results in the absorption band as one line. This vibration is also known as zero vibrational or no-phonon transition. If ΔR≠0, ν=0 level will have maximal overlap for different levels for which ν'>0. This results in a broad spectrum. The broader maxima indicate the larger value of ΔR. The intensity of the optical transition depends on two important selection rules, which are stated below:

- **Spin selection rule**: The electronic transitions between different levels for which change in spin i.e. ΔS≠0, are not allowed.

- **Parity selection rule:** The electronic transitions between different levels having same parity values are not allowed.

Inspite of allowed transitions, some forbidden transitions also take place due to relaxation in the selection rules. The relaxation in the selection rules is related to the electron-vibration coupling, spin-orbit coupling, and uneven crystal field terms. The intensity of these transitions is weaker than the allowed transitions, often more than 10^6 times.

1.3 Luminescence in Lanthanide Ions

The activators used in phosphors are mostly rare-earth (RE) or transition metal (TM) ions. The emission spectra are broad due to the transitions originating from the d orbitals in TM ions. The spectroscopic analysis of RE ions reveals that these can be used as efficient dopants for different host lattice. It is also reported that the crystal field splitting is less in case of RE ions as compared to TM ions [25]. Rare earth elements include 17 elements (Sc, Y, and Lanthanides La-Lu). The general properties of rare earth elements like atomic radii, ionic radii, valency, electronic configuration, etc. are given in **Table 1.2**. Among the trivalent rare-earth ions, Sc^{3+}, Y^{3+}, La^{3+} and Lu^{3+} ions have $^1S_0$ ground state, so they do not show transitions in 4f configuration. They are considered as spectroscopically inert ions and are used in the composition of host lattices. So, the lanthanide ions are frequently used as activators and sensitizers in different host lattices. The emission spectra exhibited by them are very sharp, narrow and intense. This is owing to the presence of the electrons in the f-orbitals. The f-orbitals lie inside the inner shells, which are shielded from the adjacent $5s^2$ and $5p^6$ orbitals. Thus the crystal field experienced by the 4f electrons is weak. The presence of f-f transitions in RE ions makes them suitable for various applications like magnetic materials, catalysts, luminescent devices, bio-sensors, display devices, optoelectronic devices, and biomedical applications. Lanthanide ions consist of elements from lanthanum to lutetium. They generally exist in +2 and +3 oxidation states. However, +3 oxidation state is stable among the other states. The outer electronic configuration for trivalent lanthanide ions, in general, can be written as $5s^2\ 5p^6\ 4f^n$, where n varies from 1 to 13. Lanthanide ions exhibit sharp, narrow, and intense spectra owing to 4f-4f orbit except for Ce^{3+}, which shows broadband luminescence spectra attributable to 4f-5d electronic transitions. The divalent ions such as Yb^{2+}, Sm^{2+} and Eu^{2+} show broadband emission and excitation spectra because of the parity allowed $4f^n \rightarrow 4f^{n-1}$ 5d electronic transition. Thus, the trivalent lanthanide activated materials exhibit sharp, narrow and intense emission spectra, long lifetimes and lesser chances of blinking and fading, etc., owing to the presence of unpaired electrons in the f orbitals.

Table 1.2: General properties of rare-earth elements.

Element	Atomic number	Atomic Weight	Electronic Configuration	Electronegativity	Atomic radii (Å)	Valency	Ionic radii (RE^{3+})*
Sc	21	44.956	$\{Ar\}3d^14s^2$	1.20	1.606	3	0.745
Y	39	88.906	$\{Ar\}4d^15s^2$	1.11	1.81	3	0.900
La	57	138.905	$\{Xe\}5d^16s^2$	1.08	1.877	3	1.045
Ce	58	140.115	$\{Xe\}4f^26s^2$	1.06	1.825	3,4	1.01
Pr	59	140.91	$\{Xe\}4f^36s^2$	1.07	1.828	3,4	0.997
Nd	60	144.24	$\{Xe\}4f^46s^2$	1.07	1.821	3	0.983
Pm	61	145	$\{Xe\}4f^56s^2$	1.07	1.81	3,2	0.97
Sm	62	150.36	$\{Xe\}4f^66s^2$	1.07	1.802	3,2	0.958
Eu	63	151.965	$\{Xe\}4f^76s^2$	1.01	2.042	3,2	0.947
Gd	64	187.25	$\{Xe\}4f^75d^16s^2$	1.11	1.802	3	0.938
Tb	65	158.925	$\{Xe\}4f^86s^2$	1.10	1.782	3	0.923
Dy	66	162.5	$\{Xe\}4f^{10}6s^2$	1.10	1.773	3	0.912
Ho	67	164.93	$\{Xe\}4f^{11}6s^2$	1.10	1.766	3	0.901
Er	68	167.26	$\{Xe\}4f^{12}6s^2$	1.11	1.757	3	0.890
Tm	69	168.934	$\{Xe\}4f^{12}6s^2$	1.11	1.746	3,2	0.880
Yb	70	173.04	$\{Xe\}4f^{13}6s^2$	1.06	1.94	3,2	0.868
Lu	71	174.98	$\{Xe\}4f^{14}5d^16s^2$	1.14	1.734	3	0.861

*****Ionic radii correspond to 6-fold coordination of ions in +3 oxidation state.

1.3.1 Rare-Earth Oxides

Till now, many luminescent materials have been investigated for various practical applications. The emission features depend a lot on the type of host lattice, such as silicates, aluminates, oxides, fluorides, chlorides, borates, etc.[26–29]. So far, many luminescent materials are studied by various researchers, out of which rare-earth oxides have drawn considerable attention because of large Stoke shifts, low phonon energy, long lifetimes, photostability, lack

of photoblinking, etc. [8,30–32]. Their excellent properties lie in the fact that they are stable in vacuum and do not produce hazardous gases when bombarded by electron beams. They find vast applications in electroluminescent devices, display devices, catalysts, magnetic resonance imaging (MRI), bio-imaging, etc. They possess low phonon energy that leads to the reduction in non-radiative transitions and thereby enhancing the luminescent efficiency. In addition to this, unlike semiconductor quantum dots, emission wavelengths of lanthanide oxides nanoparticles (NPs) are size-independent and the exciton Bohr radius is very small. However, doping of lanthanide ions in the nanosize host leads to variations in the luminescence and decay profiles.

1.4 Introduction to Gd_2O_3

Gd_2O_3, also known as gadolinia, is an excellent host matrix. Gd_2O_3 exists in three polymorphic forms i.e., hexagonal ($P\bar{3}m1$), monoclinic (C2/m) and cubic ($Ia\bar{3}$). The room temperature stable structure of Gd_2O_3 is cubic. It changes to its monoclinic phase when heated above 1250 ℃ and to the hexagonal phase beyond 2400 ℃ [33]. However, there are very controversial statements for its structural changes. The mostly reported stable structures at lower temperatures are cubic and monoclinic. Gd_2O_3 has high chemical and thermal stability, non-toxicity, non-hygroscopic nature, low phonon energy (~600 cm^{-1}), high dielectric constant, high bandgap (5.8-6.4 eV), and high refractive index. It is a potential material for many applications such as color television tubes, field emission displays (FDPs), biosensors, bio-labels, MRI contrast agents, etc.[34–36]. Gd_2O_3 also shows paramagnetic behavior due to seven unpaired electrons in f orbitals in Gd^{3+} state. Rare-earth doped Gd_2O_3 phosphors can be used for various biomedical applications. Gd_2O_3 is a UV light excited phosphor and emits several emission peaks. However, when it is doped with other elements, it gives sharp, intense and different emissions depending on the electronic transitions/defects involved. Among the various dopants, Gd_2O_3 is considered as a suitable matrix for the RE doping due to similarity in the ionic radii. Its band structure is very wide, so it is a favorable host lattice. Gd_2O_3 phosphors with high chemical stability and feasibility of their fabrication process make them a suitable choice for UC applications. Gd_2O_3 is a single-phase multimodal nanoprobe due to its paramagnetic and multicolor emission luminescent behavior, which is admired for UC applications.

1.4.1 Structure of Gd_2O_3

The two stable forms of Gd_2O_3 are cubic and monoclinic. Cubic-Gd_2O_3 has two non-equivalent crystallographic sites i.e., 8 b site with S_6 symmetry (centrosymmetric) and 24 d site with C_2 symmetry (non-centrosymmetric), both are in octahedral coordination. In C_2 site, the central cation is present along with two oxygen vacancies on the face diagonal of the cube; while in S_6 site, oxygen vacancies are present along the body diagonal [17,37]. These sites are present in the ratio 3:1, i.e. 75% of Gd^{3+} ions occupy C_2 and 25% ions occupy S_6 sites. C_2 site possesses no inversion symmetry and S_6 site has inversion symmetry. In cubic Gd_2O_3, emission originates from the C_2 site because dopant ions have more probability of occupying this site and this site has no center for inversion. When the dopants are placed at C_2 site, it leads to the hypersensitive transitions, while site occupation at S_6 site leads to the insensitive transitions (insensitive to the local symmetry). In monoclinic-Gd_2O_3, there are three non-equivalent sites, namely A, B, and C, with C_s symmetry. In these sites, Gd^{3+} ions have seven-fold coordination symmetry[38,39]. The coordination of two Gd^{3+} ions can be described by the six oxygen at the apexes of a trigonal prism and seventh oxygen along the normal to the face. The third Gd^{3+} ion is placed in the middle of distorted octahedron with seventh oxygen at a long distance. The pictorial representation of various sites in cubic and monoclinic Gd_2O_3 is shown in **Fig. 1.5 (a-b)**.

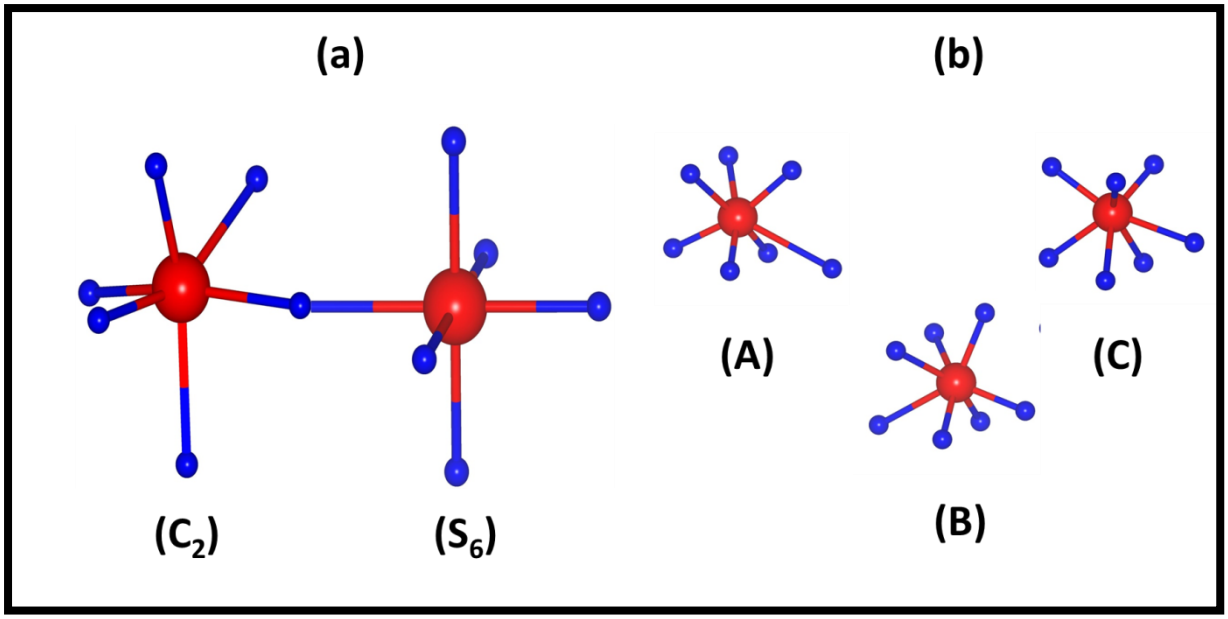

Figure 1.5: (a) Sites in cubic-Gd_2O_3 and (b) sites in monoclinic-Gd_2O_3 (Images are produced using VESTA software).

1.4.2 Gd_2O_3 Phosphors and Applications

Gd_2O_3 sesquioxide is an efficient host matrix due to its thermal stability, chemical durability, high refractive index, wide bandgap, and low phonon energy. Hence, Gd_2O_3 is a promising host lattice for various dopants to exhibit different luminescence phenomena viz. down-conversion, downshifting and upconversion due to the efficient energy transfer. Gd_2O_3 is a suitable matrix for RE doping due to similarity in the ionic radii, charge, thermal and chemical stability. The intensity of the emission spectra also depends on many factors such as phase (cubic or monoclinic), synthesis route, morphology, dopant concentration, etc. Gd_2O_3 itself exhibits intrinsic luminescence phenomena when it is irradiated under UV light. The emission peaks in undoped Gd_2O_3 are observed in the UV and visible regions. However, doping with the RE ions leads to the intense, distinct and sharp emission peaks in the visible and NIR regions[40–43]. Gd_2O_3 phosphors exhibit efficient color emissions with high intensity. These are extensively studied for optoelectronic devices for field emission displays, light-emitting diodes, fluorescent lamps, X-ray scintillators, and cathode-ray tubes. The various other applications of Gd_2O_3 phosphors are shown in **Fig. 1.6.**

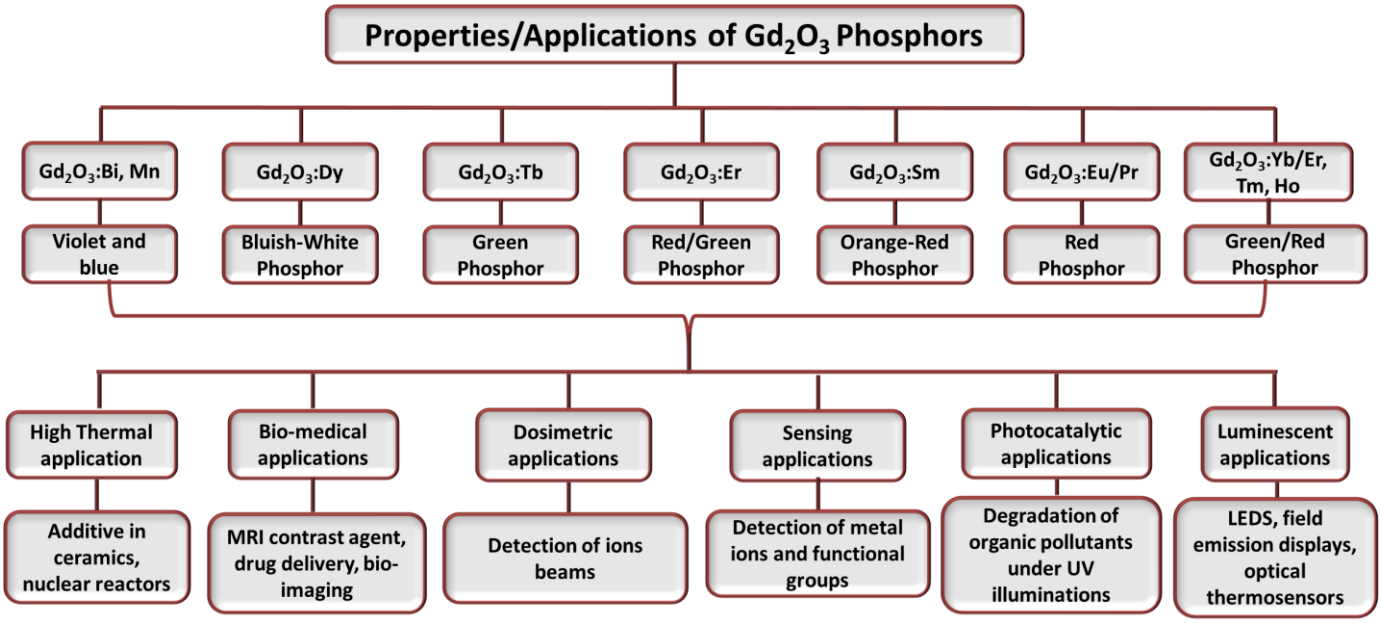

Figure 1.6: Various applications of Gd_2O_3 phosphors.

1.4.3 Gd_2O_3:Eu as Promising Red Light-Emitting Phosphor

Gd_2O_3 is iso-structural to Y_2O_3 sesquioxide and belongs to the family of Ln_2O_3 (Space group $Ia\bar{3}$ (206), Ln=La-Lu, Y). Gd_2O_3:Eu is a red light-emitting phosphor and has been widely studied for fluorescent lamps, cathode-ray tubes, contrast agents in MRI, bio-medicines, etc.

Gd_2O_3 is an ideal host matrix in the case of Eu^{3+} dopant. This is because the ionic radius of Eu^{3+} ions (0.947 Å) is close to the Gd^{3+} ions (0.938 Å) and can be easily incorporated into the Gd_2O_3 matrix. As compared to Y_2O_3:Eu, Gd_2O_3:Eu has a higher strong charge transfer band and luminescent intensity[22,44]. This is ascribed to the fact that the electronegativity of the Gd^{3+} ions (1.20) is smaller than the Y^{3+} ions (1.22), which allows easier charge transfer from the filled 2p orbitals of oxygen to the filled f orbitals of the europium ions. Moreover, transitions of Gd^{3+} around 250 and 270 nm corresponding to $^8S_{7/2}$ to ^6D_J and ^6I_J overlap, which leads to the photoluminescent enhancement at 612 nm via energy transfer from Gd^{3+} to Eu^{3+} ions. In the present study, Eu^{3+} is used as a probe to investigate the structural, morphological, and optical changes in the cubic-Gd_2O_3 host lattice. The recent progress in the synthesis of Gd_2O_3:Eu phosphors is discussed in the next chapter.

References

1 N. Hirosaki, R. Xie, K. Inoue, T. Sekiguchi, B. Dierre, N. Hirosaki, R. Xie and K. Inoue, *Appl. Phys. Lett.*, 2007, 061101, 2–5.

2 A. A. Talin, K. A. Dean and J. E. Jaskie, *Solid- State Electron.*, 2001, 45, 963–976.

3 G. Li, X. Xu, C. Peng, M. Shang, D. Geng, J. Chen and J. Lin, *Fluoresc. Lumin. Mater.*, 2011, 19, 3020–3028.

4 C. S. Kamal, T. K. V. Rao, T. Samuel, P. V. S. S. S. N. Reddy, J. B. Jasinski, Y. Ramakrishna, M. C. Rao and K. R. Rao, *RSC Adv.*, 2017, 7, 44915–44922.

5 I. V. B. Maggay and W.-R. Liu, *J. Nanosci. Nanotechnol.*, 2018, 18, 3–10.

6 G. Seeta Rama Raju, E. Pavitra, G. Nagaraju and J. S. Yu, *Dalt. Trans.*, 2015, 44, 1790–1799.

7 Y. Yang, F. Wu, H. Yu, Y. Hu, C. Qiu, J. Li, H. Zhang, X. Wang, L. Wei and B. Liu, *Optik (Stuttg).*, 2020, 200, 163455.

8 S. K. Hussain, G. S. R. Raju and J. Su Yu, *Ceram. Int.*, 2015, 41, 13264–13270.

9 G. S. Wu, Y. Lin, X. Y. Yuan, T. Xie, B. C. Cheng and L. D. Zhang, *Nanotechnology*, 2004, 15, 568.

10 J.-G. Li, X. Li, X. Sun, T. Ikegami and T. Ishigaki, *Chem. Mater.*, 2008, 20, 2274–2281.

11 S. K. Singh, K. Kumar and S. B. Rai, *Sensors Actuators A Phys.*, 2009, 149, 16–20.

12 R. Krishnan and J. Thirumalai, *New J. Chem.*, 2014, 38, 3480–3491.

13 Z. Liu, H. Deng and D. Chen, *Ceram. Int.*, 2019, 45, 13235–13241.

14 X. Zhou and X. Wang, *Opt. - Int. J. Light Electron Opt.*, 2013, 124, 1038–1040.

15 D. Li, W. Qin, P. Zhang, L. Wang, M. Lan and P. Shi, *Opt. Mater. Express*, 2017, 7, 329.

16 Ž. Antic, V. Lojpur, M. G. Nikolic, Đ. Vesna, P. S. Ahrenkiel and M. D. Dramićanin, *J. Lumin.*, 2014, 145, 466–472.

17 R. Priya and O. P. Pandey, *J. Lumin.*, 2019, 212, 342–353.

18 M. Jain, A. Gundimeda, S. Kumar, G. Gupta and S. Ok, *Appl. Surf. Sci.*, 2019, 480, 945–950.

19 R. Raji and K. G. Gopchandran, *J. Sci. Adv. Mater. Devices*, 2017, 2, 51–58.

20 E. H. Penilla, Y. Kodera and J. E. Garay, *Adv. Funct. Mater.*, 2013, 23, 6036–6043.

21 T. S. Atabaev, H. Ha, T. Vu, H. Kim and Y. Hwang, *J. Korean Phys. Soc.*, 2012, 60, 244–248.

22 R. Priya and O. P. Pandey, *Vacuum*, 2018, 156, 283–290.

23 J. R. Lakowicz, *Principles of Fluorescence Spectroscopy*, Springer, Boston, MA, 2006.

24 G. Blasse and B. C. Grabmaier, *Luminescent Materials*, Springer, Berlin, Heidelberg, 1994.

25 G. B. Nair, H. C. Swart and S. J. Dhoble, *Prog. Mater. Sci.*, 2020, 109, 100622.

26 R. Priya, I. Khurana and O. P. Pandey, *J. Mater. Sci. Mater. Electron.*, 2020, 31, 1912–1928.

27 R. Priya, A. Negi, S. Singla and O. P. Pandey, *Optik (Stuttg).*, 2020, 204, 164173.

28 D. Kumar, M. Sharma and O. P. Pandey, *Opt. Mater. (Amst).*, 2014, 36, 1131–1138.

29 M. Liu, P. Dang, Y. Wei, S. Liang, G. Liu, A. Geng, H. Lian and J. Lin, *J. Am. Ceram. Soc.*, 2019, 1–12.

30 R. Bazzi, M. A. Flores, C. Louis, K. Lebbou, W. Zhang, C. Dujardin, S. Roux, B. Mercier, G. Ledoux, E. Bernstein, P. Perriat and O. Tillement, *J. Colloid Interface Sci.*, 2004, 273, 191–197.
31 M. G. Nikolić, A. Z. Al-Juboori, V. Dordević and M. D. Dramićanin, *Phys. Scr.*, 2013, T157, 014056 (5pp).
32 Z. Liu, Q. Wang, Y. Yang, C. Tao and H. Yang, *J. Nanopart Res*, 2010, 12, 2233–2240.
33 M. Zinkevich, *Prog. Mater. Sci.*, 2007, 52, 597–647.
34 Z. Lv, T. Li, H. Yu, Y. Yang, X. Dong and L. Xia, *Microporous Mesoporous Mater.*, 2020, 305, 110354.
35 C. Zhou, H. Wu, C. Huang, M. Wang and N. Jia, *Part. Part. Syst. Charact.*, 2014, 31, 675–684.
36 M. Ahrén, L. Selegård, A. Klasson, F. Söderlind, N. Abrikossova, C. Skoglund, T. Bengtsson, M. Engström, P. O. Käll and K. Uvdal, *Langmuir*, 2010, 26, 5753–5762.
37 R. Priya and O. P. Pandey, *Spectrochim. Acta Part A Mol. Biomol. Spectrosc.*, 2020, 231, 118078.
38 R. K. Tamrakar, D. P. Bisen, K. Upadhyay and I. P. Sahu, *J. Alloys Compd.*, 2016, 655, 423–432.
39 Y. Zou, L. Tang, J. Cai, L. Lin, L. Cao and J. Meng, *J. Lumin.*, 2014, 153, 210–214.
40 M. L. Pang, J. Lin, J. Fu, R. B. Xing, C. X. Luo and Y. C. Han, *Opt. Mater. (Amst).*, 2003, 23, 547–558.
41 S. Gai, P. Yang, D. Wang, C. Li, N. Niu, F. He and X. Li, *CrystEngComm*, 2011, 13, 5480–5487.
42 X. Zhao, H. Suo, Z. Zhang and C. Guo, *Ceram. Int.*, 2017, 44, 2911–2918.
43 A. Kumar, C. G. E. da Silva, K. Kumar, H. C. Swart, S. K. Maurya, Pr. Kumar and S. P. Tiwari, *Mater. Res. Bull.*, 2018, 112, 28–37.
44 D. Kumar, M. Sharma and O. P. Pandey, *J. Lumin.*, 2015, 158, 268–274.

CHAPTER 2

LITERATURE REVIEW

Overview

Inorganic lanthanide oxides are promising host lattices owing to their chemical and physical stability, large Stoke shifts, absence of photobleaching, and low phonon energy. Among the various lanthanide oxides, Gd_2O_3 is an excellent host matrix for the doping of many rare-earth and transition metal ions due to low phonon energy, high thermal stability, and chemical durability. In the present study, europium ions are chosen as a probe to investigate the structural and optical changes in the Gd_2O_3 host lattice by varying different parameters. The selection of Eu^{3+} ions was done due to narrow, intense and intense emission spectra originating from the $^5D_0 \rightarrow {}^7F_{1,2,3,4}$ transitions. Gd_2O_3:Eu is a proficient UV light excited red light-emitting phosphor and finds prospective applications. The present chapter discusses the state-of-art synthesis of Gd_2O_3:Eu phosphors and various factors affecting its luminescent characteristics. The synthesis of Gd_2O_3:Eu phosphors via different synthesis routes and their consequences on the size, morphology, and phases have been discussed. The various parameters such as doping, co-doping, morphology, and phases affecting the luminescence features of the Gd_2O_3 phosphors, are discussed in detail. After peer-review of the existing literature on Gd_2O_3:Eu phosphors, the objectives of the thesis work are proposed.

2.1 Introduction

Gd_2O_3 has high chemical and thermal stability, non-toxicity, non-hygroscopic nature, low phonon energy (~600 cm^{-1}), high dielectric constant, high bandgap (5.8-6.4 eV), and high refractive index [1–8]. Gd_2O_3 is a UV light excited phosphor, and it emits several emission peaks. However, when doped with other elements, it gives sharp, intense, and different emissions depending on the electronic transitions/defects involved. Among the various rare-earth dopants, Gd_2O_3 is an ideal host matrix for the Eu^{3+} ions due to similarity in the ionic radii of Eu^{3+} (0.947 Å) and Gd^{3+} ions (0.938 Å). Gd_2O_3:Eu is a UV active phosphor and exhibits sharp, intense, and narrow emission spectra. The incorporation of europium ions in Gd_2O_3 host lattice leads to prominent emission peaks around 580, 590-595, 610-625, 650, and 700 nm, corresponding to the $^5D_0 \rightarrow {}^7F_{0,1,2,3,4}$ transitions, respectively [9–11]. Among these peaks, the peak corresponding to the $^5D_0 \rightarrow {}^7F_2$ transition is hypersensitive and highly dependent on the local environment of the Eu^{3+} ions in the Gd_2O_3 host lattice [12–15]. The excitation spectra of Gd_2O_3:Eu consist of host absorption band (HAB), charge transfer (CT) band, and excitation peaks corresponding to the Eu^{3+} and Gd^{3+} ions. The position of HAB and CT bands depends on the phase, emission wavelength, and synthesis parameters of Gd_2O_3:Eu. As already discussed in **Chapter 1**, Gd_2O_3 exists in three phases, i.e., hexagonal, monoclinic, and cubic. Out of these phases, only two phases are stable at lower temperatures (cubic and monoclinic). When Eu^{3+} ions are incorporated in the Gd_2O_3 lattice, they occupy different sites in these structures. There are two crystallographic sites (C_2 and S_6) in cubic and three sites (A, B, and C) in monoclinic Gd_2O_3. It is also observed that the cubic Gd_2O_3:Eu emits intense emission spectra as compared to monoclinic Gd_2O_3:Eu [16–19]. In the following sections, the literature on the different synthesis methods and factors affecting the luminescent properties of Gd_2O_3:Eu has been reviewed and discussed in detail.

2.2 Synthesis of Gd_2O_3:Eu Phosphors

2.2.1 Solid-State Method

It is a high-temperature route for the production of materials at a larger scale. The synthesized materials are generally microcrystalline with pure phase. However, sometimes secondary phases may also appear due to the agglomeration of particles. This synthesis method is not morphology controlled. Tamrakar *et al.* [20] synthesized Gd_2O_3:Eu phosphors via solid-state method and investigated its luminescent characteristics. The initial precursors opted were the oxides of the corresponding host and dopant elements, which were weighed in stoichiometric ratio and pre-heated at 1100 °C for 1 h. After grinding, the samples were again

subjected to calcination at 1400 ℃ for 4 h. The obtained Gd_2O_3 phosphors were found to have cubic phase and average crystallite size in the range 66-75 nm.

2.2.2 Combustion Method

The combustion synthesis process is one of the established low-temperature synthesis routes. The end products obtained are highly crystalline, pure, and uniform. This method requires different reducing (urea, glycine, and citric acid) and oxidizing agents (metal nitrates). The amount of fuel required is dependent on the propellant chemistry, which is calculated using molar ratio of the oxidizing to the reducing agents. The reaction is considered stoichiometrically balanced when the valency of the reducing agent balances the valency of the oxidizing agent, and this ratio is 1. **Table 2.1** represents the synthesis conditions of Gd_2O_3:Eu phosphors synthesized via the combustion route.

Table 2.1: Summary of synthesis conditions and outcomes of Gd_2O_3 phosphors synthesized via combustion route.

Compound Name	**Fuel**	**Combustion temperature (Phase)**	**Annealing Temperature (phase)**	**Ref.**
Gd_2O_3:5%Eu^{3+}	Urea (A.R.) and Glycol	-	600, 700 and 800 ℃ for 2h, (cubic)	[17]
Gd_2O_3:Eu (1 to 5%)	Urea	-	500 ℃ for 2h (monoclinic)	[21]
$Gd_{1.92-x-y}Zn_xLi_yEu_{0.08}O_{3-\delta}$ ($0\leq x\leq 1.1$, $0\leq y\leq 0.1$)	Glycine	-	500 ℃ for 1h (cubic)	[22]
Gd_2O_3:3%Eu^{3+}	Glycine	620 ℃	500 ℃ for 4h (amorphous cubic) 1000 ℃ for 3h (cubic)	[23]
$Gd_{1.95}Eu_{0.04}M_{0.01}O_3$ (M= Li, Na and K)	ODH	400 ℃ (monoclinic + cubic)	600-900 ℃ for 3h (major monoclinic+ minor cubic)	[24, 25]
Gd_2O_3:Eu	Urea	550 ℃	1000 ℃ for 3h (cubic)	[26]
	Carbonhydrazide	500 ℃	1000 ℃ for 3h (cubic)	
	Sucrose	380 ℃	1000 ℃ for 3h (cubic)	
	Glycine	300 ℃	1000 ℃ for 3h (cubic)	

It can be observed from **Table 2.1** that in combustion synthesis route, both the monoclinic and cubic phases of Gd_2O_3:Eu can be obtained. The formation of the phase(s) whether cubic or monoclinic, depends on the type of fuel used, fuel amount, and the calcination temperature.

2.2.3 Sol-Gel Method

This synthesis route is known to yield nano-size particles with uniform size distribution, high purity, and crystallinity. In this process, a chelating agent is used to form a gel via hydroxyl and carboxyl groups. Generally, citric acid is used as a chelating agent, so this method is also known as the citrate-gel method. To increase the polymerization, ethylene glycol is also used as a medium. All the precursors are mixed along with citric acid (in particular ratio; metal ions to citric acid) in an aqueous solution and then heated around 80-100 ℃ (depending on vaporization), at which gel is formed. The gel is dried to form the xerogel/aerogel/cryogel depending upon the type of drying process. Some of the resulting outcomes of Gd_2O_3 phosphors synthesized via sol-gel method are summarized in **Table 2.2**.

Table 2.2: Reaction conditions and results of Gd_2O_3 phosphors synthesized via sol-gel method.

Compound Name	Chelating /Gelating agent/ Complexant	Medium	Stirring/Drying Temperature	Prefiring/ Calcination Temperature	Morphology	Ref.
SiO_2@Gd_2O_3:Eu	Citric acid/PEG	Water ethanol (v/v= 1:7)	RT-3h/ 100 ℃-1h	-/ 300 to 800 ℃-2h	Spheres ~500 nm	[27]
Gd_2O_3:Eu	Citric acid/DEG	Water	100 ℃-5h/ 180 ℃-1h	400 ℃-2h/ 800-4h	Monodisperse spheres ~25 nm	[28]
Gd_2O_3:Eu	Citric acid/NH_4OH (pH~2)	Water	70 ℃ till gel formation	250 ℃-2h/ 600, 700, 800 ℃-2h	Particles size 32-52 nm	[29]
Gd_2O_3:Eu	NH_4OH	Water and ethanol	RT-4h/ 120 ℃-Overnight	-/ 800, 900, 1000, 1100 ℃-2h	Particles size 90 - 200 nm	[30]
Gd_2O_3:Eu^{3+}, Gd_2O_3:Eu^{3+}/Silica	EDTA-Na_2	Water	70 ℃ / 105 ℃-1h	-/350 ℃	Agglomerated particles with 20-25 nm size	[31]
Gd_2O_3:Eu^{3+}	Pluronic F-127	Ethanol	350 ºC for 30 min/ 100 ºC-24 h	-/300 to 800 ºC-1h	Homogeneous spherical particles with size 1 to 4 µm	[32]

RT= Room temperature; PEG= Polyethylene glycol; DEG= Di-ethylene glycol; EDTA= Ethylenediaminetetraacetic acid.

2.2.4 Hydrothermal/Solvothermal Method

One dimensional elongated structures such as nanowires, nanorods, nanotubes, nanoprisms, and nanodisks are preferred over other nanostructures for device applications due to their exceptional optical properties. For this, hydrothermal a low-temperature synthesis route is preferred. It is used to engineer different nanostructures with the variation in pH, temperature, and additives. In this method, a stainless steel autoclave is used in which

hydrolysis and condensation of reactants with water as an aqueous solution takes place. The autoclave is either placed in a conventional oven or furnace at optimized temperatures ranging from 120 to 250 ℃ for different holding durations. The end product taken out of the autoclave is generally $Gd(OH)_3$ (in case of Gd_2O_3), which is further subjected to the heat treatment at different temperatures to get GdOOH and Gd_2O_3 phase. It is found that oxides obtained after calcination of hydroxides retain their morphology. However, small shrinkage is also observed in the dimensions due to the loss of water molecules from the hydroxides. The solvothermal method is also the same as that of the hydrothermal method irrespective of the fact that this method involves the usage of different solvent mediums except for water, surfactants, and templates to alter the morphologies during synthesis [33–35]. Chang *et al*.; Priya and Pandey; and Selvalakshmi and Bose; synthesized rod-shaped Gd_2O_3:Eu phosphors via hydrothermal method using NaOH (pH= 13) as a precipitating agent [36–38]. Recently, Kaur *et al.* reported the thermal degradation of $Gd(OH)_3$ to form Gd_2O_3 [39]. In their study, phase evolution of the Gd_2O_3 was studied via thermal kinetics. To analyze the influence of pH and temperatures, Le *et al*. used KOH to vary pH values ranging from 8 to 14 with different autoclave temperatures in the range from 120 to 180 ℃ for 12h [40]. It was found that at pH= 8-10, nanorods were formed with low aspect ratio; at pH= 10-12, high aspect ratio nanorods with variable dimensions were formed, at pH>13, nanosheets, nanotubes, nanorods were formed. Further, it was concluded from their study that nanorods and nanowires were formed at low temperatures. However, formation of nanorods and nanowires of high aspect ratio with uniform morphologies were observed at high temperatures. Dhananjay *et al.* [1,41] used CTAB and HMT during hydrothermal synthesis of Gd_2O_3:Eu phosphors at temperatures varying in the range 120-240 ℃ for 24 h. It was observed that the surfactants did not have much influence on the morphology except the fact that samples were less agglomerated. The uniform rod-like morphology with sharp ends was obtained. The optimum temperature for the synthesis was found to be 180 ℃. Below and above this temperature, non-uniform and agglomerated rods were observed. Xing *et al.* [42] synthesized nanohexagrams via glucose assisted hydrothermal synthesis.

The various morphologies, reaction conditions, and concluding remarks of the hydrothermal synthesis of Gd_2O_3 phosphors are summarized in **Table 2.3**. It can be illustrated from **Table 2.3** that different morphologies are obtained with the variation in pH, reaction times, and use of different additives. Also, the end products i.e. Gd_2O_3:Eu via this method after calcination at specific temperatures have cubic phase. Although hydrothermal is a promising route to engineer the morphological features, but the yield is low due to the size limitation of the vessel used for the synthesis.

Table 2.3: List of hydro(solvo)thermal synthesis conditions and end products of Gd_2O_3 phosphors.

Compound Name	Synthesis Method	Precipitating Agents/ Surfactant/ Solvent	Autoclave Temperature/ Time duration	Morphology	Ref.
Gd_2O_3:Eu	HT	KOH/ 1 mol% HDA/DI	180 ℃/24h	Regular uniform nanorods	[1]
Gd_2O_3:Eu	HT	NaOH /DI	180 ℃/24h	Nanorods	[36–39]
Gd_2O_3:Eu	HT	KOH/DI	120- 180 ℃/12h	pH = 8-10: nanorods with low aspect ratio pH= 10-12: nanorods with high aspect ratio pH>13: nanosheets, nanotubes, nanorods nanotubes at low temperature nanorods and nanowires at high temperature	[40]
Gd_2O_3:Eu	HT	KOH (pH=12)/ CTAB/DI	120, 180, 240 ℃/12h	Below 180 ℃: irregular nanorods 180 ℃: regular and smooth nanorods 210 ℃: irregular nanorods CTAB reduced agglomeration	[41]
Gd_2O_3:Eu	HT	NaOH (pH=11)/Glucose/ DI	180 ℃/12h	Nanorods for glucose free samples and hexagrams for the different ratio of glucose to metal ions	[42]
Gd_2O_3:Eu	HT	NH_4OH/DI	200 ℃/24h	At pH= 7; microrods At pH= 9; nanorods	[43]
Gd_2O_3:Eu/Dy	HT	Urea	180 ℃/24h	Smooth microspheres	[44]
Gd_2O_3:Eu	ST	CTAB/ PVP, DMF solution	180 ℃/24h	Nanospheres 80 to 100 nm	[45]
Gd_2O_3:Eu	ST	NH_4OH/DI and Toluene	180 ℃/12h	Variation in nanorods' dimensions with the variation of toluene content	[46]
$(Gd_{1-x}Eu_x)_2O_3$	HT	NH_4OH/DI	120-180 ℃/24, 48, 96h	Nanorods at pH 9-10 Nanotubes at pH<8.5	[47]
Gd_2O_3:Eu	ST	Thiourea/PVP/ Ethylene glycol	200 ℃/24h	Regular columnar	[48]
Gd_2O_3:Eu	ST	Urea/ PVP/ethanol	180 ℃/12h	Core-shell microspheres	[49]

HT= hydrothermal, ST= solvothermal; DI= distilled water; HDA= hexadecyl amine; HMT= hexamethylenetetramine; PVP= polyvinylpyrrolidone; CTAB= cetyltrimethylammonium bromide.

2.2.5 Co-precipitation Method

It is a convenient chemical route due to ease of synthesis on a large scale production level, environment-friendly approach, and low cost. When compared to other methods, viz. solid-state method (which requires high temperatures), hydrothermal route (where the use of sophisticated instruments and synthesis conditions are required), combustion method (generates residues due to use of organic fuels), the co-precipitation is a facile and economical route to yield well-shaped, mono-disperse and pure phase crystalline nanomaterials. In general, this method involves the mixing of the initial metal precursors such as their chlorides, nitrates, and acetates in stoichiometric ratios in an aqueous solution. To this mother solution, precipitating agents are added under mild or room temperature conditions. The commonly used precipitating agents are NaOH, KOH, LiOH, NH_4OH, urea, sodium carbonate, sodium bicarbonate, etc. The addition of a precipitating agent leads to formation of hydroxides, hydroxyl oxalates, or some intermediate compound out of the mother solution. The further procedure involves washings with ethanol or distilled water and then drying. The as-synthesized precipitates may have a crystalline phase or some intermediate phase depending upon the initial conditions. However, to induce the oxide crystallization phase, calcination at higher temperatures is required. This temperature can be determined from the TGA curves of the precipitates.

Table 2.4: Summary of reaction conditions and outcomes of Gd_2O_3 phosphors synthesized via co-precipitation method.

Compound Name	Precipitating agent (Reaction temperature –Time duration)	Sintering Temperature-Holding hours	Phase	Morphology	Ref.
Gd_2O_3:Eu	NH_4OH	800 °C-4h	Cubic	Nanorods	[50]
Gd_2O_3:Eu	NH_4OH (70 °C-16h)	700 °C-3h	Cubic	Nanorods (dia. 10- 20 nm; length <180 nm	[51]
Gd_2O_3:Eu	NH_4OH (75 °C-18h)	600 °C-2h	Cubic	Nanotubes	[52]
Gd_2O_3:Eu	NH_4OH (70 °C-10h)	700 °C-3h	Cubic	Nanorods (length 150 nm; width 14 nm)	[53]
Gd_2O_3:Eu	NH_4OH (RT)	800 °C-4h	Cubic	Nanorods (length 200- 500 nm, dia. 70- 120 nm)	[50]
Gd_2O_3:Eu	NH_4OH {pH= 9 (P1), 11 (P2)}+ Urea {pH= 9 (P3), 11 (P4)}	800 °C-2h	Cubic	P1-Hexagonal submicroprisms P2-Hexagonal microprisms P3-Hexagonal nanoprisms P4-Hexagonal nanoprisms	[54]
Gd_2O_3:Ln (Ln =Eu^{3+}, Dy^{3+}, Tb^{3+}, Sm^{3+}, Yb^{3+}/Tm^{3+}, Yb^{3+}/Er^{3+}, Yb^{3+}/Ho^{3+})	Urea (75 °C-4h)	800 °C-3h	Cubic	Spheres	[55]
Gd_2O_3:Ln^{3+} (Ln = Eu, Yb/Er) and Zn^{2+} and Li^+ as co-dopants	Urea (85 °C-4h)	1100 °C-4h	Cubic	Spheres	[56]

*RT= Room Temperature, dia. =diameter.

To control size and shape, either surfactants/templates or pH values are varied. In case of urea-based precipitation method, morphology of the synthesized particles is generally spherical. The intermediate product is $Gd(OH)CO_3$, which upon calcination at higher temperatures transforms to Gd_2O_3. **Table 2.4** summarizes the reaction conditions and outcomes of the co-precipitation route adopted by different research groups to synthesize Gd_2O_3 phosphors. It can be observed from **Table 2.4** that the synthesized end products, i.e., Gd_2O_3 phosphors via co-precipitation route have cubic structure having different morphologies. It is a well-known fact that the luminescence is enhanced in cubic Gd_2O_3 compared to a monoclinic counterpart. So, to get a pure crystalline cubic phase with different morphologies and high yield, the co-precipitation route is an efficient approach.

2.3 Factors Affecting Luminescent Properties of Gd_2O_3:Eu

2.3.1 Effect of Crystal Structure: Li *et al*. [16] investigated the luminescent characteristics of cubic Gd_2O_3:Eu synthesized via combustion route and used glycol as a dispersing agent. The excitation spectra on monitoring at 610 nm consisted of broadband with maxima peak at 255 nm due to Eu-O charge transfer (CT) band. The peak at 235 nm with a shoulder was attributed to the host lattice absorbance band (HAB). The peaks around 279 and 311 nm appeared because of $^8S_{7/2}$–^6I_J,^6P_J transitions of Gd^{3+} ions, respectively and peaks in the range from 300 to 500 nm were due to f-f transitions of Eu^{3+} ions. Under excitation at 255 nm, emission spectra consisted of a dominant peak at 610 nm and PL intensity increased with increasing calcination temperature. The increase in PL intensity was attributed to the increase in grain size, improvement in crystallinity, and removal of surface defects, which acted as luminescent quenchers. The maximum PL was found at 8% of Eu^{3+} ions. The lifetime was also decreased with increasing Eu^{3+} ion concentration. It was also found that the emission bands around 580 and 610 nm were broadened in the case of small size particles. The plausible reason as given was the different structural parameters of the host lattice.

Xinyu *et al.* [17] reported the luminescent properties of cubic and monoclinic Gd_2O_3:Eu, which were synthesized via combustion route by varying urea ratio and calcination temperature. The cubic phase of the Gd_2O_3 transformed into the monoclinic phase when the calcination temperature was in between 1200 and 1300 ℃. PLE spectra monitored at 611 nm consisted of HAB and CT around 220 and 230-250 nm, respectively. The emission peaks at 254 nm excitation were observed corresponding to Eu^{3+} transitions in the region from 560 to

720 nm. It was found that the main emission peak of cubic and monoclinic were located at 611 nm, and 625 nm with a shoulder peak at 611 nm, respectively. The difference in the main peak was associated to the difference in the local environments of the dopant ions in these phases (cubic and monoclinic). However, when both phases were present, the prominent peak ($^5D_0 \rightarrow {}^7F_2$) was located between 611 and 625 nm. It was concluded from their study that there were three non-equivalent sites (A, B, and C) and two sites (C_2 & S_6) in monoclinic and cubic Gd_2O_3, respectively.

Liu *et al.* [18] investigated the different sites in Gd_2O_3:Eu^{3+} using the spectral technique via recording site-selective excitation (SSE) spectra. It was further found that host and charge transfer bands (CTB) in excitation spectra in cubic phase were almost equal for particles having size around 135 nm, while CTB band dominated for sizes less than 23 nm. When the size was further reduced from 135 to 15 nm, quantum efficiencies were reduced from 23.6 to 4.6% for $^5D_0$, which was explained on the basis of increased surface to volume ratio. Their study led to the conclusion that the cubic and monoclinic Gd_2O_3 show different PL and PLE properties. Iwako and co-workers [57] also studied the luminescent properties of cubic and monoclinic Gd_2O_3:Eu phosphors. These two phases were obtained via varying the flame temperature in flame spray pyrolysis method. The phase transformation was observed when the flame temperature changed from 1375 to 2050 K. The transformation of the monoclinic phase from the cubic phase took place at 1873 K. In cubic phase, PL intensity enhanced linearly with increase in flame temperature until it transformed into monoclinic phase. For cubic phase, PL intensity at 1733 K was 3 times higher than that at 1375 K. Further, it was noticed that the main peaks in cubic and monoclinic phases were located at 611 and 622 nm, respectively. The emission spectrum was much narrower and stronger in case of cubic phase. The intensity of the peak at 611 nm in the cubic phase synthesized at 1733 K was twice the peak at 622 nm in the monoclinic phase synthesized at 2050 K. Hence, it was concluded that the emission intensity in cubic phase was more than monoclinic phase.

Zhang *et al.* [19] studied the structural stability of Gd_2O_3 by in-situ high-pressure (up to 18.9 GPa) luminescence spectra monitored at room temperature using europium ions as a probe. The results revealed that pressure-induced phase transformation from cubic to hexagonal took place around 11.3 GPa. The strongest emission line at 611.3 nm lost its intensity drastically above 11.3 GPa and almost disappeared at 16.4 GPa. Meanwhile, the peak intensity at 630 nm was gradually increased with applied pressure and became the strongest peak above 14.3 GPa. The appearance of the peak at 630 nm was considered as the evolution of the hexagonal phase under high pressure. The luminescence spectrum of the sample during

decompression was also studied. The hexagonal high-pressure phase was retained for the pressure lower than 7.7 GPa, but a new weak peak at 625 nm appeared at 4.9 GPa, and its intensity dominated over the other peaks till ambient pressure. At the same time, the weak peak at 615 nm became stronger with releasing pressure. The two sharp peaks around 615 nm and 625 nm originated in the monoclinic Gd_2O_3. Thus, their study concluded that the Eu^{3+} ions could be used as a probe to study the structural phase transformations in Gd_2O_3.

2.3.2 Effect of Calcination Temperature: Lin *et al.* [30] reported the effect of variation in Eu^{3+} doping concentration (3-15%) and calcination temperature (800-1000 ℃) in Gd_2O_3. The excitation spectra (λ_{emi}= 612 nm) consisted of peaks at 254 nm (CT band), and the broadband at 312 nm was due to Gd^{3+} transitions, indicating $Gd^{3+}\rightarrow Eu^{3+}$ energy transfer process. The other excitation peaks around 365, 380, and 390 nm were due to europium ions. 7% europium ion and 1000 ℃ sintering temperature were the optimized doping concentration and sintering temperature for maximum PL intensity in Gd_2O_3. The cause of the increasing PL intensity was the improvement in crystallinity with increasing calcination temperature. CL emission was also found to be maximum for 7% Eu^{3+} concentration. Flores-Gonzalez and workfellows [58] have also investigated the PL properties of Gd_2O_3:Eu by varying the sintering temperature under excitation at 254 nm. It was found that the intensity of the samples sintered below 700 ℃ was less. This was ascribed to the presence of organic residues i.e. -OH group of the DEG, which acted as the luminescent sink. Further, it was observed that the PL properties changed with the crystallite size at a given temperature and crystallite size did not vary with Eu^{3+} concentration. The sample with 20 wt% Eu^{3+} concentration synthesized at 300 ℃ showed maximum PL as the crystallite size was 4 nm. However, for annealed samples, maximum PL was found at 5 wt% Eu with crystallite size 35 nm at 700 ℃, and after that concentration quenching followed.

***2.3.3 Effect of Morphology*:** The morphological features of the luminescent materials play a significant role, and the same was demonstrated by Seo *et al.* [59]. They compared the PL spectra of Eu and Tb doped Gd_2O_3 phosphors having different morphologies i.e. nanospheres and nanoplates. It was found that PL intensity increased from nanoplates to nanospheres. PLE spectra consisted of broadband from 250 to 300 nm, resulting in host absorption and charge transfer transitions. The peak at 260 nm was for the charge transfer band. Another broadband around 280 nm was associated to the $Gd^{3+}\rightarrow Eu^{3+}$ energy transfer process. The variation in the PL intensity was attributed to several factors. First of all, due to the geometry difference in nanoplates and nanospheres, nanoplates had high surface to volume ratio, which led to more

europium ions close to surface with modified site symmetry. Initially, concentrations of Eu^{3+} ions was 10 mol%. However, ICP results indicated that the concentration of Eu^{3+} ions were 1.9 and 6.1 mol% in nanoplates and nanospheres, respectively. This indicated the strong connection between the shape of particles and dopant concentration. The other factor which affected the doping efficiency was the difference in the crystal structure of Gd_2O_3:Eu^{3+} nanocrystals. It was found that cubic Gd_2O_3 exhibited better luminescent properties than the monoclinic phase. The same results were found for Tb^{3+} doped Gd_2O_3 samples. Yang *et al.* [60] studied the size tailored luminescent properties of Gd_2O_3:Eu nanorods and micro-rods. It was observed that both Gd_2O_3:Eu micro-rod and nanorod exhibited the same PL properties except variation in their luminescent intensity. The excitation spectra on monitoring at 610 nm consisted of HAB, CTB, and excitation peaks due to Gd^{3+} and Eu^{3+} ions. It was found that PL intensity of the microrods was higher when compared to nanorods. The anomalous behavior was due to high surface area of the nanoparticles, which resulted in the surface defects. This led to an increase in non-radiative rates during hole-electron recombination, causing decreased PL intensity.

***2.3.4 Core-Shell Structures*:** The core-shell structures are more favorable to increase the biocompatibility of the materials. The coating with different materials results in different optical properties. Liu *et al.* [61] studied the luminescent features of silica-coated Gd_2O_3:Eu phosphors. PLE spectra consisted of broadband at 260 nm due to Eu-O charge transfer, which was not observed in the bulk samples. The weak peak at 277 nm originated due to $^8S \rightarrow {}^6I$ transition of Gd^{3+} ions. It was observed that bare and coated Gd_2O_3:Eu phosphors had peaks corresponding to Gd^{3+} ions' transitions. The peaks near 396 and 466 nm were associated with Eu^{3+} ions's transitions. The emission spectra at 260 nm excitation consisted of peaks at 576, 610, 649, 699, corresponding to $^5D_0 \rightarrow {}^7F_{0,1,2,3}$ transition of Eu^{3+} ions. It was found that the silica-coated samples had broad-spectrum as compared to bare ones. This was because coating with silica decreased the particle size, which increased the surface area and volume atom percentage of the interface. This led to the increase in the surface defects, and the density of the defects between the surface and the interior was different, which resulted variation in the bond length of the surface and interior. The bond length of the interface had broader distribution; thus, the energy was not uniform, and hence energy levels got broadened, and so the emitting peaks were also broadened. Anh *et al.* [62] also reported the effect of silica coating on the luminescent properties of Gd_2O_3:Eu phosphors. Under excitation at 270 nm, PL emission spectrum consisted of major peaks at 590, 611, 625, 650, and 705 nm. However, in silica-

coated samples, a new peak at 621 nm was also observed whose intensity increased with increase in silica thickness. It was believed that the silica introduction altered the transformation mechanism of gadolinium hydroxyl carbonate to gadolinium oxide. The excitation spectra of Gd_2O_3:6%Eu^{3+}@silica monitored at 621 nm consisted of peaks around 362, 380, 394 (highly intense), and 465 nm. However, the intense peak in the PLE spectrum of bare Gd_2O_3:6%Eu^{3+} was observed at 465 nm. The variation in the strongest peak in the bare and coated Gd_2O_3:Eu^{3+} samples also indicated crystal reforming in Gd_2O_3 nanophosphor, which caused the new transition channel's evolution in the energy levels ($^5D_0 \rightarrow {}^7F_2$). Thus, Eu^{3+} ions can be used as optical probes for the detection of structural changes in solid-state. Aldalbahi *et al.* [14] studied the mesoporous silica modified luminescent Gd_2O_3:Eu phosphors synthesized via sol-gel method. It was observed that the coating of amorphous mesoporous silica quenched the luminescence, which was further quenched with another silica coating. The plausible reason for the decrease in the luminescent intensity was multi-photon relaxation pathways due to the presence of silanol groups.

In another study, Gayathri *et al.* [63] investigated the influence of silica coating on the luminescent properties of Gd_2O_3:Eu phosphors synthesized via polyol method using TEG (Triethylene Glycol) medium. At λ_{emi}= 611 nm, PLE spectra consisted of a broad peak at 264 nm (CT band). The other peaks at 276 nm ($^8S \rightarrow {}^6I$) and 314 nm ($^6P \rightarrow {}^8S$) were due to Gd^{3+} ions' transitions. The peaks in higher wavelength regions were corresponding to the Eu^{3+} ions's transitions. The emission spectra on excitation at 264 nm consisted of characteristic Eu^{3+} ions' peaks. However, the intensity of the silica-coated sample was less as compared to the bare samples. It was concluded that nanoparticles were coated with silica, and a TEG layer was sandwiched between the Gd_2O_3:Eu core and silica shell structure. During excitation, TEG prevented the light to enter into Gd_2O_3:Eu core, which contributed to lower the excitation intensity after coating. In the same way, TEG also reduced the amount of emitted light and thereby reduced the emission intensity. In the light of core-shell structures, Peng and co-workers [64,65] synthesized biocompatible Fe_3O_4@Gd_2O_3:Eu^{3+} core-shell nanocomposites via hydrothermal and precipitation methods. Under λ_{emi}= 613 nm, PLE spectra consisted of a broad CT band at 254 nm and HAB at 230 nm. At 230 nm excitation wavelength, the dominant peak was observed at 613 nm. The characteristic emission and excitation peaks were observed to be the same for the bare and nanocomposites. The decrease in the luminescent intensity was observed for Fe_3O_4@Gd_2O_3:Eu^{3+}. This was attributed to the presence of black magnetite core on the surface of Gd_2O_3:Eu^{3+} phosphor. Though the luminescent intensity of the as-synthesized

nanophosphors was quenched due to the black magnetite core, they still find potential applications in the biomedical fields.

2.3.5 Effect of Non-Rare Earth Ion Co-doping: It was found that PL properties enhanced several folds with co-doping of non-rare earth elements. The effect of the alkali metal ion co-doping in Gd_2O_3:Eu phosphors was studied by Dhananjay *et al.* [24,25]. Gd_2O_3:Eu samples were synthesized via combustion route and monoclinic phase was obtained as a major phase along with small fractions of the cubic phase. Their study concluded that the alkali metals ion enhanced the PL properties of Gd_2O_3:Eu by several times. The addition of the alkali metal ions generates oxygen vacancies, increases the charge transfer rate, and increases the PL properties of Gd_2O_3:Eu. In another study, Kumar *et al.* [66] showed the effect of Li^+ co-doping in cubic Gd_2O_3:Eu synthesized via solvothermal method using diethylene as the medium. The intensity of Li^+ co-doped sample ($Gd_{1.75}Eu_{0.1}Li_{0.15}O_3$) was 1.83 times than $Gd_{1.9}Eu_{0.1}O_3$ sample. The enhancement in the PL intensity was attributed to the modifications in the crystal lattice parameters and distortion of the local symmetry around the europium ions. It was concluded that Li^+ ions acted as flux and sensitizer for the luminescence by reducing the symmetry around the activator ions in the host lattice.

2.4 Gaps in Study

Peer-review of the literature survey revealed that wet-chemical routes are the efficient methods for synthesizing nanosized Gd_2O_3:Eu phosphors. The majorly opted chemical pathways for the synthesis are hydrothermal, sol-gel, co-precipitation and combustion method. Among these aforesaid synthesis routes; co-precipitation is a facile, economical, and simple route over the other methods. In case of hydrothermal method, special apparatus are required, and yield is small. The extent of agglomeration is high in the case of sol-gel process. The formation of mixed phases and the usage of organic fuels hinders the use of the combustion method. For intense and color pure emission spectra; nanosized, mono-disperse, crystalline, and impurity (especially organic residues) free phosphors are required. For this purpose, co-precipitation method is a promising route. There are very limited reports on the synthesis of Gd_2O_3:Eu phosphors via co-precipitation method. Moreover, the systematic variation of Eu ions in the Gd_2O_3 lattice is not studied so far. Many researchers have studied the emission and excitation spectra of Gd_2O_3:Eu phosphors. However, literature still lacks in the theoretical understanding of photometric parameters of Gd_2O_3:Eu such as Judd Ofelt parameters, stimulated cross-sectional area, branching ratios, and lifetimes. It is found that the incorporation of alkali and alkaline earth metals in the host lattice alters the luminescent

properties. Dhananjaya *et al.* [25] and Kumar *et al.* [66] investgated the significant enhancement in the emission intensity of Gd_2O_3:Eu phosphors with the incorporation of Li^+ ions. In one of the studies, Dhananjaya *et al.* [24] incorporated 1 mol% of alkali metal (Li^+, Na^+ and K^+) ions in the mixed phased $Gd_{1.96}Eu_{0.04}O_3$ host lattice. However, so far no systematic study related to the incorporation of alkali and alkaline-earth metals on the luminescent properties of the Gd_2O_3:Eu has been done. There are reports in which decrease in agglomeration and variations in morphologies is achieved using surfactants/templates during synthesis. The luminescent properties vary significantly with the agglomeration and morphologies. However, variations in the structural, morphological, and emission features of Gd_2O_3:Eu using different surfactants/templates have not been studied extensively.

2.5 Objectives

Considering the abovementioned gaps in the study, the following objectives have been proposed**:**

1. To study the effect of variation in Eu^{3+} doping concentration, pH and temperature on morphological and optical properties of Gd_2O_3 synthesized via co-precipitation route.
2. To study the effect of co-doping of Eu^{3+} and Alkali (Li^+, Na^+, and K^+)/ Alkaline-earth metal (Mg^{2+}, Ca^{2+}, Ba^{2+}, and Sr^{2+}) on morphological and optical properties of Gd_2O_3.
3. To study the effect of surfactants/templates like, CTAB, PVP, TOPO, etc. on morphological and optical properties of Eu doped Gd_2O_3.

The synthesis methodology and processing parameters of Eu doped, alkali and alkaline-earth metals co-doped, and surfactant/template assisted synthesis of Gd_2O_3 phosphors are discussed in the next chapter.

References

1 N. Dhananjaya, H. Nagabhushana, S. C. Sharma, B. Rudraswamy, C. Shivakumara and B. M. Nagabhushana, *J. Alloys Compd.*, 2014, **587**, 755–762.

2 H. Guo, N. Dong, M. Yin, W. Zhang, L. Lou and S. Xia, *J. Phys. Chem. B*, 2004, **108**, 19205–19209.

3 G. Tian, Z. Gu, X. Liu, L. Zhou, W. Yin, L. Yan, S. Jin, W. Ren, G. Xing, S. Li and Y. Zhao, *J. Phys. Chem. C*, 2011, **115**, 23790–23796.

4 G. Liu, S. Zhang, X. Dong and J. Wang, *J. Nanomater.*, 2010, **2010**, 2–7.

5 Y. Shao, X. Tian, W. Hu, Y. Zhang, H. Liu, H. He, Y. Shen, F. Xie and L. Li, *Biomaterials*, 2012, **33**, 6438–6446.

6 A. Hedlund, M. Ahrén, H. Gustafsson, N. Abrikossova, M. Warntjes, J.-I. Jonsson, K. Uvdal and M. Engstro, *Int. J. Nanomedicine*, 2011, **6**, 3233–3240.

7 R. M. Petoral, F. So, A. Klasson, A. Suska, M. A. Fortin, P. Ka and M. Engstro, *J. Phys. Chem. C*, 2009, **113**, 6913–6920.

8 L. Faucher, M. Tremblay, J. Lagueux, Y. Gossuin and M. Fortin, *ACS Appl. Mater. Interfaces*, 2012, **4**, 4506–4515.

9 T. Qin, G. Mountjoy, N. D. Afify, M. F. Reid, Y. Y. Yeung, A. Speghini and M. Bettinelli, *Phys. Rev. B - Condens. Matter Mater. Phys.*, 2011, **84**, 1–14.

10 M. Bettinelli, F. Piccinelli, A. Speghini, J. Ueda and S. Tanabe, *J. Lumin.*, 2012, **132**, 27–29.

11 K. Munirathnam, G. R. Dillip, B. D. P. Raju, S. W. Joo, S. J. Dhoble, B. M. Nagabhushana, R. Hari Krishna, K. P. Ramesh, S. Varadharaj Perumal and D. Prakashbabu, *Appl. Phys. A Mater. Sci. Process.*, 2015, **120**, 1615–1623.

12 K. M. Lin and Y. Y. Li, *Nanotechnology*, 2006, **17**, 4048–4052.

13 G. Xia, S. Wang, S. Zhou and J. Xu, *Nanotechnology*, 2010, **21**, 345601.

14 A. Aldalbahi, M. Rahaman and A. A. Ansari, *J. Sol-Gel Sci. Technol.*, 2019, **89**, 785–795.

15 L. Liu, E. Ma, R. Li, G. Liu and X. Chen, *Nanotechnology*, 2007, **18**, 1–6.

16 Y. Li and G. Hong, *J. Lumin.*, 2007, **124**, 297–301.

17 Y. Xinyu, G. Wengui, X. Libin, N. Huaping and Z. Weidong, *J. Rare Earths*, 2010, **28**, 345–350.

18 L. Chunxu, L. Junye and D. Kai, *J. Phys. Chem. B*, 2006, **110**, 20277–20281.

19 C. C. Zhang, Z. M. Zhang, R. C. Dai, Z. P. Wang and Z. J. Ding, *J. Nanosci. Nanotechnol.*, 2011, **11**, 9887–9891.

20 P. Taylor, K. Iwasaki and T. Matsui, 2012, **66**, 37–41.

21 S. Chaudhary, S. Kumar, A. Umar, J. Singh, M. Rawat and S. K. Mehta, *Sensors Actuators B. Chem.*, 2017, **243**, 579–588.

22 B. Liu, M. Gu, X. Liu, C. Ni, D. Wang, L. Xiao and R. Zhang, *J. Alloys Compd.*, 2007, **440**, 341–345.

23 L. G. Jacobsohn, S. C. Tornga, B. L. Bennett, R. E. Muenchausen, O. Ugurlu, T. Tseng, J. Choi and P. H. Holloway, *Radiat. Meas.*, 2010, **45**, 611–614.

24 N. Dhananjaya, H. Nagabhushana, B. M. Nagabhushana, B. Rudraswamy, C. Shivakumara, K. Narahari and R. P. S. Chakradhar, *Spectrochim. Acta - Part A Mol.*

Biomol. Spectrosc., 2012, **86**, 8–14.
25 N. Dhananjaya, H. Nagabhushana, B. M. Nagabhushana, B. Rudraswamy, C. Shivakumara and R. P. S. Chakradhar, *J. Alloys Compd.*, 2011, **509**, 2368–2374.
26 A. Jain and G. A. Hirata, *Ceram. intenational*, 2016, **42**, 6428–6435.
27 G. Z. Li, M. Yu, Z. L. Wang, J. Lin, R. S. Wang and J. Fang, *J. Nanosci. Nanotechnol.*, 2006, **6**, 1416–1422.
28 R. G. A. Kumar, S. Hata, K. Ikeda and K. G. Gopchandran, *Ceram. Int.*, 2014, **40**, 2915–2926.
29 T. Selvalakshmi, S. Sellaiyan, A. Uedono and A. C. Bose, *Mater. Chem. Phys.*, 2015, **166**, 73–81.
30 C. C. Lin, K. M. Lin and Y. Y. Li, *J. Lumin.*, 2007, **126**, 795–799.
31 T. K. Anh, P. T. M. Chau, N. T. Q. Hai, V. T. T. Ha, H. Van Tuyen, S. Bounyavong, N. T. Thanh and L. Q. Minh, *J. Electron. Mater.*, 2018, **47**, 585–593.
32 A. G. Murillo, V. H. C. Calderon, F. de J. C. Romo and D. Y. M. Velazquez, *Mater. Res.*, 2019, **22**, 1–9.
33 S. Majeed and S. A. Shivashankar, *Mater. Lett.*, 2014, **125**, 136–139.
34 G. Jia, Y. Huang, Y. Song, M. Yang, L. Zhang and H. You, *Eur. J. Inorg. Chem.*, 2009, **2009**, 3721–3726.
35 J. G. Kang, B. K. Min and Y. Sohn, *Ceram. Int.*, 2015, **41**, 1243–1248.
36 R. Priya and O. P. Pandey, *Vacuum*, 2018, **156**, 283–290.
37 T. Selvalakshmi and A. Chandra Bose, in *Advanced Materials Research*, 2012, vol. 585, pp. 105–109.
38 C. Chang, F. Kimura, T. Kimura and H. Wada, *Mater. Lett.*, 2005, **59**, 1037–1041.
39 G. Kaur, P. Sharma, R. Priya and O. P. Pandey, *J. Alloys Compd.*, 2020, **822**, 153450.
40 K. Lee, Y. Bae and S. Byeon, *Bull. Korean Chem. Soc*, 2008, **29**, 2161–2168.
41 N. Dhananjaya, H. Nagabhushana, B. M. Nagabhushana, B. Rudraswamy, C. Shivakumara and R. P. S. Chakradhar, *Phys. B Condens. Matter*, 2011, **406**, 1639–1644.
42 G. Xing, Q. Guo, Q. Liu, Y. Li, Y. Wang, Z. Wu and G. Wu, *Ceram. Int.*, 2014, **40**, 6569–6577.
43 J. Yang, C. Li, Z. Cheng, X. Zhang, Z. Quan, C. Zhang and J. Lin, *J. Phys. Chem. C*, 2007, **111**, 18148–18154.
44 Y. Liu, G. Liu, J. Wang, X. Dong and W. Yu, *Multicolor photoluminescence and energy transfer properties of dysprosium and europium-doped Gd2O3phosphors*, Elsevier Ltd, 2015, vol. 649.
45 Y. Wang, X. Bai, T. Liu, B. Dong, L. Xu, Q. Liu and H. Song, *J. Solid State Chem.*, 2010, **183**, 2779–2785.
46 S. J. Park, J. Y. Park and H. K. Yang, *J. Alloys Compd.*, 2017, **725**, 807–817.
47 Q. Zhu, J. Li, X. Li and X. Sun, *Curr. Nanosci.*, 2010, **6**, 496–504.
48 B. Qian, D. Wang, H. Wang, H. Zou, Y. Song, X. Zhou and Y. Sheng, *J. Am. Ceram. Soc.*, 2020, **103**, 356–366.
49 J. Huang, Y. Song, G. Wang, Y. Sheng, K. Zheng, H. Li and H. Zhang, *J. Alloys Compd.*, 2013, **574**, 310–315.
50 R. Priya and O. P. Pandey, *J. Lumin.*, 2019, **212**, 342–353.

51 M. L. Debasu, D. Ananias, A. G. Macedo, J. Rocha and L. D. Carlos, *J. Phys. Chem. C*, 2011, **115**, 15297–15303.

52 G. Jia, H. You, K. Liu, Y. Zheng, N. Guo and H. Zhang, *Langmuir*, 2010, **26**, 5122–5128.

53 D. Ghosh and M. N. Luwang, *J. Lumin.*, 2015, **171**, 1–8.

54 G. Li, Y. Liang, M. Zhang and D. Yu, *CrystEngComm*, 2014, **16**, 6670–6679.

55 S. Gai, P. Yang, D. Wang, C. Li, N. Niu, F. He and X. Li, *CrystEngComm*, 2011, **13**, 5480–5487.

56 D. Li, W. Qin, P. Zhang, L. Wang, M. Lan and P. Shi, *Opt. Mater. Express*, 2017, **7**, 329.

57 Y. Iwako, Y. Akimoto, M. Omiya, T. Ueda and T. Yokomori, *J. Lumin.*, 2010, **130**, 1470–1474.

58 M. A. Flores-Gonzalez, C. Louis, R. Bazzi, G. Ledoux, S. Roux, P. Perriat and O. Tillement, *Appl. Phys. A*, 2005, **1391**, 1385–1391.

59 S. Seo, H. Yang and P. H. Holloway, *J. Colloid Interface Sci.*, 2009, **331**, 236–242.

60 J. Yang, C. Li, Z. Cheng, X. Zhang, Z. Quan, C. Zhang and J. Lin, *J. Phys. Chem. C*, 2007, **111**, 18148–18154.

61 G. Liu, G. Hong and D. Sun, *J. Colloid Interface Sci.*, 2004, **278**, 133–138.

62 T. Ki. Anh, N. T. Huong, P. T. Lien, D. K. Tung, V. D. Tu, N. D. Van, W. Strek and L. Q. Minh, *Mater. Sci. Eng. B*, 2019, **241**, 1–8.

63 T. Gayathri, R. A. Kumar, B. S. Panigrahi, P. Saravanan and B. Devanand, *Mater. Res. Express*, 2019, **6**, 055037.

64 H. Peng, B. Cui and Y. Wang, *Mater. Res. Bull.*, 2013, **48**, 1767–1771.

65 H. Peng, B. Cui, L. Li and Y. Wang, *J. Alloys Compd.*, 2012, **531**, 30–33.

66 R. G. A. Kumar, S. Hata, K. Ikeda and K. G. Gopchandran, *RSC Adv.*, 2016, **6**, 67295–67307.

CHAPTER 3

EXPERIMENTAL DETAILS

Overview

This chapter discusses the experimental details for the synthesis of Gd_2O_3:Eu phosphors and their characterization to analyze their properties. All the samples were prepared via co-precipitation method, the details of which are discussed in this chapter. The synthesis procedure employed to synthesize the alkali and alkaline-earth metals co-doped and capped Gd_2O_3:4mol%Eu phosphors has been given. The synthesized samples were investigated for structural, morphological, elemental, optical, and luminescent studies, using X-ray diffraction, Fourier transform infrared spectroscopy, field emission scanning electron microscopy, UV-Visible spectroscopy, and photoluminescence techniques, respectively. The details of each characterization technique, such as the instruments used and their operating conditions, have been described in this chapter.

3.1 Raw Materials

The starting precursors used for the synthesis are: Gadolinium nitrate hexahydrate (*Alfa Aesar*, 99.99%); Europium nitrate hexahydrate (*Alfa Aesar*, 99.99%); Lithium nitrate (*Sigma Aldrich*, 99.99%), Sodium nitrate (*Sigma Aldrich*, 99.99%); Potassium nitrate (*Sigma Aldrich*, 99.99%); Magnesium nitrate hexahydrate (*HIMEDIA*, 99%); Calcium nitrate tetrahydrate (*HIMEDIA*, 99%); Strontium nitrate (*HIMEDIA*, 99%); Barium nitrate (*HIMEDIA*, 99%); Cetyltrimethylammonium bromide (*Sigma Aldrich*, 99.99%); Trioctylphosphine oxide (*Sigma Aldrich*, 99.99%); Dextran (*Alfa Aesar*); Thioglycerol (TG, *Sigma Aldrich*, 99%); Polyvinyl pyyrolidone (*Sigma Aldrich*, 99.9%); Ammonia (25 wt%, *Loba Chemie* Pvt. Limited); Ethanol (*Loba Chemie* Pvt. Limited, 99.9%) and Distilled water (D.I.). All the chemicals used in this work were in as received condition without additional purification treatment.

3.2 Synthesis Methodology

3.2.1 Synthesis of Eu Doped Gd_2O_3 Phosphors

A series of Eu^{3+} doped (1 to 5 mol%) Gd_2O_3 samples were synthesized using co-precipitation method. In a typical synthesis procedure, the stoichiometric amounts of metal ions precursors were dissolved in D.I. water under vigorous stirring to prepare 0.1 M mother solution. After stirring for half an hour, 25 wt% ammonia solution was added dropwise into the mother solution to maintain pH (8 and 10) and white precipitates were obtained. The white precipitates containing solution was kept under continuous stirring for an hour. After aging for 24 h, the obtained white precipitates were centrifuged at 10,000 rpm and washed with D.I. water followed by ethanol to remove the adhere impurities. The precipitates were oven dried at 60 °C. The dried samples were further calcined in a muffle furnace at 800 °C for 4 h. The heating rate of the furnace was set 3 °C/min. These samples were ground to form a uniform powder for further characterization. PL results exhibited that the photoluminescent quenching was obtained for concentrations beyond 4 mol% of europium ions in the Gd_2O_3 matrix. Thus, the concentration of the Eu^{3+} ions was fixed as 4 mol% to further synthesize alkali and alkaline-earth metals co-doped and surfactants/templates assisted Gd_2O_3:Eu samples.

3.2.2 Synthesis of Alkali and Alkaline-Earth Metal Ions Co-doped Gd_2O_3:4mol%Eu Phosphors

For the synthesis of alkali (AM) and alkaline-earth metals (AEM) co-doped Gd_2O_3:4mol%Eu samples, stoichiometric amount of the nitrates of the alkali and alkaline-earth metals were dissolved in the solution containing stoichiometric amount of europium and

gadolinium nitrates according to the formula $Gd_{1.96-x}Eu_{0.04}AM_x/AEM_xO_3$ (AM/AEM= Li^+, Na^+, K^+/ Mg^{2+}, Ca^{2+}, Sr^{2+}, Ba^{2+}). The concentration of the Eu^{3+} ions was fixed 4 mol% as the maximum PL intensity was found at this concentration. This was also done to avoid the chances of the concentration quenching. The concentrations of the alkali metals (Li= 1 to 6 mol%; Na= 1 to 4 mol%; K= 1 to 4 mol%) and alkaline-earth metals (Mg= 1 to 7 mol%; Ca= 1 to 5 mol%; Ba= 1 to 4 mol%; Sr= 1 to 4 mol%) were varied to observe the concentration quenching in the co-doped Gd_2O_3:Eu samples. The solution containing the dopants and co-dopants was further stirred for half an hour. To this solution, ammonia solution was added dropwise until pH 10 was obtained. The white precipitates were further aged for 24 h, centrifuged and washed several times with D.I. water and ethanol. The precipitates were further dried at 60 ℃ in an electric oven. These as-synthesized samples were calcined in a muffle furnace at 800 ℃ for 4 h. The heating rate of the furnace was 3 ℃/min. The samples were ground and used for further characterization.

3.2.3 CTAB and TOPO Assisted Synthesis of Gd_2O_3:4mol%Eu Phosphors

For the synthesis of CTAB and TOPO assisted samples, stoichiometric amount of nitrates of gadolinium and europium were dissolved in 50 ml of D.I. water under constant stirring, keeping the concentration of the mother solution as 0.1 M. The surfactants were added into the mother solution in various molar ratios such as 1:0.5, 1:1 and 1:2 (metal ion: surfactant) at 60 ℃. To this mother solution, ammonia solution was added rapidly to maintain pH 10. This resulted in the formation of white precipitates. The solution containing white precipitates was stirred at 60 ℃ for 6 h. After stirring, the mixed solution was allowed to cool down at room temperature. The obtained precipitates were centrifuged, washed and oven dried at 70 ℃ for 6 h. The synthesized samples were further calcined in a muffle furnace at 800 and 1000 ℃ for 4 h to induce crystallization. The sample labels for the CTAB and TOPO assisted Gd_2O_3:4mol%Eu samples are represented in **Table 3.1**.

Table 3.1: Sample labels for the surfactant assisted/free Gd_2O_3:4mol%Eu samples.

S. No.	Sample ID	Surfactant	Ratio (Metal ion: Surfactant)	Calcination Temperature (℃)
1.	GOE	-	-	800, 1000
2.	GOEC1	CTAB	1:0.5	800, 1000
3.	GOEC2	CTAB	1:1	800, 1000
4.	GOEC3	CTAB	1:2	800, 1000
5.	GOET1	TOPO	1:0.5	800, 1000
6.	GOET2	TOPO	1:1	800, 1000
7.	GOET3	TOPO	1:2	800, 1000

3.2.4 TG, Dextran, and PVP Assisted Synthesis of Gd_2O_3:4mol%Eu Phosphors

The stoichiometric amounts of gadolinium and europium nitrates were dissolved in 50 ml of D.I. water under constant stirring. To this 0.1 M mother solution, 10 ml of varying concentrations (0.5, 1, 1.5, 2, and 2.5 wt%) of different templates (PVP, Dextran and TG) were added dropwise under vigorous stirring. This solution was stirred for an hour for the complete mixing of the constituents. To this solution, 25 wt% of ammonia solution was added dropwise to maintain pH 10. The solution temperature was increased from room temperature to 60 ℃, and the samples were stirred at this temperature for 6 h. Finally, the solution was allowed to cool down. The obtained white precipitates were centrifuged, washed and oven dried at 70 ℃ for 6 h. The synthesized samples were further calcined at 1000 ℃ for 4 h to get the final products. The sample labels for all the template (TG, Dextran and PVP) free/directed Gd_2O_3:4mol%Eu samples are given in **Table 3.2**.

Table 3.2: Sample labels for TG, Dextran, and PVP assisted/free Gd_2O_3:4mol%Eu samples.

S. No.	Template used	Amount of template (in wt%)	Calcination Temperature (℃)	Sample ID
1.	-	-	1000	GE4
2.	Dextran	0.5, 1.0, 1.5, 2.0, 2.5	1000	D0.5, D1, D1.5, D2, D2.5
3.	PVP	0.5, 1.0, 1.5, 2.0, 2.5	1000	PVP0.5, PVP1, PVP1.5, PVP2, PVP2.5
4.	TG	0.5, 1.0, 1.5, 2.0, 2.5	1000	TG0.5, TG1, TG1.5, TG2, TG2.5

3.3 Characterization Techniques

The samples were characterized by various techniques to investigate different properties. A brief description of each technique is given in the following sections.

3.3.1 Thermogravimetric (TG) Analysis

All undoped, doped, co-doped and surfactant/template assisted Gd_2O_3 samples were synthesized via calcination of as-synthesized hydroxides, which were synthesized at different pH. The thermal behavior of the hydroxides was studied via TG/DTG curves. Thermogravimetric analysis (TGA) for the decomposition of as-synthesized precursors sample was done using Exstar TG/DTA 6300 in the nitrogen atmosphere at a heating rate of 10 °C/min.

3.3.2 X-ray diffraction (XRD)

The crystallinity, phase formation, and their crystal structures were investigated using X-ray diffraction technique. XRD patterns were recorded using Panalytical X'Pert Pro XRD diffractometer operating at 45 kV using Cu-K_α radiation as a monochromatic source of X-rays equipped with in-built Ni filter. XRD patterns were recorded in the range $10° \leq \theta \leq 80°$ with step size of 0.0131°. The obtained XRD patterns were matched with standard cards in the database of the International center for diffraction data (ICDD) with the help of ***X'Pert High Score*** software for phase identification. The crystallite size (D) of the synthesized samples are determined using Debye-Scherrer formula as follows:

$$D = \frac{K\lambda}{\beta_{corr}\cos\theta} \tag{3.1}$$

where, β_{corr} (in radians) is the full width at half maxima (FWHM), λ corresponds to the wavelength of the incident CuK_α X-rays (1.54 Å), θ is the Bragg angle, K is the constant (here, K= 0.9). The β_{corr} used in the above equations is the amalgam of instrumental and sample broadening. The value of the FWHM is corrected using silicon (Si) as the standard sample according to the following equation:

$$\beta_{corr} = [(\beta^2)_{Observed} - (\beta^2)_{Instrumental}]^{1/2} \tag{3.2}$$

The lattice parameters are calculated using the following formulas:

$$2\,d\sin\theta = n\lambda \tag{3.3}$$

$$d = \frac{a}{\sqrt{h^2+k^2+l^2}} \tag{3.4}$$

where, the terms symbols have their usual meaning.

3.3.3 Electron Microscopy

The morphological features such as variation in shape and size of the synthesized samples were studied by field-emission scanning electron microscope (FESEM). FESEM micrographs were recorded using Carl Zeiss operated at 20 kV or HITACHI-SU8010 operated at 15 kV.

3.3.4 Fourier Transform Infrared (FTIR) Spectroscopy

It is known that the presence of functional groups such as nitrates and hydroxides act as luminescent quenchers. FTIR is an analytical technique to investigate the presence of different functional groups and chemical bonds in the molecules. FTIR spectra of the

synthesized samples were recorded in the range from 400 to 4000 cm^{-1} using Perkin Elmer-Spectrum spectrometer (RX-IFTIR) using KBr pellet technique.

3.3.5 UV-Visible Spectroscopy

The bandgap of the samples varies with different parameters such as synthesis method, doping, co-doping, morphology, and crystallite size. The absorbance spectra of all the samples were recorded using double beam UV-Visible spectrometer (Hitachi-U3900H) in the range 200-800 nm. The bandgap values were determined from Tauc's plots using Tauc's formula.

3.3.6 Photoluminescence (PL)

The excitation and emission spectra of all the synthesized samples were recorded to investigate the luminescent features and determination of spectral and radiative parameters. Photoluminescent (PL) spectra of all the powdered samples were recorded using fluorescent spectrometer (Agilent Technologies-Model Cary Eclipse) equipped with a Xenon lamp. The slit width of photospectrometer were set at 5 nm for excitation and emission spectra. CIE (Internationale de l'Eclairage) coordinates of the synthesized samples were determined with the help of color calculator MATLAB program in MATLAB 9.1.

CHAPTER 4

RESULTS AND DISCUSSION I

Overview

The present chapter elucidates the effect of alkali metal ion (Li^+, Na^+, and K^+) co-doping on the morphological and optical properties of Gd_2O_3:Eu phosphors. First of all, phase pure Gd_2O_3 sample with uniform morphology was synthesized via co-precipitation route. The concentration of the Eu^{3+} ions was varied from 1 to 5 mol% in Gd_2O_3. The maximum PL intensity was obtained for the Gd_2O_3 sample with 4 mol% Eu^{3+}, synthesized at pH 10 and calcined at 800 ℃. Further, different concentrations of alkali metal ions were co-doped in Gd_2O_3:4mol%Eu to investigate their influence on the structural, morphological, and optical properties. CIE coordinates and color-coordinated temperature (CCT) values were calculated for all the samples. The radiative and Judd Ofelt parameters (Ω_2, Ω_4) were calculated to investigate the luminescent properties further. In brief, the present chapter gives an insight into the variation in the various parameters that influence the different features of Gd_2O_3:Eu phosphors with alkali metal ion co-doping and their contribution in the luminescent enhancement.

4.1 Introduction

Among all the rare-earth oxides, Gd_2O_3 is one of the most promising host matrix [1–4]. Gd_2O_3 is an ideal host matrix in the case of Eu^{3+} dopant. This is because the ionic radii of Eu^{3+} ions (0.947 Å) is close to the Gd^{3+} ions (0.938 Å) and can be easily incorporated into the Gd_2O_3 matrix. As compared to Y_2O_3:Eu, Gd_2O_3:Eu has higher strong charge transfer band and luminescent intensity. The electronegativity of the Gd^{3+} ions (1.20) is smaller than the Y^{3+} ions (1.22), which allows easier charge transfer from the 2p orbitals of oxygen to the 4f orbitals of the europium ions [5–7]**.**

Although, Gd_2O_3:Eu is a widely studied phosphor, however, there are limited investigations on the structural and luminescent properties with the alkali metal co-doping in Gd_2O_3:Eu phosphors. The existing studies revealed that Li^+ ions incorporation enhanced the luminescent properties of Gd_2O_3:Eu phosphors [8,9]. However, the effects of Na^+ and K^+ ions on the structural and luminescent properties are still less known. No systematic studies related to calculation of CIE, CCT, Judd-Ofelt, and other radiative parameters have been done so far. In one report, Dhananjaya *et al.* [10] reported the effect of alkali metal ion co-doping on the luminescent properties of mixed-phase (monoclinic and cubic) Gd_2O_3:Eu synthesized via combustion method. The emission spectra of Eu doped and alkali metal co-doped were not sharp, narrow and intense, which limit their applicability as a red light component in the solid-state lighting devices. Thus, a systematic study to visualize the effect of alkali metal co-dopants in the phase pure Gd_2O_3:Eu phosphors is required**.**

In the present work, a novel, facile, and economic co-precipitation synthesis route is reported for large scale production of Gd_2O_3:Eu phosphors. This method is simple, homogeneous, morphology controlled, and less time consuming to synthesize single-phase cubic Gd_2O_3 phosphors. It is also reported that cubic phase Gd_2O_3:Eu shows better luminescent properties than the monoclinic phase [11–13]**.** In brief, in the present chapter, systematic investigations on the structural and luminescent changes with the alkali metal (Li^+, Na^+ and K^+) co-doping in Gd_2O_3:Eu phosphors are reported. Judd-Ofelt and other spectral parameters (branching ratios, stimulated cross-sectional area, and radiative time) have been calculated as a probe to investigate the luminescent properties further. The obtained results are presented and discussed in the following sections.

4.2 Structural Analysis of As-synthesized Samples

XRD patterns of the as-synthesized precipitates obtained at pH 8 and 10, respectively, are shown in **Fig. 4.1** (a-b). All the XRD peaks correspond to the standard ICDD card (01-083-2037) of the $Gd(OH)_3$ phase with hexagonal structure and P63/m space group symmetry. No impure phase(s) due to initial precursors are observed in the XRD patterns. It represents the synthesis of pure hexagonal $Gd(OH)_3$ phase. The sharp and intense XRD peaks exhibit the formation of the crystalline $Gd(OH)_3$ phase.

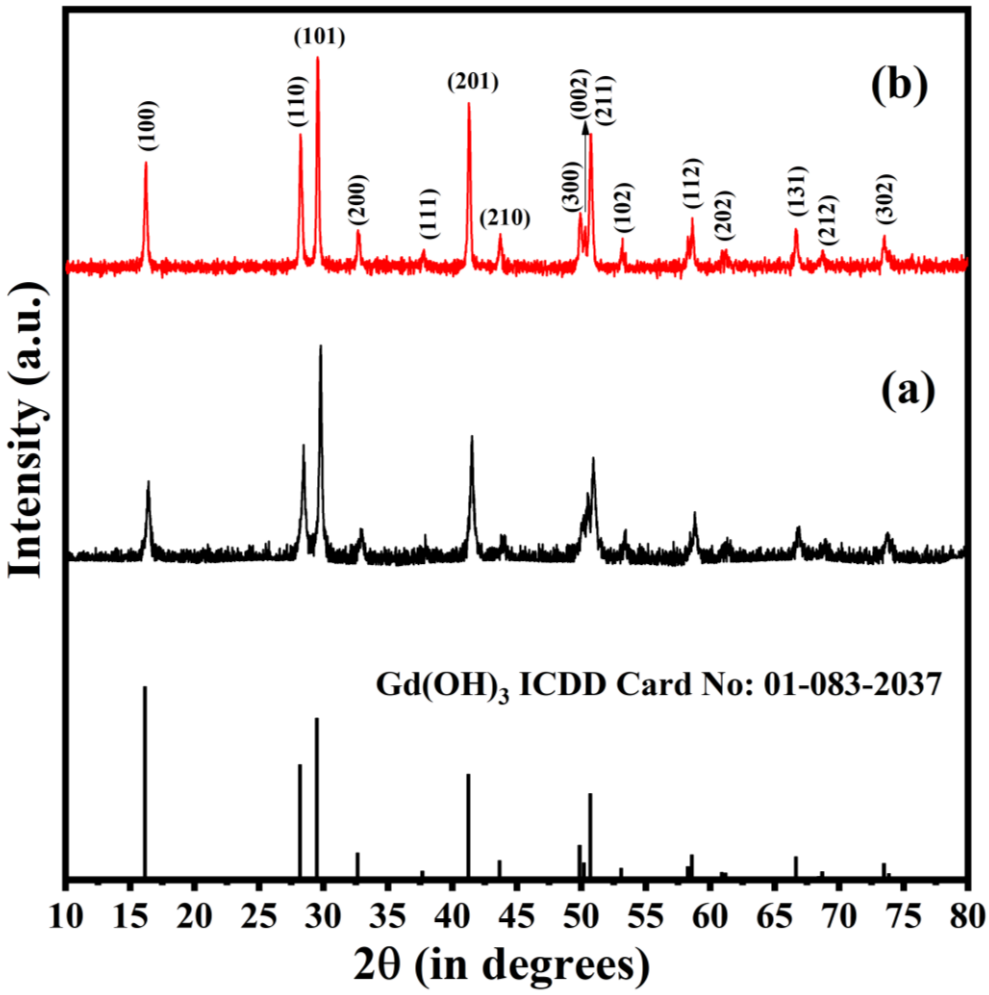

Figure 4.1: XRD patterns of the samples prepared at (a) pH 8 and (b) pH 10.

4.3 Thermal Behavior of As-Synthesized Samples

The thermal behavior of $Gd(OH)_3$ powders synthesized at different pH are analyzed via TG/DTG curves, as shown in **Fig. 4.2**. The TG curves represent two stages at which weight loss can be clearly seen. The sample synthesized at pH 8 shows different weight loss stages around 323.24 and 410.81 ℃, respectively. The weight losses corresponding to these temperatures are ~6.08 and ~6.71%, respectively. However, in the case of sample synthesized at pH 10, weight losses are observed at 306.21, and 419.41 ℃, and the corresponding weight

losses are ~8.95 and ~4.11%, respectively. The variation in the temperature and weight losses in the TG curves of samples synthesized at different pH indicates the formation of intermediate products during calcination. In literature, it is reported that lanthanide hydroxides have the LnOOH phase as an intermediate product when dehydration of $Ln(OH)_3$ takes place [14]. Based on this, the dehydration of the synthesized $Gd(OH)_3$ is considered to proceed via the following steps:

$$Gd(OH)_3 \rightarrow GdOOH + H_2O \quad (4.1)$$

$$2GdOOH \rightarrow Gd_2O_3 + H_2O \quad (4.2)$$

The total experimental weight losses for $Gd(OH)_3$ synthesized at pH 8 and 10 are 12.79 and 13.1%, respectively. These experimentally determined values are very close to the theoretical value of weight loss of $Gd(OH)_3$, i.e. 12.97% [15,16].

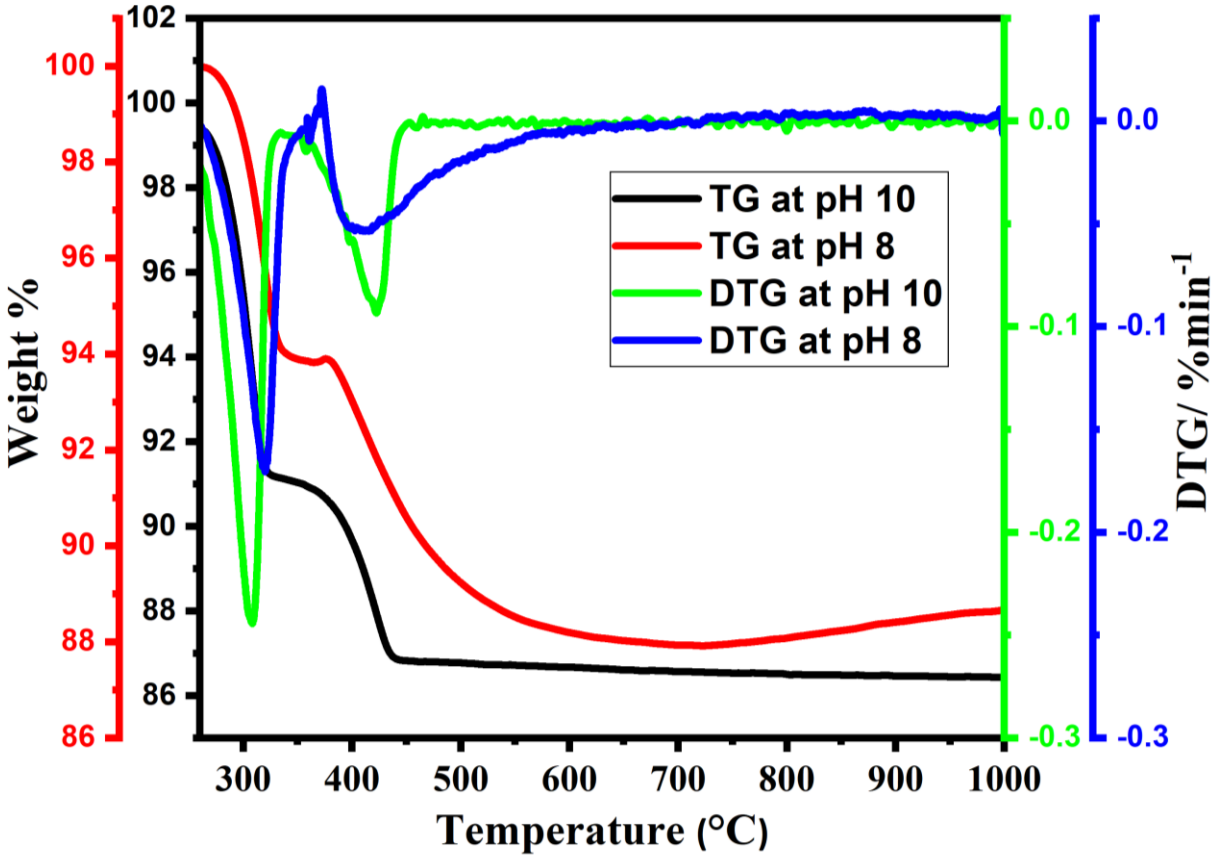

Figure 4.2: TG/DTG curves of as-prepared samples at pH 8 and 10.

4.4 XRD study of Undoped, Eu Doped and Alkali Metal Co-doped Gd_2O_3

The phase confirmation, phase purity, and average crystallite size are determined from XRD patterns. Based on the TG results, $Gd(OH)_3$ precursors are calcined at 800 ℃ to ensure the complete crystallization into the oxide phase. **Fig. 4.3 (a-b)** represents the XRD patterns of

the Gd_2O_3 synthesized at pH 8 and 10 after calcining $Gd(OH)_3$ at 800 ℃. All the XRD peaks are sharp and intense, which indicate the crystalline nature of the synthesized oxides. XRD patterns are well-matched with the International center for diffraction data (ICDD) card number 03-065-3181. The obtained XRD patterns correspond to the BCC structure of Gd_2O_3 and Ia-3 (206) group symmetry. The peak position around 28.6° corresponds to the (222) plane. No impurity peak(s) due to precursors are found. This shows that hydroxides are completely converted into oxides.

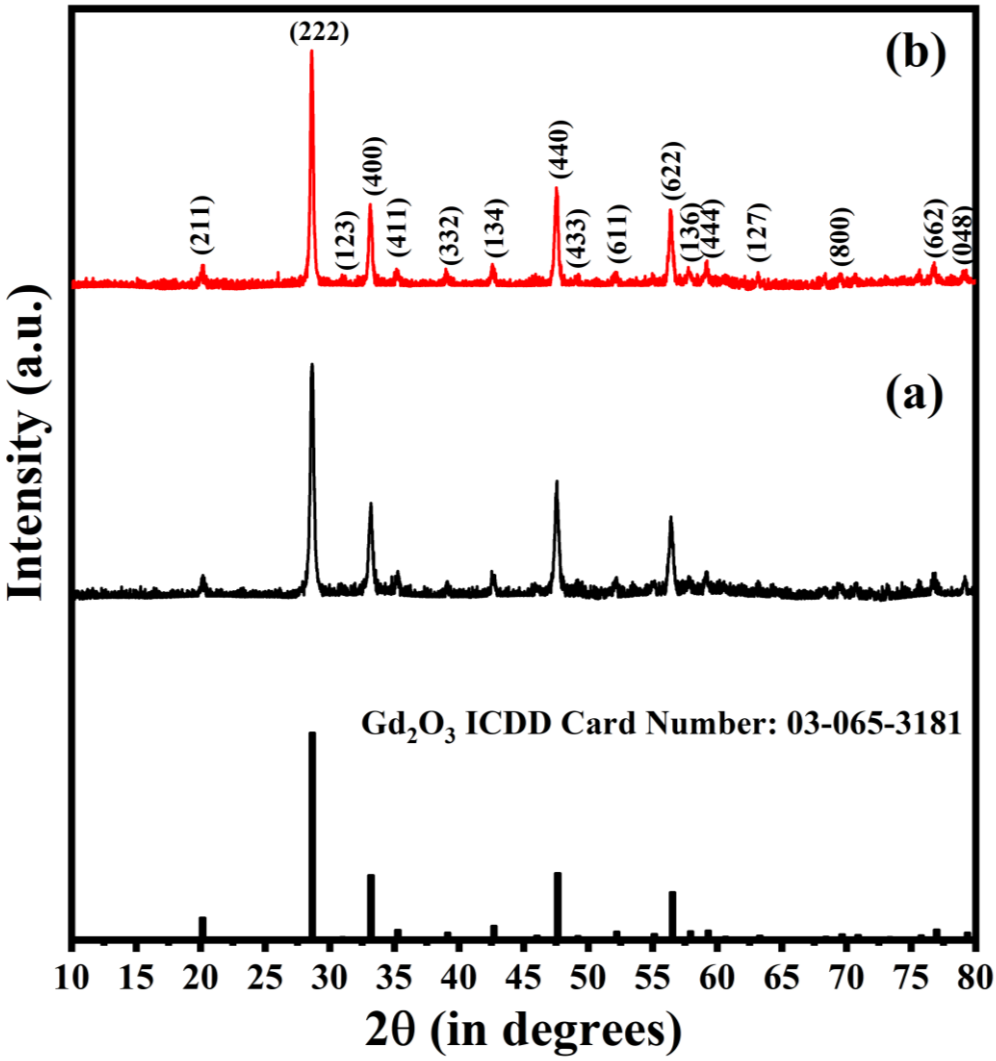

Figure 4.3: XRD patterns of samples synthesized at (a) pH 8 and (b) pH 10 and calcined at 800 ℃.

Fig. 4.4 represents the XRD patterns of the Gd_2O_3 doped with varying concentrations of Eu synthesized at pH 10 and 800 ℃. XRD patterns of all the samples correspond to the formation of single cubic Gd_2O_3 phase. No additional peak(s) due to Eu_2O_3 or other phases are found. This indicates that dopant ions are incorporated into the host lattice. It can be observed that XRD peaks of the samples doped with the Eu^{3+} ions are shifted slightly towards the left

side. This is owing to the incorporation of the large-sized Eu^{3+} ions (ionic radii= 0.0947 Å) in the place of Gd^{3+} ions (ionic radii= 0.0938 Å). The average crystallite size (D) of all the doped samples is determined using Debye-Scherrer formula and found in the range 26-50 nm [16].

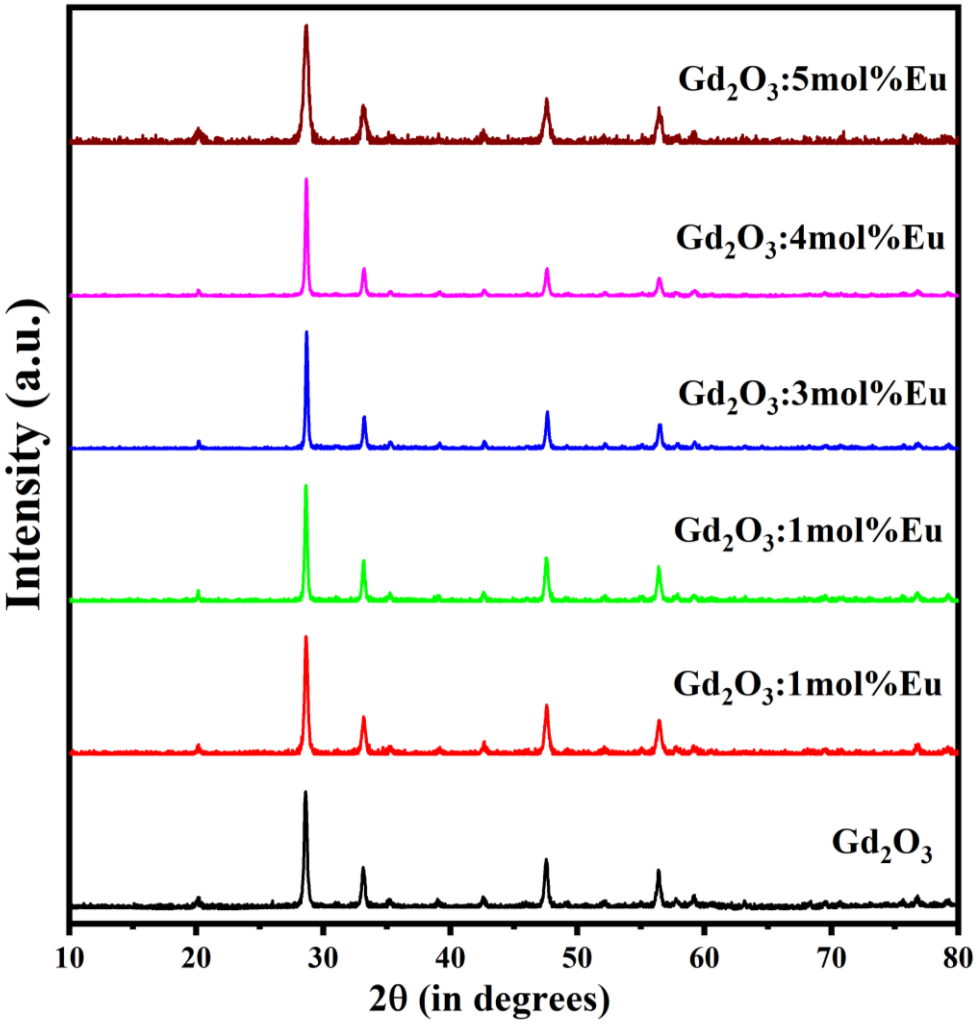

Figure 4.4: XRD patters of undoped and Eu (1-5 mol%) doped Gd_2O_3 (pH=10) calcined at 800 ℃.

Fig. 4.5 (A) represents the XRD patterns of alkali metal ions co-doped Gd_2O_3:4mol%Eu phosphors. A small variation in the peak position in the XRD pattern (peak shifting) is observed with alkali metal ion co-doping. The peak shifting corresponding to the (222) plane is shown in **Fig. 4.5 (B)**. The peak shifting has been observed due to the difference in the ionic radii of alkali metal ions ($r_{lithium}$= 0.76 Å, r_{sodium}= 1.02 Å, $r_{potassium}$= 1.38 Å) and Gd^{3+} ions. Upon lithium incorporation, XRD peaks have shifted towards the right side owing to decrease in the lattice parameters of the host matrix. The average crystallite size (D) of the samples is determined for the peak corresponding to (222) plane using Debye Scherrer equation [17].

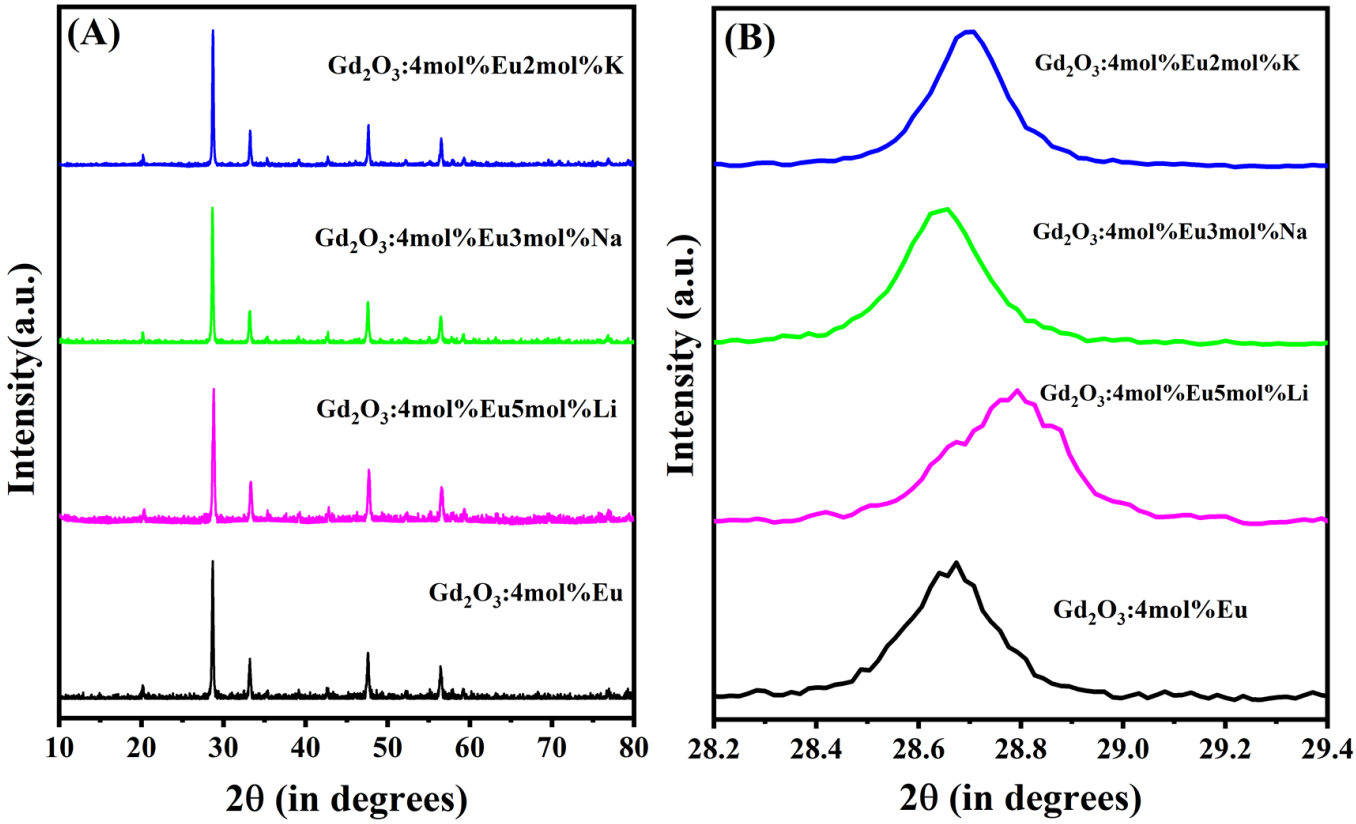

Figure 4.5: (A) XRD patterns of Eu doped and alkali metal co-doped Gd_2O_3 samples and (B) corresponding peak shifting in the (222) plane with different doped ion concentrations.

The lattice parameters (a) w.r.t. (222) plane are calculated using following formula:

$$\sin^2 \theta = \lambda^2 / \{4\, a^2\, (h^2 + k^2 + l^2)\} \qquad (4.3)$$

The calculated values of average crystallite size and lattice parameters are given in **Table 4.1**.

Table 4.1: XRD crystal structure parameters and bandgap values of alkali metal ions co-doped Gd_2O_3:Eu phosphors.

Sample name	Plane	FWHM (in degrees)	2 Theta (in degrees)	Crystallite size (nm)	Lattice parameter (Å)	Bandgap (eV)
Gd_2O_3:4%Eu	(222)	0.1851	28.66	44.27	10.77	4.78
Gd_2O_3:4%Eu5%Li	(222)	0.2488	28.77	32.94	10.73	5.11
Gd_2O_3:4%Eu3%Na	(222)	0.1718	28.64	47.68	10.78	4.94
Gd_2O_3:4%Eu2%K	(222)	0.1506	28.69	54.39	10.76	4.95

4.5 Morphological Studies

Fig. 4.6 (A-B) represents the micrographs of the Gd_2O_3:4mol%Eu calcined at 800 ℃ and synthesized at pH (8 and 10) conditions. **Fig. 4.6 (A)** illustrates that the samples synthesized at pH 8 do not have particular morphology. The sample consists of irregular shape particles having rod like features. The length of the rods is found to be in the range 200-400 nm and diameter around 90-150 nm. The average size of the particles lies in the range 55-90 nm. However, samples synthesized at pH 10 (**Fig. 4.6 (B)**) have uniform rod-like morphology. The formation of the rod-like structure is related to the self or induced scrolling mechanism [18]. The rods are highly uniform and nano-sized in nature. The diameter of the rods varies in the range 70-120 nm, and the length around 200-500 nm.

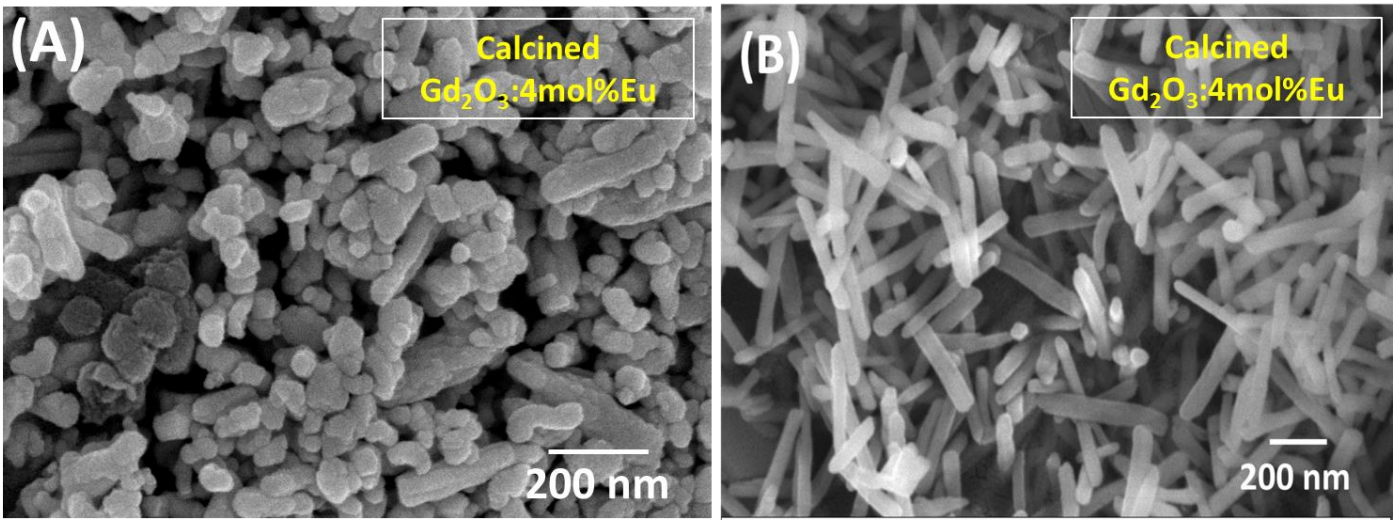

Figure 4.6: FESEM micrographs of Gd_2O_3:4mol%Eu phosphors synthesized at (A) pH 8 and (B) pH 10.

Fig. 4.7 (A-C) represents the FESEM images of the alkali metal (Li^+, Na^+ and K^+) ion co-doped Gd_2O_3:4mol%Eu samples synthesized at pH 10 and calcined at 800 ℃. All the samples represent uniform rod-like morphology. The co-doping of the alkali metal ions affected the length of the rod. The average length of the rods is in the micrometer regime, and diameters are in the range 70-120 nm.

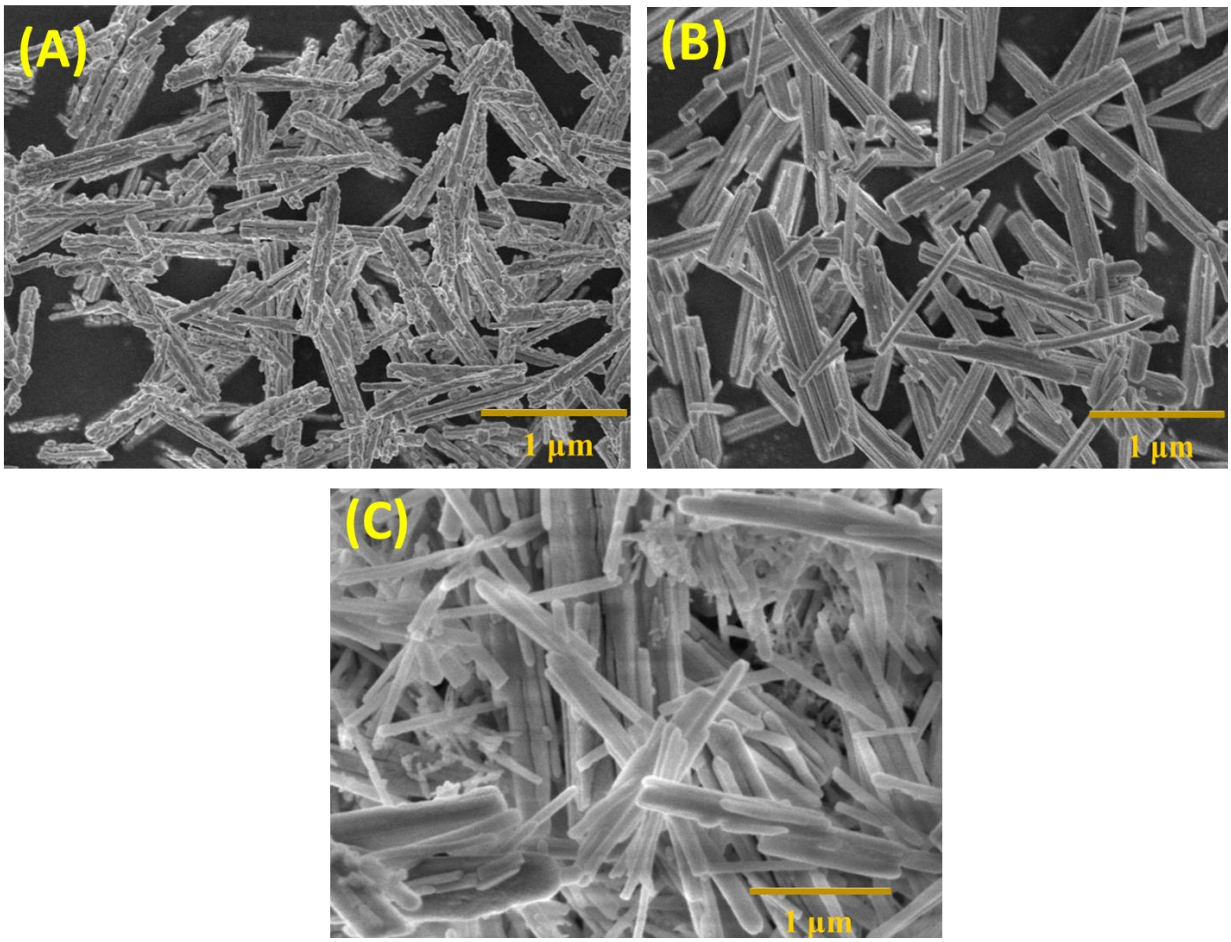

Figure 4.7: FESEM micrographs of (A) Gd_2O_3:4mol%Eu5mol%Li, (B) Gd_2O_3:4mol%Eu3mol%Na, and (C) Gd_2O_3:4mol%Eu2mol%Li synthesized at pH=10 and 800 ℃.

4.6 Fourier Transform Infrared (FTIR) Analysis

FTIR spectra of the as-prepared (a) 4 mol% Eu doped and (b-d) 5 mol% Li, 3 mol% Na and 2 mol% K co-doped Gd_2O_3 phosphors, respectively, are shown in **Fig. 4.8 (A)**. The weak band at 3439 cm^{-1} is attributed to the absorption of water molecules. The peak around 3619 cm^{-1} is ascribed to Gd-OH vibration, which is further confirmed by the out of the plane OH mode of γ-OH [19]. The small intensity peaks around 1494 and 1379 cm^{-1} are for the carbonate (CO_3^{2-}) ions, which come into existence due to the absorption of CO_2 from the atmosphere. The band around 1629 cm^{-1} is attributed to the nitrate (NO_3^{2-}) ions [20]. **Fig. 4.8 (B)** represents the FTIR spectra of calcined samples. It can be seen from **Fig. 4.8 (B)** that sharp OH absorption peak around 3619 cm^{-1} has vanished in calcined samples, which confirms the formation of oxide samples. The peaks at 1514, 1398, and 1122 cm^{-1} are corresponding to the CO symmetric and asymmetric stretching vibrations. The peak position centered around 550 cm^{-1} is attributed to Gd-O stretching vibration. FTIR results also confirm that the calcined samples are free from

nitrate groups (1629 cm^{-1}) [18]. This suggests that the as-synthesized samples have transformed into the oxides after calcination at 800 ℃. FTIR results are consistent with the XRD results.

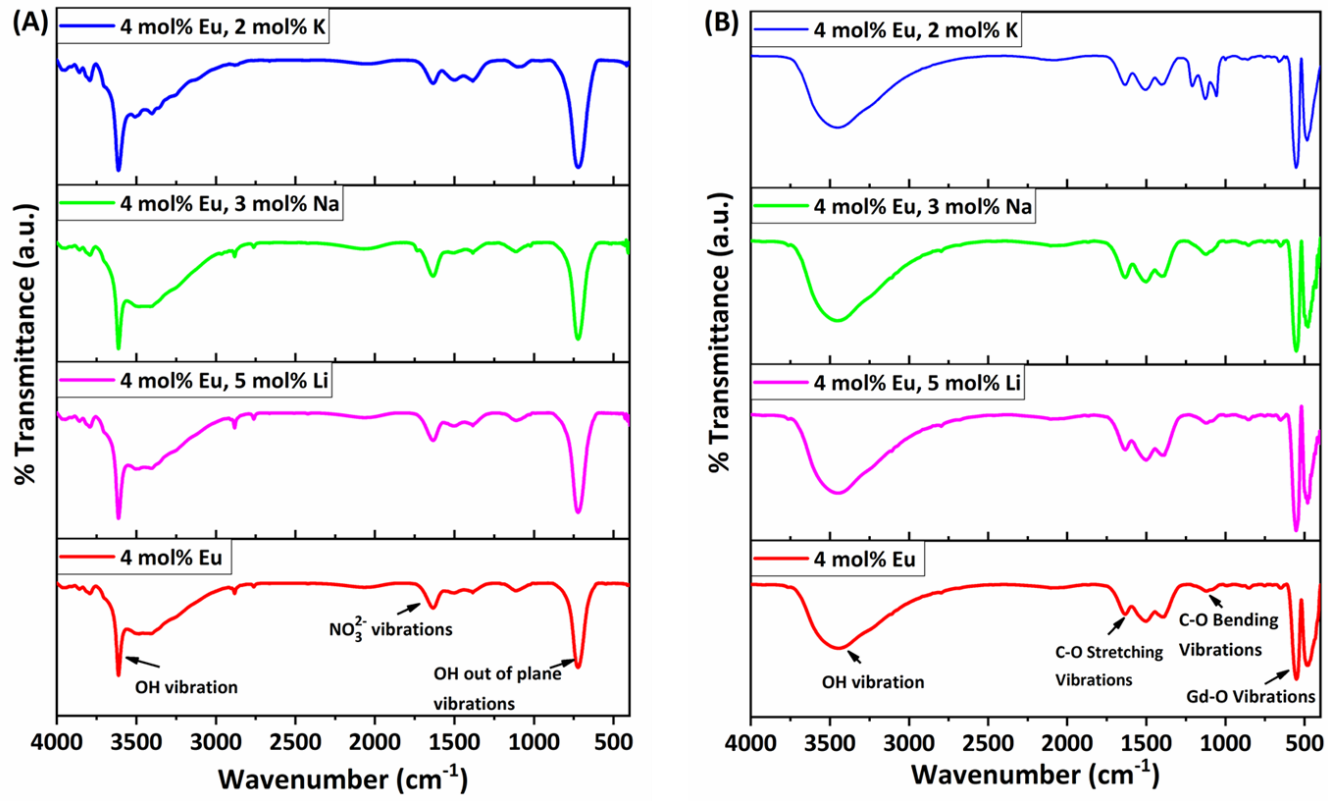

Figure 4.8: (A) FTIR spectra of as-prepared Gd_2O_3:4mol%Eu, Gd_2O_3:4mol%Eu5mol%Li, Gd_2O_3:4mol%Eu3mol%Na, Gd_2O_3:4mol%Eu2mol%K and (B) FTIR spectra after calcination at 800 ℃, respectively.

4.7 UV-Vis Measurements

The bandgap of europium doped and alkali metal ions co-doped Gd_2O_3 are calculated by plotting the Tauc plots. According to Tauc's formula [21], the relation between absorption coefficient (α) and incident photon energy (hν) is expressed as:

$$\alpha h\nu = A(h\nu - E_g)^n \quad (4.4)$$

where, α is absorption coefficient, A is a constant, and value of n = ½, 2, 3/2 or 3 corresponds to the allowed direct, allowed indirect, forbidden direct or forbidden indirect transition, respectively. The oxides are characterized by an indirect allowed transition, and therefore the value of the n is taken as 2. The graph is plotted between $(\alpha h\nu)^2$ versus hν. The bandgap is determined by extrapolating the linear portion of $(\alpha h\nu)^2$ to x-axis, where hν = 0.

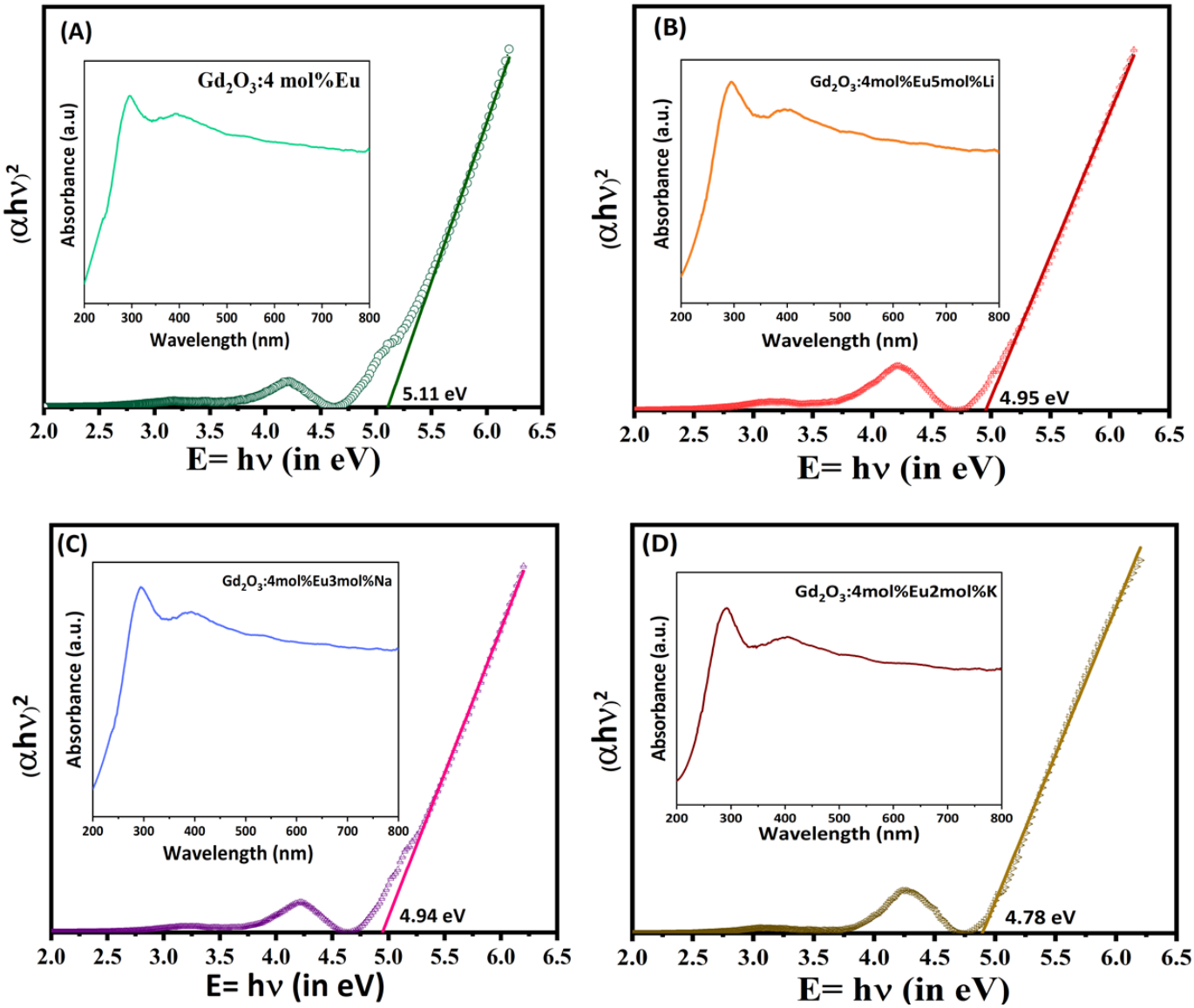

Figure 4.9: Tauc Plots of (A) Gd_2O_3:4mol%Eu, (B) Gd_2O_3:4mol%Eu5mol%Li, (C) Gd_2O_3:4mol%Eu3mol%Na, (D) Gd_2O_3:4mol%Eu2mol%K and inset showing the actual UV-Visible spectra of these phosphors.

Fig. 4.9 represents the Tauc plots for **(A)** 4 mol% Eu doped and **(B-D)** for 5 mol% Li, 3 mol% Na and 2 mol% K co-doped Gd_2O_3 phosphors, respectively, and the insets represent the actual UV-Vis spectra for the respective samples. UV-Vis spectra of doped and co-doped Gd_2O_3 samples exhibit strong absorption in the UV region. In the case of alkali metal ions co-doped samples; there is a redshift of the absorption edge as compared to the Gd_2O_3:4mol%Eu sample. The red shifting of the absorption edge in the case of alkali metal ions co-doped samples corresponds to the energy levels caused by interstitial defects.

The bandgap of Gd_2O_3:4mol%Eu is determined to be 5.11 eV. A decrease in the bandgap with alkali metal co-doping in Gd_2O_3:4mol%Eu is observed. The bandgaps of Li^+, Na^+, and K^+ co-doped Gd_2O_3:4mol%Eu are determined to be 4.95, 4.94, and 4.78 eV,

respectively. The variation in E_g values can be related to the degree of structural order-disorder variation in the lattice, which changes the intermediate energy level within the bandgap. The ionic radius of Li^+ ions is smaller than the Gd^{3+} ions, so this results in the shrinkage of the host lattice. However, ionic radii of Na^+ and K^+ ions are larger than the Gd^{3+} ions, which leads to the expansion of the crystal lattice. The variation in the size of these cations results in the variation in structure density. In addition to this, alkali metal and Gd^{3+} ions possess different valency [3]. The introduction of alkali metal ions (Li^+, Na^+, K^+) in the host lattice gives rise to the number of oxygen vacancies. This changes the energy band structure and enhances the deformation degree of O 2p orbits with the superposition of the electronic wave functions. Thus, the forbidden band gets narrowed and red shifting of absorption edge is observed [3]. The increase in the oxygen vacancies also leads to change in density of states and electronic structure of the host lattice [22]. The generation of the oxygen vacancies gives rise to the redshift of the absorbance edge and thus bandgap decreases in the case of alkali metal co-doped samples. Li *et al.* [23] observed the same red shifting of absorption edge with the incorporation of Li^+ ions in the (Y, Gd)BO_3:Eu host lattice. In the present case, oxygen vacancies play a significant role in varying the bandgap of alkali metal co-doped Gd_2O_3: Eu phosphors.

4.8 Photoluminescence Studies

Fig. 4.10 represents the excitation spectra of Eu doped and alkali metal ions co-doped Gd_2O_3 samples recorded in the region 200-400 nm under 612 nm excitation wavelength. A broadband between 200-280 nm is assigned to the Eu-O CT band (ligand to metal charge transfer transition) [24]. The position of this band depends on the Eu-O bond length, ligand charge, bond volume polarization, and coordination of the europium ions. There are small peaks present beyond 280 nm, which are present due to f transitions of europium ions. A small shifting of this band is observed in case of co-doped samples. To study the shifting of Eu-O CT band, Jorgensen's formula of charge transfer was employed to determine the ligand ion's optical electronegativity, given below:

$$\Delta(\text{Eu-O}) = [\chi(O^{2-}) - \chi(Eu^{3+})] \times 3\times10^4 \text{ cm}^{-1} \quad (4.5)$$

where, χ represents the optical electronegativities of ions, and Δ (Eu-O) is the position of Eu-O CT band [24]. The variation in CT band position suggests increase in the covalency or decrease of the ionicity of Eu-O bond. The emission spectra were recorded under 250 nm excitation in the range from 550 to 800 nm.

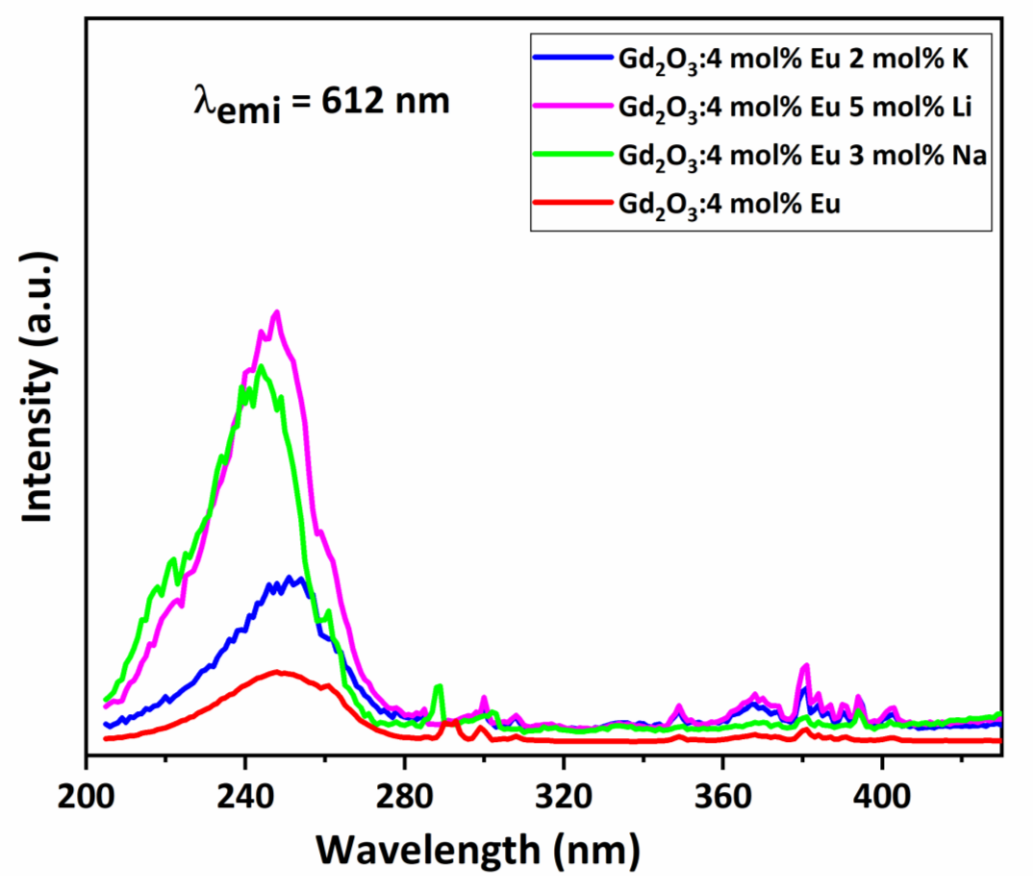

Figure 4.10: Excitation spectra of 4 mol% Eu doped and alkali metal ions co-doped (5 mol% Li, 3 mol% Na and 2 mol% K) Gd_2O_3 phosphors.

The emission spectra of Eu^{3+} doped (1 to 5 mol%) Gd_2O_3 phosphors are shown in **Fig. 4.11**. The maximum emission intensity peak is observed at 612 nm. The other emission peaks are also observed at 592, 625, 650, and 705 nm [25–29]. The peak at 611 nm is a hypersensitive electric dipole transition, while weak intensity peak around 592 nm is insensitive magnetic dipole transition. There are two symmetry sites i.e., C_2 and S_6, in Gd_2O_3 lattice, which are present in the ratio 3:1. C_2 sites possess non-inversion symmetry, and S_6 sites possess inversion symmetry. The positions of these two different sites in the Gd_2O_3 lattice are shown in **Fig. 4.12**. When europium ions occupy S_6 site, transition corresponding to the 592 nm ($^5D_0 \rightarrow {}^7F_1$) dominates.

When europium ions occupy C_2 site, transition at 612 nm ($^5D_0 \rightarrow {}^7F_2$) dominates [30]. Since $^5D_0 \rightarrow {}^7F_2$ transition is hypersensitive to the host matrix, while $^5D_0 \rightarrow {}^7F_1$ is not, the ratio of the integrated intensity of these transitions i.e., $\left(\frac{\int I(^5D_0 - {}^7F_2)}{\int I(^5D_0 - {}^7F_1)}\right)$, known as asymmetry ratio (A_{sym}), can be used to probe the non-symmetric environment of europium ions in Gd_2O_3 matrix. The value of the asymmetry ratio greater than 1 is considered as a highly asymmetric environment around the metal ion [31]**.** The values of the asymmetry ratio for the doped and co-

doped samples have been summarized in **Table 4.3 (b)**. The value of the asymmetry ratio is greater than 1 for all the doped and co-doped samples, representing the highly non-symmetric environment of the europium ions.

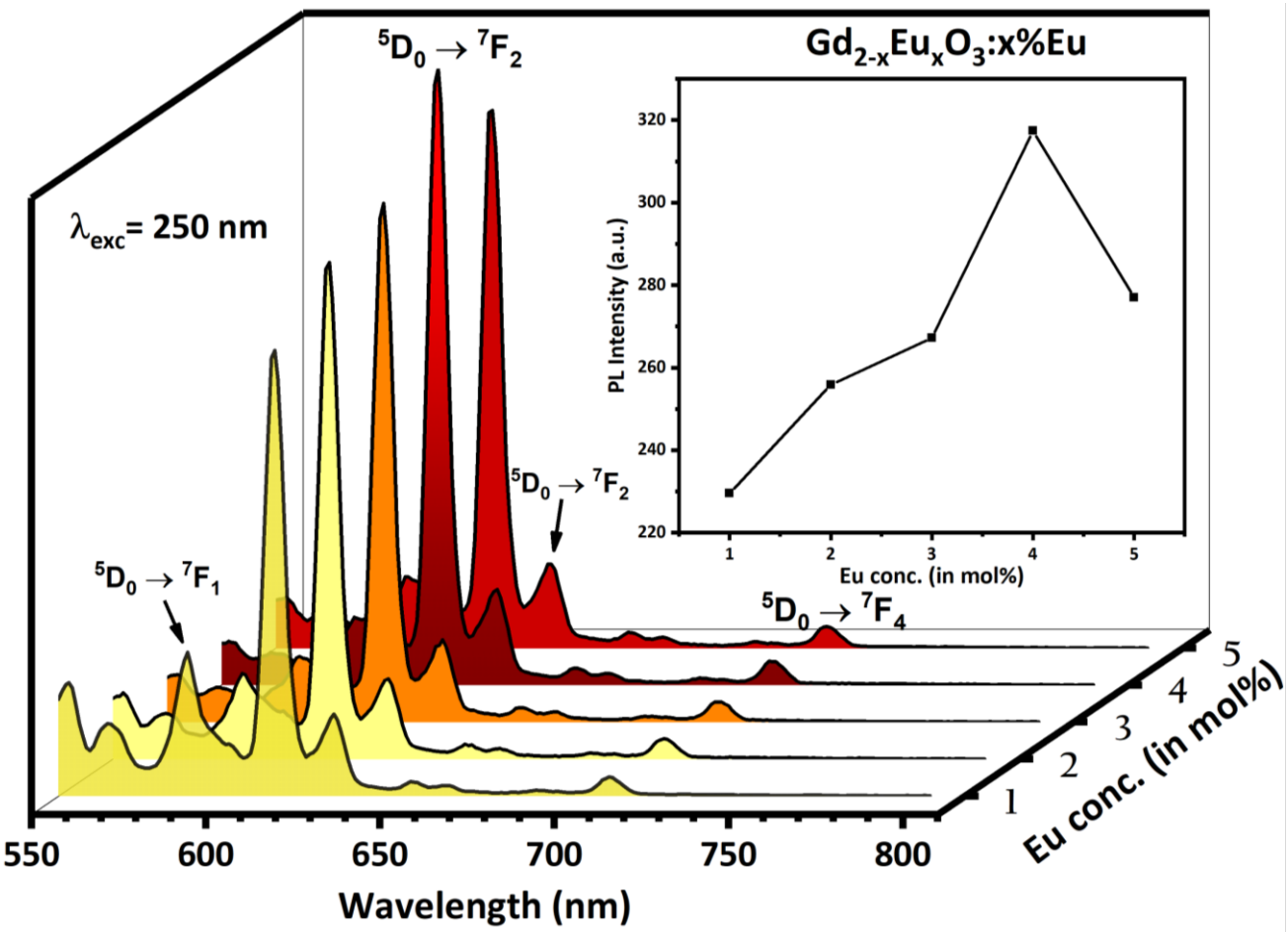

Figure 4.11: Emission spectra of Gd_2O_3 with the variation of Eu ions (1 to 5 mol%).

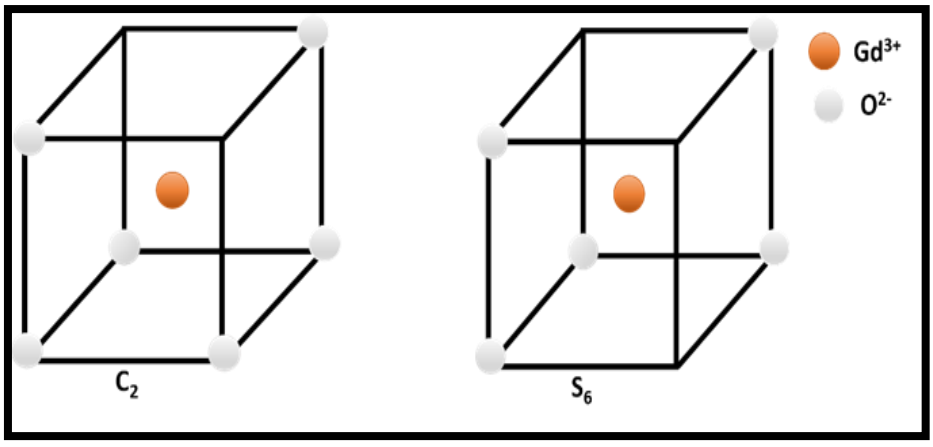

Figure 4.12: Position of C_2 and S_6 sites in cubic-Gd_2O_3 lattice.

It is observed that emission intensity increases with increasing europium ion concentration. The maximum PL intensity is observed for the 4 mol% Eu^{3+} ions beyond which

concentration quenching occurs. There are many reasons for the concentration quenching like non-radiative energy transfer among the europium ions. As distance between the europium ions decreases, it leads to the non-radiative energy transfer. The minimum distance (R_c), which is known as the critical distance, can be found by Blasse's equation [32]. According to Blasse equation:

$$R_c = 2\left[\frac{3V}{4\pi N X_c}\right]^{1/3} \quad (4.6)$$

where, V corresponds to cell volume, X_c is dopant ion concentration, and N represents the number of available sites for dopant ion in the host. For Gd_2O_3:4mol%Eu, N= 32, X_c= 0.04, V= 1251.42 $Å^3$. If the value of the $R_c \leq 5$ Å, then it will lead to the non-radiative transitions, and if it is greater than 5 Å, then multipole-multipole transitions are taken into account due to the concentration quenching mechanism. The value of R_c is determined to be 10.27 Å. It indicates that the cause of the concentration quenching in the host matrix is multipolar transitions, such as dipole-dipole (d-d), quadrupole-quadrupole (q-q), dipole-quadrupole transition (q-d), etc. The type of transition can be found using Dexter's theory. The multipolar interaction can be calculated by the following equation [33]:

$$\frac{I}{\chi} = K\left[1 + L(\chi)^{Q/3}\right]^{-1} \quad (4.7)$$

where, χ corresponds to the activator concentration, K and L are the constants for a given host, Q is a constant and its value 6, 8 and 10 corresponds to d-d, q-d, and q-q transition, respectively. The value of Q is determined from the slope (Q/3) of the graph plotted between log(I/C) versus log(C). A graph is plotted between log(I/C) versus log(C), and slope of the graph is determined to be -1.79 **(Fig. 4.13)**.

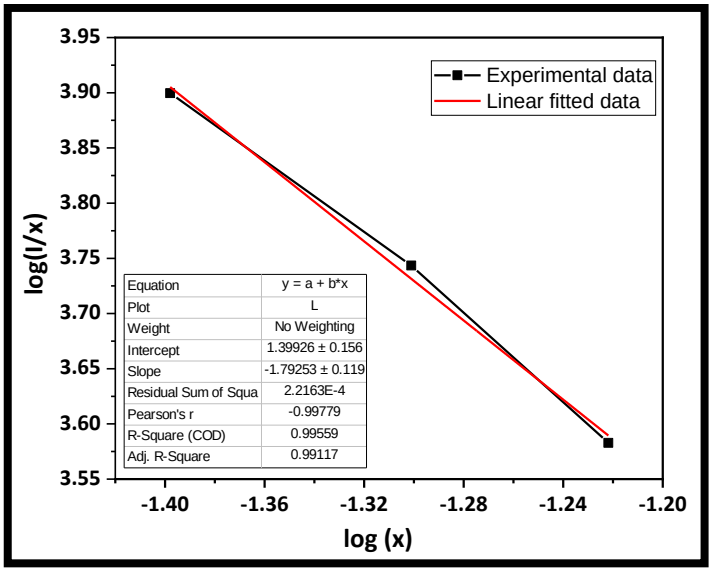

Figure 4.13: Plot of log(I/x) versus log(x) for Gd_2O_3:Eu phosphor.

Thus, value of Q is calculated to be 5.37, which represents the theoretical value required for the d-d transition. Hence, the quenching mechanism for the given host is mainly due to d-d transition. The optimum concentration of europium ions in Gd_2O_3 lattice is 4 mol%. The effect of pH and calcination temperature on the luminescent behavior of Gd_2O_3:4mol% is also investigated. The emission spectra of Gd_2O_3:4mol% as a function of pH and calcination temperature is shown in **Fig. 4.14**. PL intensity increases with increase in the calcination temperature and is found maximum at 800 ℃. Further, decrease in PL intensity above this temperature is observed due to increase in the non-radiative transitions. PL intensity is found to be maximum at pH 10 compared to the sample synthesized at pH 8. The decrease in PL intensity at low pH is attributed to the non-uniform morphology, irregular shapes, and agglomeration observed in the samples. The maximum PL is obtained for the sample, which is synthesized at pH 10, calcined at 800 ℃, and having 4 mol% europium ions in the host lattice. This is the optimized sample and used in further study to see the effect of alkali and alkaline-earth metal co-doping in the Gd_2O_3:Eu host lattice.

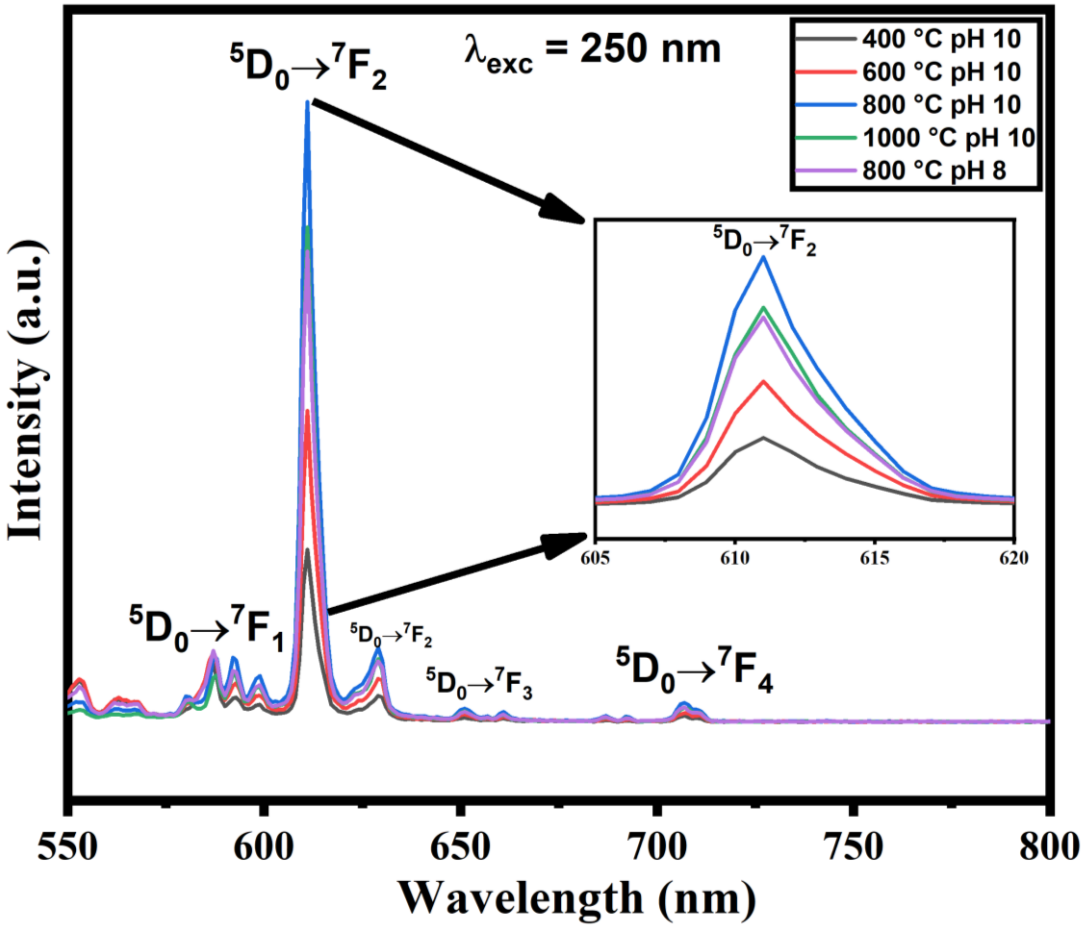

Figure 4.14: PL emission spectra of Gd_2O_3:4mol%Eu phosphors synthesized at different pH and temperature.

Further, the effect of alkali metal co-doping in Gd_2O_3:4mol%Eu is studied. **Fig. 4.15 (A)** represents the PL emission spectra of the Li^+ ion (1 to 6 mol%) co-doped Gd_2O_3:4mol%Eu. The concentration quenching occurs for 5 mol% of Li^+ ions. **Fig. 4.15 (B)** represents the PL emission spectra of Na^+ co-doped Gd_2O_3: Eu phosphors. Na^+ ions concentration is varied from 1 to 4 mol%, and the optimum concentration is found to be 3 mol%.

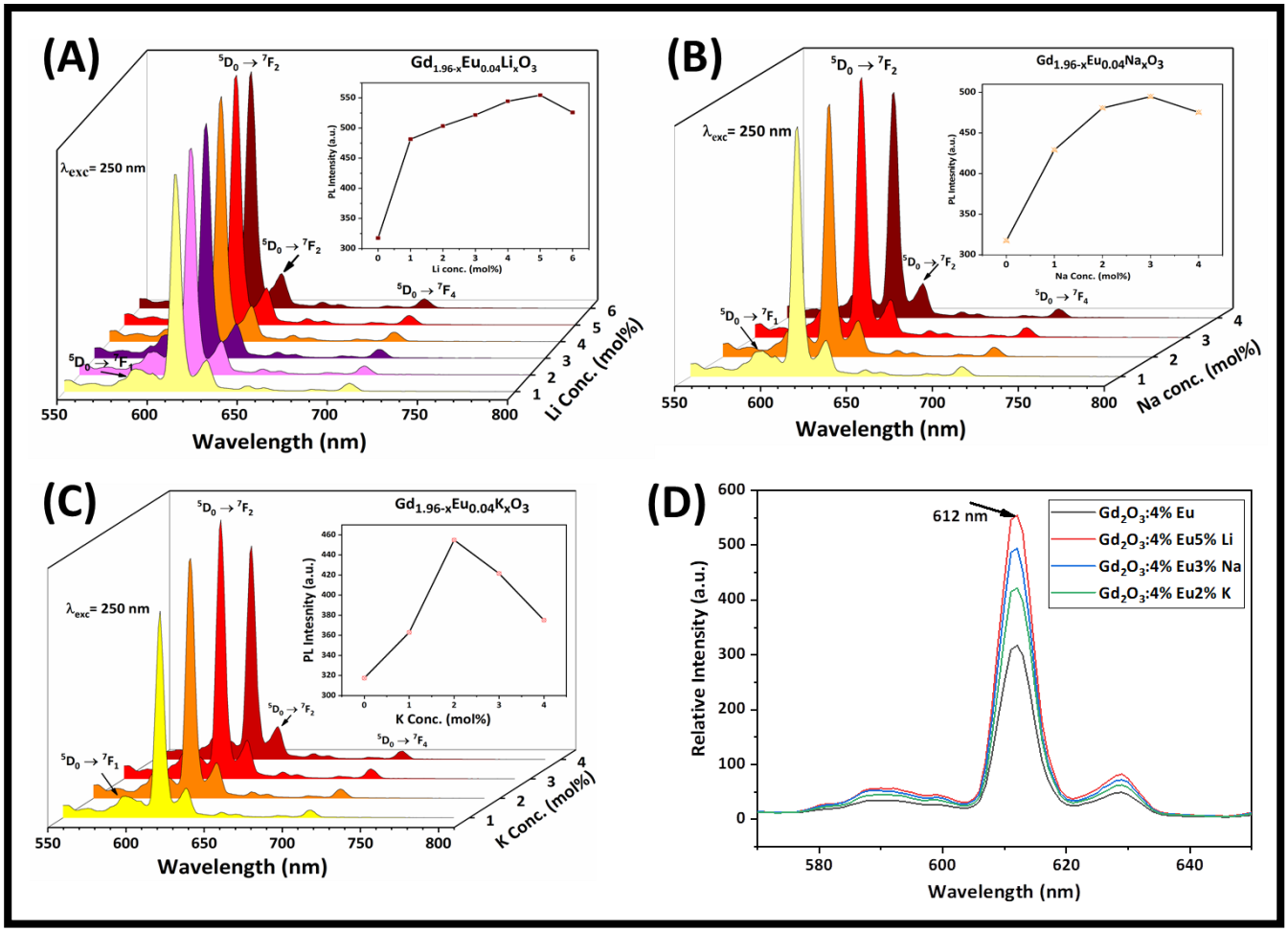

Figure 4.15: PL emission spectra of (A) Li^+ co-doped (1 to 6 mol%), (B) Na^+ co-doped (1 to 4 mol%), (C) K^+ co-doped (1 to 4 mol%) Gd_2O_3:4mol%Eu phosphors and (D) Relative emission spectra of Eu doped and alkali metal ions co-doped Gd_2O_3 phosphors.

Fig. 4.15 (C) represents the PL emission spectra of K^+ ions co-doped Gd_2O_3:4mol%Eu phosphors, and the K^+ ions concentration is varied from 1 to 4 mol% yielding optimum concentration at 2 mol%. It is observed that emission spectra of the Gd_2O_3:4mol%Eu and alkali metal co-doped Gd_2O_3:4mol%Eu phosphors have the same characteristics of peak shape and position. However, with the incorporation of alkali metal ions, emission intensity os increased as compared to Gd_2O_3:4mol%Eu sample. **Fig. 4.15 (D)** represents the PL emission spectra of 5 mol% Li, 3 mol% Na and 2 mol% K co-doped Gd_2O_3:4mol%Eu samples. The emission

intensities of the Li^+, Na^+, and K^+ co-doped samples are increased by 1.75, 1.56, and 1.32 times of Gd_2O_3:4mol%Eu, respectively. The partial energy level diagram illustrating the excitation and emission transitions in Gd_2O_3:Eu matrix is represented in **Fig. 4.16.**

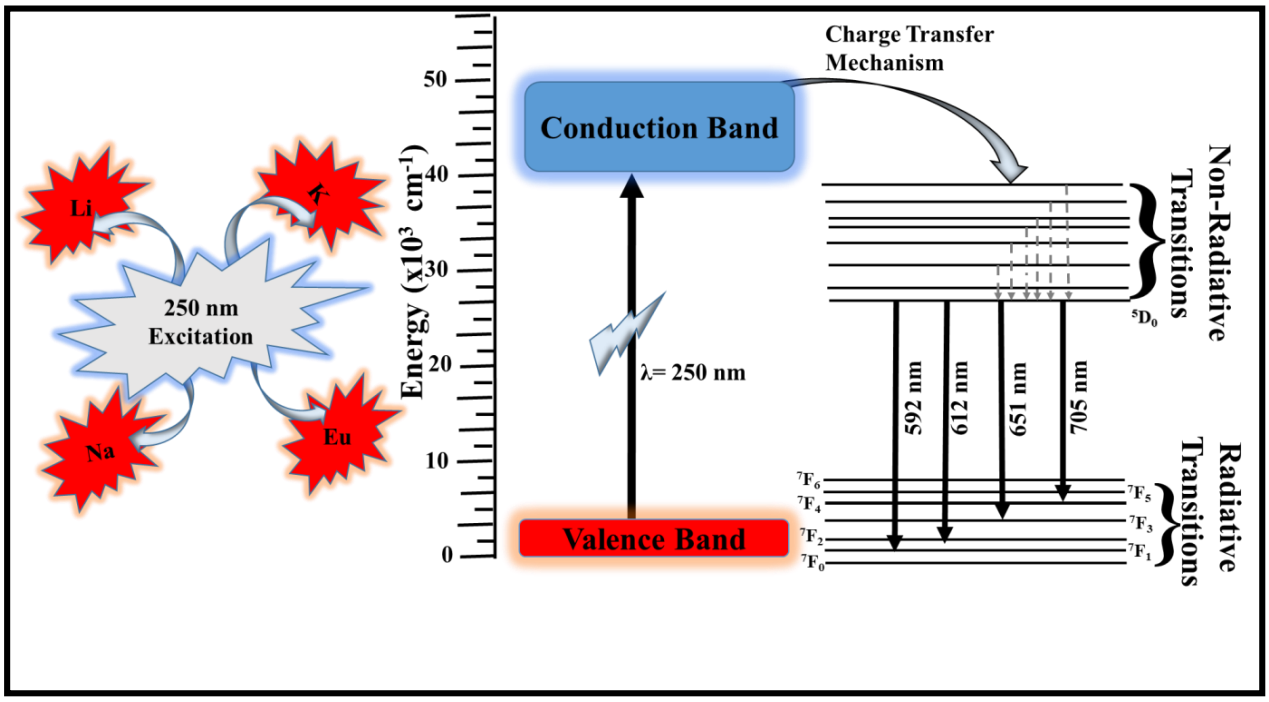

Figure 4.16: Energy level diagram of Gd_2O_3:Eu under excitation at 250 nm.

The enhancement in the emission intensity with alkali metal ions (AM) incorporation can be attributed to several reasons. The ionic radii of alkali metal ions are different from Gd^{3+} ions. The substitution of the AM^+ ions with Gd^{3+} ions gives rise to the change in the crystal lattice parameters around the activator ions, which influences the spin orbit-coupling and crystal field of europium ions. The ionic radius of the Li^+ ions is close to the Gd^{3+} ions, so they can be easily substituted on the Gd^{3+} site. But, ionic radii of Na^+ and K^+ ions are larger than the Gd^{3+} ions. Thus, Li^+ ions are expected to cause less distortion in the crystal structure as compared to the Na^+ and K^+ ions. Moreover, alkali metal ions occupy Gd^{3+} sites in Gd_2O_3 and contribute in the creation of oxygen vacancies. The oxygen vacancies act as sensitizers for the luminescent enhancement for the energy transfer due to the strong mixing of the charge transfer states. This mixing of states results increase in the oscillator strength, which helps in luminescent enhancement [34]. In addition, the incorporation of alkali metal ions in the host lattice may change the coordination conditions**,** which results variation in Eu-O bond length [35]. The distortion in the Eu-O bond and local symmetry around europium ions leads to increase in the transition probabilities of intra-4f transitions of europium ions, which contribute to the PL enhancement in the alkali metal co-doped Gd_2O_3:Eu phosphors.

One more possible reason for the enhancement in the luminescent intensity could be the creation of bounded electron-hole (*e-h*) pairs with the incorporation of alkali metal ions in Gd_2O_3:Eu [36]. In Gd_2O_3:Eu, alkali metal ions substitute Gd^{3+}, and create point defects such as oxygen vacancies to compensate for the extra positive charge of Gd^{3+}, which can be represented as:

$$M_2O \xrightarrow{Gd_2O_3} 2M''Gd + 2V\ddot{o} + O_o^x \qquad (4.8)$$

The bounded e-h pair in the crystal gives rise to strong excitation band of the host under UV excitation. Since ionic radii and the valency of the alkali metal ions are different from Gd^{3+}, the incorporation of alkali metal ions in Gd_2O_3:Eu leads to the formation of *e-h* pair. The similar phenomenon was observed in alkali metal co-doped (Y, Gd)BO_3:Eu phosphors [23]. The increase in the alkali metal ion concentration leads to increase in oxygen vacancies. The increase in the oxygen vacancies beyond a certain limit results in the concentration quenching. This occurs because of the energy transfer to the quenching sites.

The perception of emission color and quality of light sources of doped and co-doped samples is analyzed by determining the CIE coordinates and correlated color temperature (CCT) values. **Fig. 4.17** represents the CIE chromaticity diagram of the europium doped and alkali metal co-doped Gd_2O_3 phosphors.

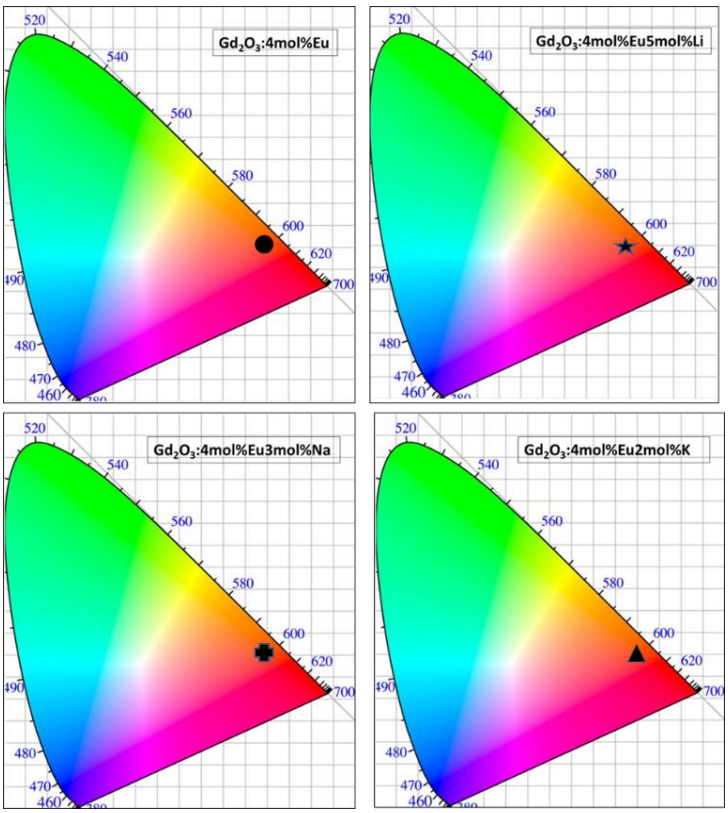

Figure 4.17: CIE coordinates of 4 mol% Eu doped and alkali metal ions co-doped (5 mol% Li, 3mol% Na and 2 mol% K) Gd_2O_3 phosphors.

CIE values of the synthesized phosphors lie in the red region. According to National Television Standard Committee (NTSC), ideal value of red color coordinates is (0.67, 0.33). With co-doping of alkali metal ions, the coordinates shift towards rge ideal red color.

CCT values are calculated by McCamy's empirical formula [37]. According to this:

$$\mathbf{CCT} = -473\ n^3 + 3601\ n^2 - 6861\ n + 5514.31 \quad (4.9)$$

where, $n= (x-x_e)/(y-y_e)$ and (x_e, y_e) represent the coordinates of chromaticity epicenter located at $x_e= 0.3320$ and $y_e= 0.1858$. The CIE and CCT values for doped and co-doped Gd_2O_3 phosphors are enlisted in **Table 4.2**. The calculated CCT values of the phosphors are in the range 1081-1280 K. In general, CCT values less than 5000 K indicate the warm light and are suitable for the household applications [38]. This illustrates that synthesized samples are suitable for the luminescent devices.

Table 4.2: CIE and CCT values of synthesized phosphors.

Concentration (in mol%)	**Chromaticity coordinates**		**CCT values (K)**
	x	**y**	
	$Gd_{2-x}Eu_xO_3$		
1.0	0.6192	0.3802	1280
2.0	0.6324	0.3672	1169
3.0	0.6377	0.3619	1126
4.0	0.6417	0.3572	1092
5.0	0.6375	0.3622	1128
	$Gd_{1.96-x}Eu_{0.04}Li_xO_3$		
1.0	0.646	0.3536	1061
2.0	0.6473	0.3522	1051
3.0	0.6475	0.3520	1049
4.0	0.6478	0.3518	1047
5.0	0.6484	0.3519	1046
6.0	0.6477	0.3512	1045
	$Gd_{1.96-x}Eu_{0.04}Na_xO_3$		
1.0	0.6458	0.3538	1063
2.0	0.6456	0.3540	1064
3.0	0.6461	0.3535	1060
4.0	0.6457	0.3539	1064
	$Gd_{1.96-x}Eu_{0.04}K_xO_3$		
1.0	0.6428	0.3568	1086
2.0	0.6454	0.3542	1066
3.0	0.6459	0.3569	1075
4.0	0.6435	0.3561	1081

Judd-Ofelt analysis is carried out to understand the site symmetry and luminescence behavior of synthesized phosphors [39]. Judd Ofelt parameters (Ω_t = (t= 2, 4, 6) and intensity are calculated from the emission spectra, and are given in **Table 4.3 (a)**.

Table 4.3 (a): Spectral parameters of $Gd_{2-x}O_3$:x%Eu doped and alkali metal co-doped phosphors.

Judd- Ofelt Intensity Parameters					
Concentration (in mol%)	**Ω_2 (10^{-20} cm^2)**	**Ω_4 (10^{-20} cm^2)**	**A_{0-1} (sec^{-1})**	**A_{0-2} (sec^{-1})**	**A_{0-4} (sec^{-1})**
$Gd_{2-x}Eu_xO_3$					
1.0	4.34	0.206	50	236.9	7.65
2.0	4.49	0.207	50	245.7	8.18
3.0	4.21	0.198	50	229.9	7.35
4.0	4.44	0.214	50	242.8	7.93
5.0	3.62	0.171	50	198.0	6.33
$Gd_{1.96-x}Eu_{0.04}Li_xO_3$					
1.0	3.73	0.166	50	204.0	6.16
2.0	4.28	0.196	50	234.0	7.32
3.0	4.01	0.197	50	219.3	7.32
4.0	3.26	0.159	50	178.3	5.90
5.0	3.44	0.169	50	188.4	6.26
6.0	4.06	0.192	50	222.1	7.13
$Gd_{1.96-x}Eu_{0.04}Na_xO_3$					
1.0	3.89	0.197	50	212.9	7.32
2.0	3.51	0.169	50	192.3	6.28
3.0	3.57	0.170	50	195.6	6.31
4.0	4.14	0.170	50	226.3	7.10
$Gd_{1.96-x}Eu_{0.04}K_xO_3$					
1.0	4.02	0.186	50	219.6	6.89
2.0	4.57	0.211	50	249.2	7.81
3.0	3.70	0.188	50	203.0	6.97
4.0	4.08	0.185	50	222.3	6.84

$^5D_0 \rightarrow {}^7F_1$ (magnetic dipole) transition is taken as the reference. In our case, we have calculated Ω_2, Ω_4 but not Ω_6 because $^5D_0 \rightarrow {}^7F_6$ transition was not present. These intensity parameters are determined by the scheme described by Kodaira *et al.* [40]. The radiative rates ($A_{0-2,4}$ and A_{0-1}) and integrated emission intensities ($I_{0-2,4}$ and I_{0-1}) are associated with the relation:

$$\frac{A_{0-2,4}}{A_{0-1}} = \frac{I_{0-2,4}}{I_{0-1}} \frac{h\nu_{0-1}}{h\nu_{0-2,4}} \tag{4.10}$$

where, I_{0-j} is the integrated area, and ν_{0-j} represent the energy barycenter corresponding to a particular transition. The radiative rate of magnetic dipole transition was taken as 50 sec^{-1} [9]. The radiative rates ($A_{0-2,4}$) as a function of J-O intensity parameters can be expressed as follows [41]:

$$A_{0-J} = \frac{64\,\pi^4 (\nu_{0-2,4})^3 e^2}{3hc^3} \frac{1}{4\pi\varepsilon_0} \chi \sum_j (j= 2,\ 4)[\Omega_j \langle {}^5D_0|U(J)|{}^7F_{2,4}\rangle^2] \tag{4.11}$$

$<^5D_0|U(J)|^7F_{2,4}>^2$ are the squared reduced matrix elements, their values are: $<^5D_0|U(J)|^7F_2>^2 = 0.0032$ and $<^5D_0|U(J)|^7F_4>^2 = 0.0023$. The other radiative parameters are also calculated using Judd-Ofelt parameters and are given in **Table 4.3 (b).**

Table 4.3 (b): Spectral parameters of $Gd_{2-x}O_3$:x%Eu doped and alkali metal co-doped phosphors.

Concentration (in mol%)	A_T (Ψ_j) (s^{-1})	τ_{rad} (ms)	Branching ratio (in %)			Asymmetry ratio	Stimulated emission cross-section (cm^2)		
			β_{0-1}	β_{0-2}	β_{0-4}		σ_{0-1} (10^{-22})	σ_{0-2} (10^{-21})	σ_{0-4} (10^{-22})
$Gd_{2-x}Eu_xO_3$									
1.0	294.6	3.39	16.9	80.43	2.60	3.88	3.39	2.03	1.04
2.0	303.9	3.29	16.45	80.85	2.69	4.07	2.13	2.10	1.09
3.0	287.2	3.48	17.41	80.03	2.56	3.77	1.33	1.96	0.99
4.0	300.7	3.33	16.63	80.74	2.64	3.96	1.26	2.08	0.10
5.0	254.4	3.93	19.66	77.85	2.49	3.30	1.28	1.71	0.86
$Gd_{1.96-x}Eu_{0.04}Li_xO_3$									
1.0	260.2	3.84	19.22	78.41	2.37	3.42	1.21	1.01	0.84
2.0	291.3	3.43	17.16	80.32	2.51	3.90	1.27	2.03	0.10
3.0	276.6	3.62	18.08	79.28	2.65	3.70	1.23	1.92	0.98
4.0	234.2	4.27	21.35	76.14	2.52	3.03	1.14	1.46	0.80
5.0	244.7	4.09	20.43	77.01	2.56	3.20	1.17	1.66	0.84
6.0	279.3	3.58	17.90	79.54	2.55	3.75	1.24	1.82	0.99
$Gd_{1.96-x}Eu_{0.04}Na_xO_3$									
1.0	270.3	3.70	18.50	80.32	2.71	3.60	1.21	1.87	0.97
2.0	248.6	4.02	20.12	79.28	2.53	3.30	1.21	1.71	0.83
3.0	251.9	3.96	19.85	76.14	2.50	3.35	1.21	1.74	0.87
4.0	283.4	3.52	17.64	77.01	2.51	3.75	1.25	1.94	0.98
$Gd_{1.96-x}Eu_{0.04}K_xO_3$									
1.0	276.5	3.62	18.08	79.43	2.49	3.62	1.23	1.89	0.94
2.0	307.0	3.25	16.28	81.17	2.54	4.08	1.25	2.12	1.06
3.0	260.0	3.85	19.23	78.08	2.68	3.63	1.19	1.76	0.96
4.0	279.1	3.58	17.91	79.64	2.45	3.52	1.23	1.73	0.93

The total radiative transition probability, radiative lifetime ($\tau_{rad}(\psi_J)$), branching ratio ($\beta(\psi_j)$) and stimulated emission cross-section σ (λ_p) are estimated using following expressions:

$$\mathbf{A_T(\Psi_j)} = \Sigma A_{J\text{-}J'} \tag{4.12}$$

$$\boldsymbol{\tau_{rad}(\psi_J)} = \frac{1}{A_T(\psi_J)} \tag{4.13}$$

$$\boldsymbol{\beta(\psi_J)} = \frac{A(\psi_J, \psi'_{J'})}{A_J(\psi_J)} \tag{4.14}$$

$$\boldsymbol{\sigma(\lambda_p)\ (J \rightarrow J')} = \frac{\lambda_P^4}{8\, c\, n^2\, \Delta\lambda_{eff}} A_{rad}\ (J \rightarrow J') \tag{4.15}$$

where, λ_p is the wavelength of the peak corresponding to the particular transition and $\Delta\lambda_{eff}$ (effective linewidth) is calculated by dividing the total area under emission band by its maximum height.

It can be observed from **Table 4.3 (a-b)** that the value of Ω_2 is found to be more than Ω_4. Ω_2 is highly sensitive to the ligand environment and represents the asymmetry of the local environment activator ions. With alkali metal ion co-doping, the value of Ω_2 decreases, indicating increase in the symmetry. The decrease in Ω_4 values is also observed. It demonstrates that with the incorporation of the alkali metal ions, efficiency of the $^5D_0 \rightarrow {}^7F_2$ transition increases. β values and stimulated cross-section values are also higher for the $^5D_0 \rightarrow {}^7F_2$ transition than the other transitions. Moreover, branching ratio of this transition in the synthesized phosphors is greater than 0.50, which makes them suitable for solid-state lighting applications.

References

1 S. Chaudhary, S. Kumar, A. Umar, J. Singh, M. Rawat and S. K. Mehta, *Sensors Actuators B. Chem.*, 2017, **243**, 579–588.

2 J. Chen, Y. Shi and J. Shi, *J. Mater. Res.*, 2004, **19**, 3586–3591.

3 R. G. A. Kumar, S. Hata and K. G. Gopchandran, *Ceram. Int.*, 2013, **39**, 9125–9136.

4 N. Dhananjaya, H. Nagabhushana, B. M. Nagabhushana, B. Rudraswamy, C. Shivakumara, K. P. Ramesh and R. P. S. Chakradhar, *Phys. B Phys. Condens. Matter*, 2011, **406**, 1645–1652.

5 A. Jain and G. A. Hirata, *Ceram. intenational*, 2016, **42**, 6428–6435.

6 J. Li, Q. Zhu, X. Li, X. Sun and Y. Sakka, *Acta Mater.*, 2011, **59**, 3688–3696.

7 A. A. Ansari, N. Ahmad and J. P. Labis, *J. Photochem. Photobiol. A Chem.*, 2019, **371**, 10–16.

8 N. Dhananjaya, H. Nagabhushana, B. M. Nagabhushana, B. Rudraswamy, C. Shivakumara and R. P. S. Chakradhar, *J. Alloys Compd.*, 2011, **509**, 2368–2374.

9 R. G. A. Kumar, S. Hata, K. Ikeda and K. G. Gopchandran, *RSC Adv.*, 2016, **6**, 67295–67307.

10 N. Dhananjaya, H. Nagabhushana, B. M. Nagabhushana, B. Rudraswamy, C. Shivakumara, K. Narahari and R. P. S. Chakradhar, *Spectrochim. Acta - Part A Mol. Biomol. Spectrosc.*, 2012, **86**, 8–14.

11 Z. Wang, P. Wang, J. Zhong, H. Liang and J. Wang, *J. Lumin.*, 2014, **152**, 172–175.

12 Y. Iwako, Y. Akimoto, M. Omiya, T. Ueda and T. Yokomori, *J. Lumin.*, 2010, **130**, 1470–1474.

13 S. Majeed and S. A. Shivashankar, *J. Mater. Chem. C*, 2014, **2**, 2965–2974.

14 T. Thongtem, A. Phuruangrat, J. Ham, S. Lee and S. Thongtem, *CrystEngComm*, 2010, **12**, 2962–2966.

15 G. Kaur, P. Sharma, R. Priya and O. P. Pandey, *J. Alloys Compd.*, 2020, **822**, 153450.

16 R. Priya and O. P. Pandey, *Vacuum*, 2018, **156**, 283–290.

17 R. A. Mir and O. P. Pandey, *Chem. Eng. J.*, 2018, **348**, 1037–1048.

18 G. Boopathi, S. Gokul Raj, G. Ramesh Kumar, R. Mohan and S. Mohan, *Indian J. Phys.*, 2018, **92**, 715–724.

19 J. Yang, C. Li, Z. Cheng, X. Zhang, Z. Quan, C. Zhang and J. Lin, *J. Phys. Chem. C*, 2007, **111**, 18148–18154.

20 M. K. Devaraju, S. Yin and T. Sato, *Cryst. Growth Des.*, 2009, **9**, 2944–2949.

21 J. Tauc, R. Grigobovici and A. Vancu, *Phys. Stat. Sol.*, 1966, **15**, 627–637.

22 Q. Ma, Y. Zhou, A. Zhang, M. Lu, G. Zhou and C. Li, 2009, **11**, 1124–1130.

23 J. Li, Y. Wang and B. Liu, *J. Lumin.*, 2010, **130**, 981–985.

24 R. G. A. Kumar, S. Hata, K. Ikeda and K. G. Gopchandran, *Ceram. Int. 41*, 2015, **41**, 6037–6050.

25 A. N. Meza-Rocha, A. Speghini, J. Franchini, R. Lozada-Morales and U. Caldiño, *J. Mater. Sci. Mater. Electron.*, 2017, **28**, 10564–10572.

26 K. Munirathnam, G. R. Dillip, B. D. P. Raju, S. W. Joo, S. J. Dhoble, B. M. Nagabhushana, R. Hari Krishna, K. P. Ramesh, S. Varadharaj Perumal and D. Prakashbabu, *Appl. Phys. A Mater. Sci. Process.*, 2015, **120**, 1615–1623.

27 M. Bettinelli, F. Piccinelli, A. Speghini, J. Ueda and S. Tanabe, *J. Lumin.*, 2012, **132**, 27–29.
28 T. Qin, G. Mountjoy, N. D. Afify, M. F. Reid, Y. Y. Yeung, A. Speghini and M. Bettinelli, *Phys. Rev. B - Condens. Matter Mater. Phys.*, 2011, **84**, 1–14.
29 S. Som, S. Dutta, V. Kumar, A. Pandey, V. Kumar, A. K. Kunti, J. Priya, S. K. Sharma, J. J. Terblans and H. C. Swart, *J. Alloys Compd.*, 2015, **622**, 1068–1073.
30 C. C. Lin, K. M. Lin and Y. Y. Li, *J. Lumin.*, 2007, **126**, 795–799.
31 D. Kumar and S. J. Manam, *Appl. Phys. A*, 2018, **124**, 261–276.
32 X. Huang, H. Guo and B. Li, *J. Alloys Compd.*, 2017, **720**, 29–38.
33 K. Mondal, P. Kumari and J. Manam, *Curr. Appl. Phys.*, 2016, **16**, 707–719.
34 J. H. Jeong, J. S. Bae, S. Yi and J. Park, *J. Phys. Condens. Matter*, 2003, **567**, 567–574.
35 L. Li, L. Liu, W. Zi, H. Yu, S. Gan, G. Ji, H. Zou and X. Xu, *J. Lumin.*, 2013, **143**, 14–20.
36 W. Luo, J. Liao, R. Li and X. Chen, *Phys. Chem. Chem. Phys.*, 2010, **12**, 3276–3282.
37 C. S. McCamy, *Color Res. Appl.*, 1992, **17**, 142–144.
38 P. Kumari and J. Manam, *Spectrochim. Acta - Part A Mol. Biomol. Spectrosc.*, 2016, **152**, 109–118.
39 N. M. Maalej, A. Qurashi, A. A. Assadi, R. Maalej, M. N. Shaikh, M. Ilyas and M. A. Gondal, *Nanoscale Res. Lett.*, 2015, **10**, 215.
40 S. Som, A. K. Kunti, V. Kumar, V. Kumar, S. Dutta, M. Chowdhury, S. K. Sharma, J. J. Terblans and H. C. Swart, *J. Appl. Phys.*, 2014, **115**, 0–14.
41 L. Liu and X. Chen, *Nanotechnology*, 2007, **18**, 255704.

CHAPTER 5

RESULTS AND DISCUSSION II

Overview

This chapter discusses the effect of alkaline-earth metal (AEM = Mg^{2+}, Ca^{2+}, Sr^{2+}, Ba^{2+}) co-doping on different properties of Gd_2O_3:4mol%Eu phosphors. All the samples were excited under UV illumination and exhibited intense, sharp, and narrow emission peaks. The photometric parameters, such as CIE coordinates and CCT values are calculated. In order to further probe the luminescent properties and influence of the alkaline earth metals on the local environment of the europium ions in the host lattice, different radiative parameters are calculated using Judd Ofelt theory from emission spectra. The present chapter elucidates the effect of alkaline-earth metal co-doping in Gd_2O_3:Eu phosphor and their impact on altering the luminescent features.

5.1 Introduction

The luminescent intensity of the phosphors depends on various factors such as phase purity, grain size, defect-free surface, type of host, dopants, etc. In order to alter the luminescent intensity, various rare-earth and non-rare-earth co-dopants are being used these days. It has been observed that with the incorporation of these co-dopants, there is a substantial increase in the luminescent intensity. The co-doping with rare-earth elements is generally related to the energy transfer, up-conversion, and cross-section mechanism. However, a considerable increase in the luminescent intensity has also been found with the incorporation of the non-rare earth elements in the host matrix as co-dopants. For non-rare earth elements, alkali and alkaline-earth metals are generally used. In the recent reports, the luminescent intensity of various phosphors has been observed to improve several folds with the incorporation of alkali metals in the Y_2O_3:Eu, Gd_2O_3:Eu, $MgAl_2O_4$:Eu, $CaMg_2B_2O_5$:Sm, etc. [1–4]. In addition, alkaline-earth metals are also found to be responsible for the increased luminescent behavior in the Y_2O_3:Eu and YVO_4:Eu [5–7]. This is because of the difference in the size and valency of these co-doped elements and the host lattice elements. This leads to distortion in the crystal structure, which in turn alters the luminescent properties. As reported in the previous chapter that luminescent intensity decreases beyond 4 mol% of the Eu^{3+} ions in the Gd_2O_3 host lattice because of concentration quenching. However, with the incorporation of the alkali metal ions in the Gd_2O_3:4mol%Eu, PL intensity increased beyond the concentration quenching [8]. Motivating from the aforementioned facts, the present report deals with the structural, optical, and luminescent changes with the incorporation of the alkaline-earth metals (AEM) in the Gd_2O_3:4mol%Eu matrix. To the best of our knowledge, no one has reported the effect of the alkaline-earth metal co-doping in the Gd_2O_3:Eu matrix.

In the present chapter, alkaline-earth metal co-doped Gd_2O_3:Eu phosphors are synthesized via co-precipitation route. The structural, morphological, optical, and luminescent changes have been studied in detail. The concentration quenching mechanism and type of energy transfer has been explained on the basis of Blasse's theory. The photometric parameters, such as CIE coordinates and CCT values of the synthesized samples have been calculated. The change in the local environment of the Eu^{3+} ions with the incorporation of alkaline-earth metals in the Gd_2O_3 host matrix has been studied using standard Judd-Ofelt calculations from emission spectra. The obtained results are discussed below.

5.2 XRD Study

Fig. 5.1 represents the XRD patterns of alkaline-earth metals (AEM^{2+} = Mg^{2+}, Ca^{2+}, Sr^{2+}, Ba^{2+}) co-doped Gd_2O_3:4mol%Eu phosphors. The intensity of the peaks represents the crystalline nature of the synthesized phosphors. The observed XRD patterns are well-matched with the standard International center for diffraction data (ICDD) card number 03-065-3181 of Gd_2O_3 with cubic structure and $Ia\bar{3}$ (206) space group symmetry. No impure phase(s) corresponding to the initial precursor(s) are found, indicating that the synthesized phase is pure cubic phase of Gd_2O_3.

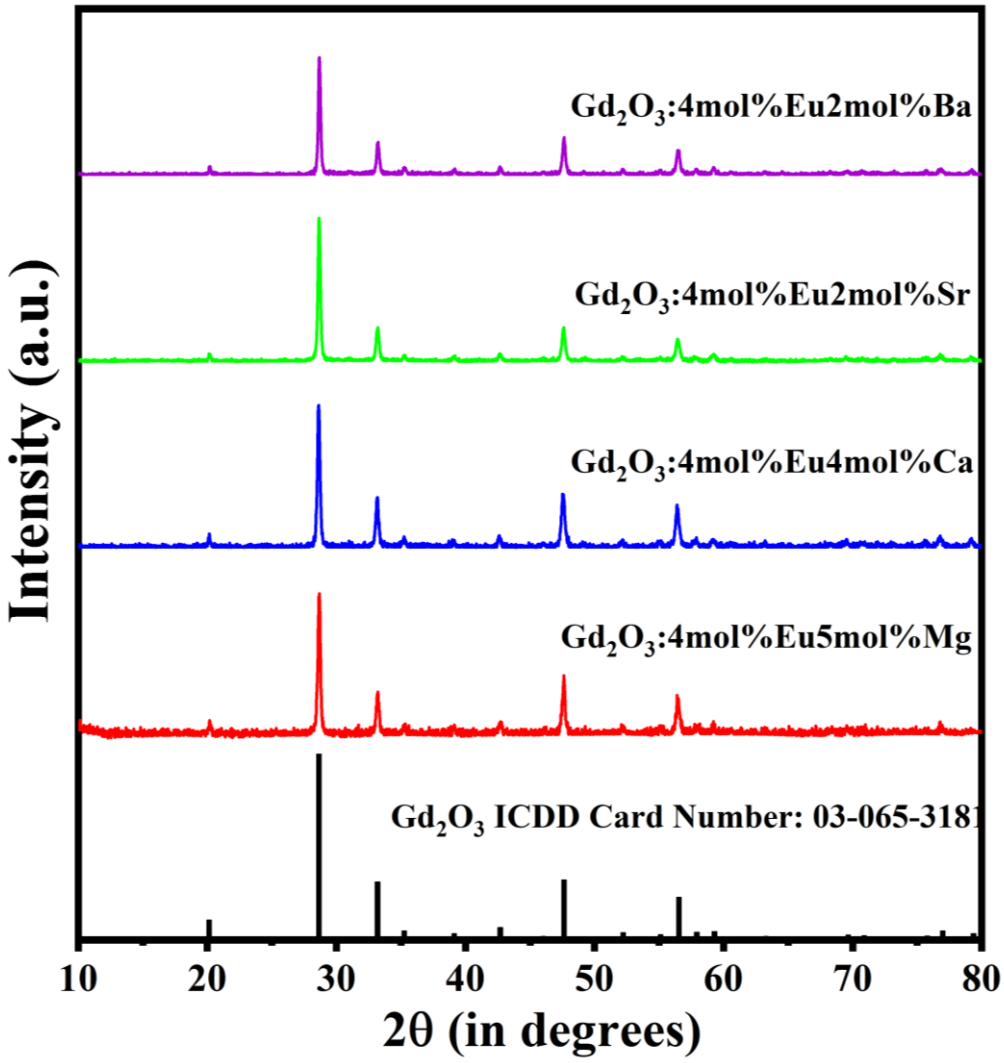

Figure 5.1: XRD patterns of alkaline-earth metal co-doped Gd_2O_3:Eu phosphors.

It has been observed that there is a small shifting in the XRD peaks with co-doping. This typical peak shifting nature of the highly intense (222) plane as observed for co-doped samples is shown in **Fig. 5.2**.

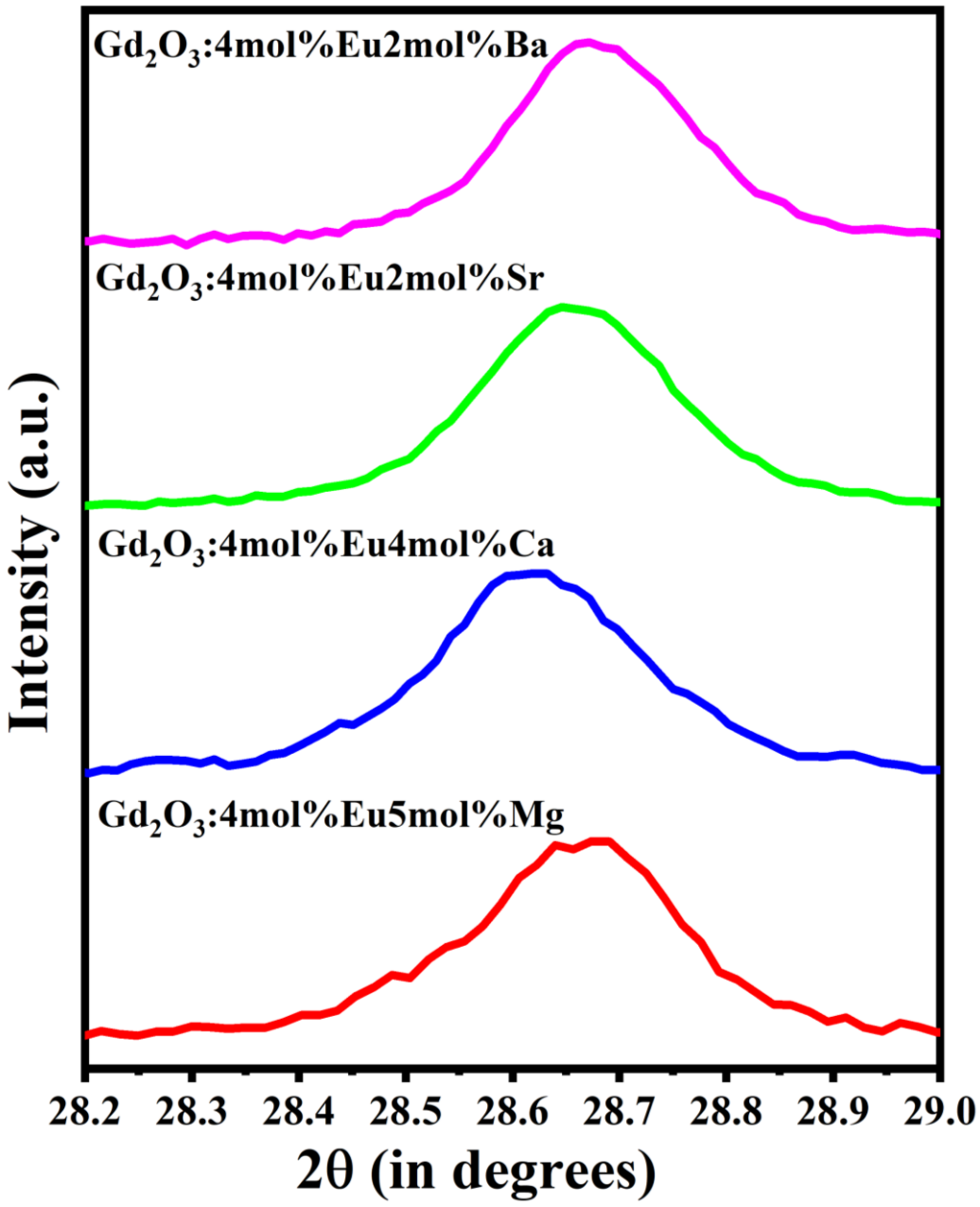

Figure 5.2: Peak shifting in the (222) plane of AEM co-doped Gd_2O_3:4mol%Eu phosphors.

The crystallite size (D) of the samples is determined using Debye-Scherrer formula [9]. The lattice parameters are calculated from the most intense peak w.r.t (222) plane using the following formulas:

$$2\ d \sin\theta = n\ \lambda \tag{5.1}$$

$$d = \frac{a}{\sqrt{h^2+k^2+l^2}} \tag{5.2}$$

Table 5.1 illustrates the calculated average crystallite size (D) and other structural parameters. The difference in the ionic radii of the AEM and host matrix has resulted in the

observed peak shifting. It can be depicted from the XRD results that with the incorporation of the alkaline-earth metal cations, there is an expansion in the crystal lattice. AEM co-doping did not alter the crystal structure, indicating that they have been completely incorporated in the host lattice.

Table 5.1: XRD crystal structure parameters and bandgap values of AEM co-doped Gd_2O_3:Eu phosphors.

Sample Name	Plane	Lattice parameter (Å)	Crystallite size (nm)	Bandgap (eV)
Gd_2O_3:4%Eu5%Mg	(222)	10.769	30-38	4.81
Gd_2O_3:4%Eu4%Ca	(222)	10.791	29-38	4.73
Gd_2O_3:4%Eu2%Sr	(222)	10.781	28-40	4.58
Gd_2O_3:4%Eu2%Ba	(222)	10.772	30-43	4.45

5.3 Morphological Features

Fig. 5.3 (a-d) represents the FESEM micrographs of the AEM co-doped Gd_2O_3:Eu phosphors.

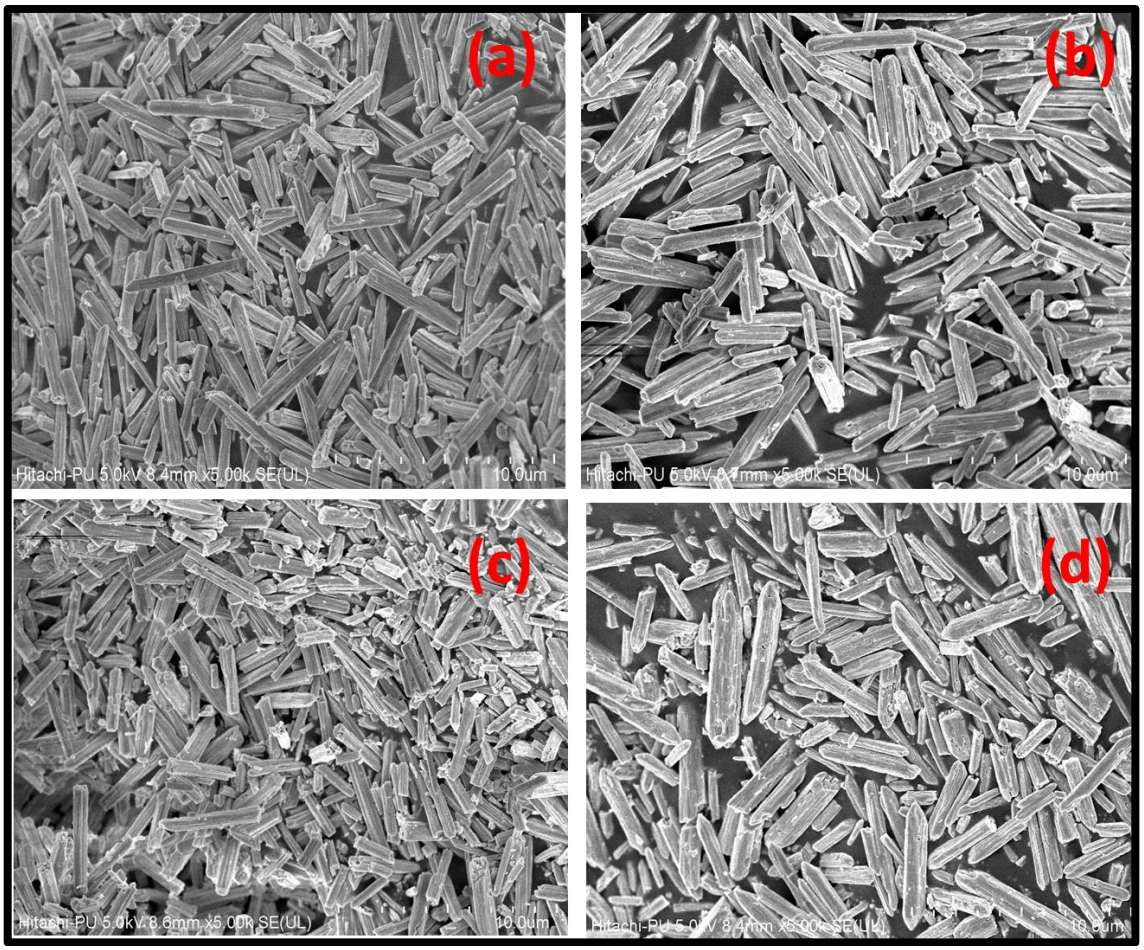

Figure 5.3: FESEM micrographs of AEM (a) Mg, (b) Ca, (c) Sr, and (d) Ba co-doped Gd_2O_3:4mol%Eu phosphors.

It can be seen from the microstructures **Fig. 5.3 (a-d)** that the morphology of the synthesized samples is rod like with variation in length and diameter. The formation of the nanorods can be explained on the basis of the self or induced scrolling mechanism [11,12]. It can be observed that different co-dopants (Mg^{2+}, Ca^{2+}, Sr^{2+}, Ba^{2+}) are introduced into the Gd_2O_3 matrix, but no change in the morphology is observed. So, different co-dopants have no effect on the directional growth mechanism of Gd_2O_3:Eu phosphors.

5.4 Fourier Transform Infrared (FTIR) Analysis

FTIR spectra of as-synthesized and calcined alkaline earth metal (Mg, Ca, Sr and Ba) co-doped Gd_2O_3:4mol%Eu phosphors are represented in **Fig. 5.4 (A - B)**.

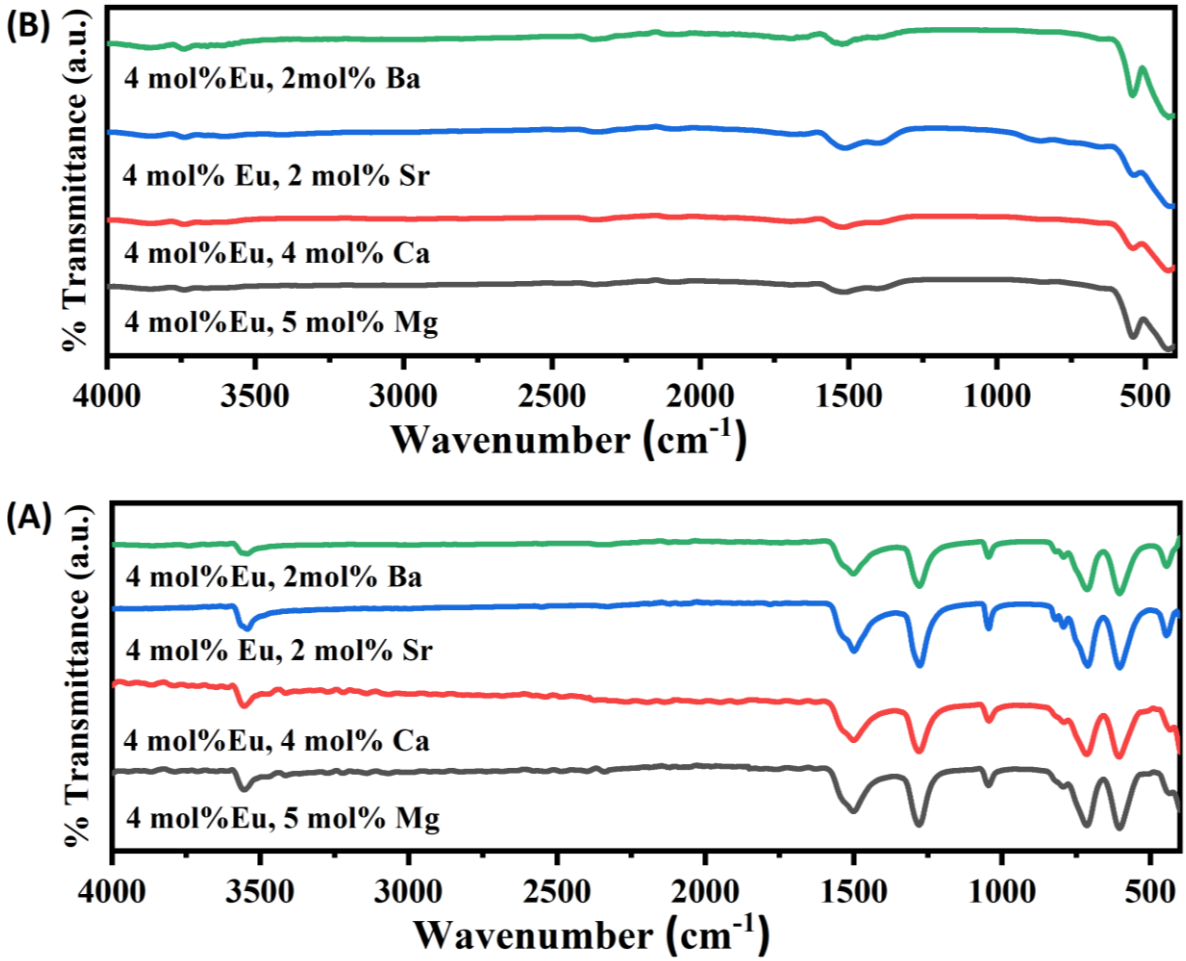

Figure 5.4: FTIR spectra of AEM co-doped (A) as-synthesized, and (B) calcined Gd_2O_3:4mol%Eu phosphors.

The small band around 3500 cm^{-1} is attributed to the stretching vibrations of the OH groups [13]. The peaks around 1500, 1288, and 1038 cm^{-1} are ascribed to the CO symmetric and asymmetric stretching vibrations. These bands are observed due to the absorption of CO_2 from the atmosphere during sample preparation. It is a well-known fact that OH-groups act as

luminescent quenchers and can be removed after calcination. It can be seen from the FTIR spectra of calcined samples that the band around 3500 cm^{-1} vanishes and the prominent band corresponding to the Gd-O vibrations is found at 545 cm^{-1} [14]. The obtained results confirm that after calcination, the samples are free from hydroxyl group and transformed into oxides. These results are consistent with the XRD results.

5.5 UV-Vis Measurements

Fig. 5.5 (a) represents the UV-visible absorbance spectra of the AEM co-doped samples. It can be observed from the UV-Visible spectra that all the AEM co-doped samples exhibit strong absorbance in the UV region. A small shift in the absorption band can be observed in all the samples. The co-doping of the alkaline-earth metals created energy levels due to the interstitial defects, which lead to the shifting in the absorption band.

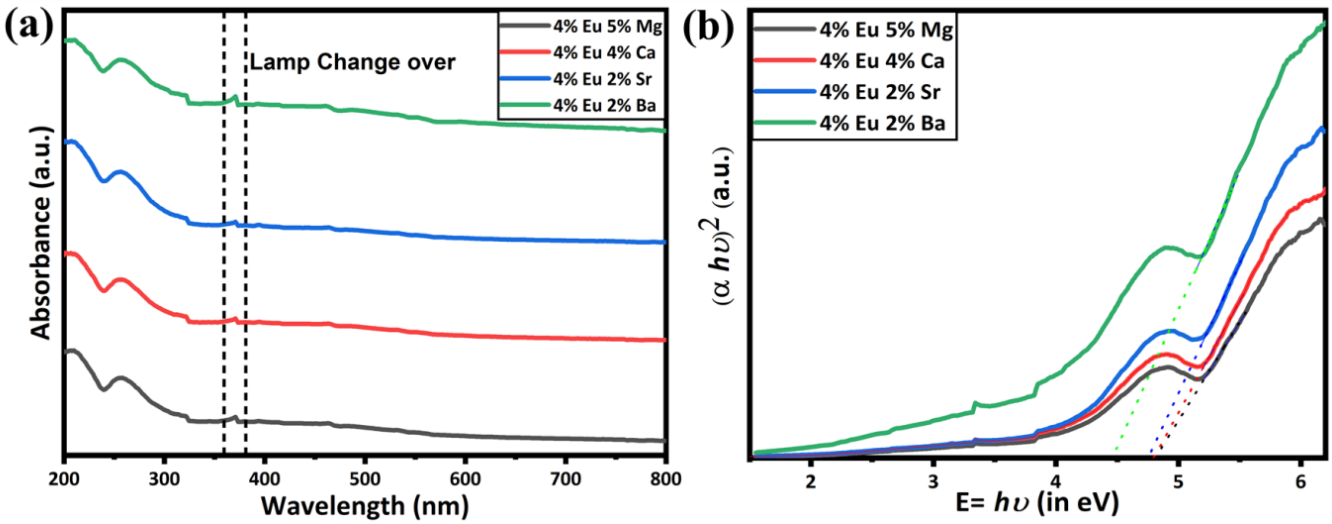

Figure 5.5: (a) UV-Vis absorbance spectra of AEM co-doped Gd_2O_3:4mol%Eu phosphors and (b) Tauc plots of respective samples.

The bandgap of all the samples is determined employing Tauc's formula, which represents the relationship between the absorption coefficient (α) and incident photon energy (hυ) as following [15]:

$$\alpha\, h\nu = A\,[h\nu - E_g]^n \qquad (5.3)$$

where, α represents the absorption coefficient, A is a constant, E_g is the bandgap (in eV), value of n i.e., 1/2, 2, 3/2, and 3 corresponds to the allowed direct, allowed indirect, forbidden direct and forbidden indirect transitions, respectively. The graph is plotted between $(\alpha\, h\upsilon)^2$ (along y-axis) and energy (hυ) in eV (along x-axis). The value of the bandgap is determined by extrapolating the straight portion of the $(\alpha\, h\upsilon)^2$ to the x-axis where hυ = 0. **Fig.**

5.5 (b) represents the Tauc plots of AEM co-doped samples. It can be observed that there is a decrease in the bandgap of the co-doped samples analogous to the Gd_2O_3:4mol%Eu [8].

The calculated bandgap values for the Mg, Ca, Sr, and Ba co-doped Gd_2O_3:4mol%Eu are given in **Table 5.1**. The variation in the bandgap is related to the degree of structural order-disorder variation in the lattice, which changes the intermediate energy levels within the bandgap. The ionic radii of AEM are different from the Gd^{3+} ions, which changes the structural parameters as observed from the XRD results. The increase in the crystallite size due to the expansion of the crystal structure is also responsible for the decrease in the bandgap. In addition to this, there is valency difference between alkaline earth metal cations and Gd^{3+}, which lead to the creation of oxygen vacancies. This may change the energy band structure leading to the enhancement in the deformation degree of O 2p orbits and the superposition of the electronic wave functions. The same phenomena were also observed in alkali metal co-doped Gd_2O_3:Eu samples [8].

5.6 Photoluminescence Studies

Photoluminescence (PL) excitation spectra of AEM co-doped Gd_2O_3:4mol%Eu phosphors in the region 200-300 nm recorded under 612 nm emission wavelength are shown in **Fig. 5.6**.

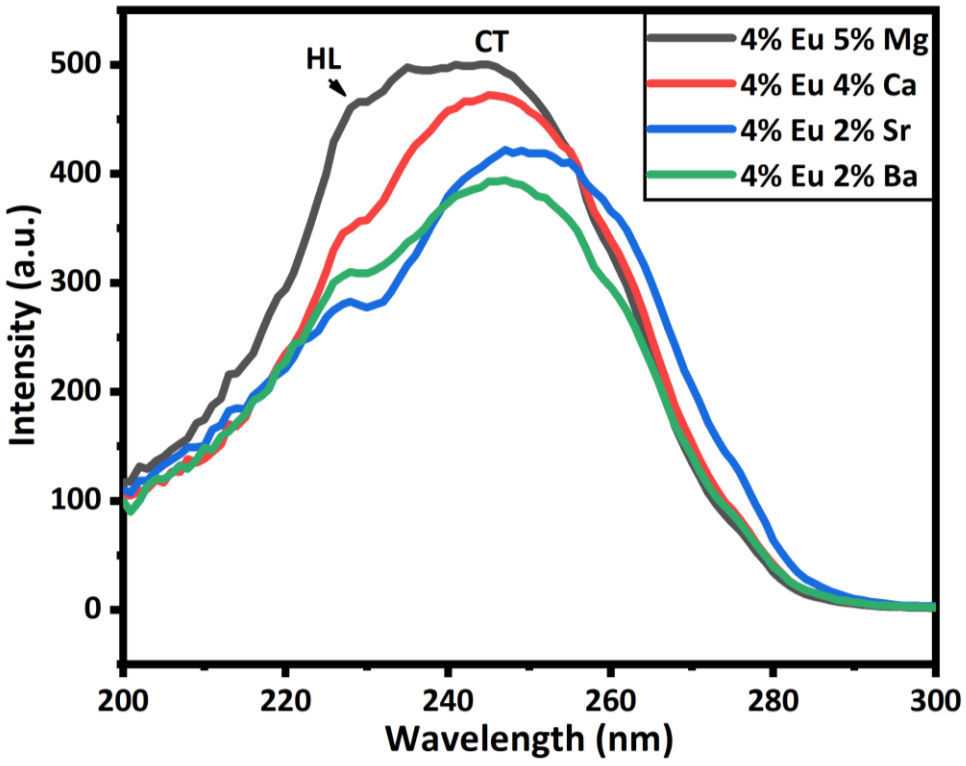

Figure 5.6: Excitation spectra of AEM co-doped Gd_2O_3:4mol%Eu phosphors.

The two main bands observed in the excitation spectra are charge transfer (CT) and host lattice (HL) bands. The bands observed around 228 nm is due to the band excitation of Gd_2O_3 and the band centered at 250 nm is Eu-O charge trasnfer band [16–19]. The charge transfer band is closely related to the covalency between the O^{2-} and Eu^{3+} ions and the coordination conditions around europium ions in the host lattice. The incorporation of the AEM in the host lattice changes the structural parameters. This results in the small variation in the excitation band. The emission spectra of AEM co-doped Gd_2O_3:4mol%Eu phosphors recorded under 250 nm charge transfer excitation in the range 550-750 nm are shown in **Fig. 5.7 (a-d)**.

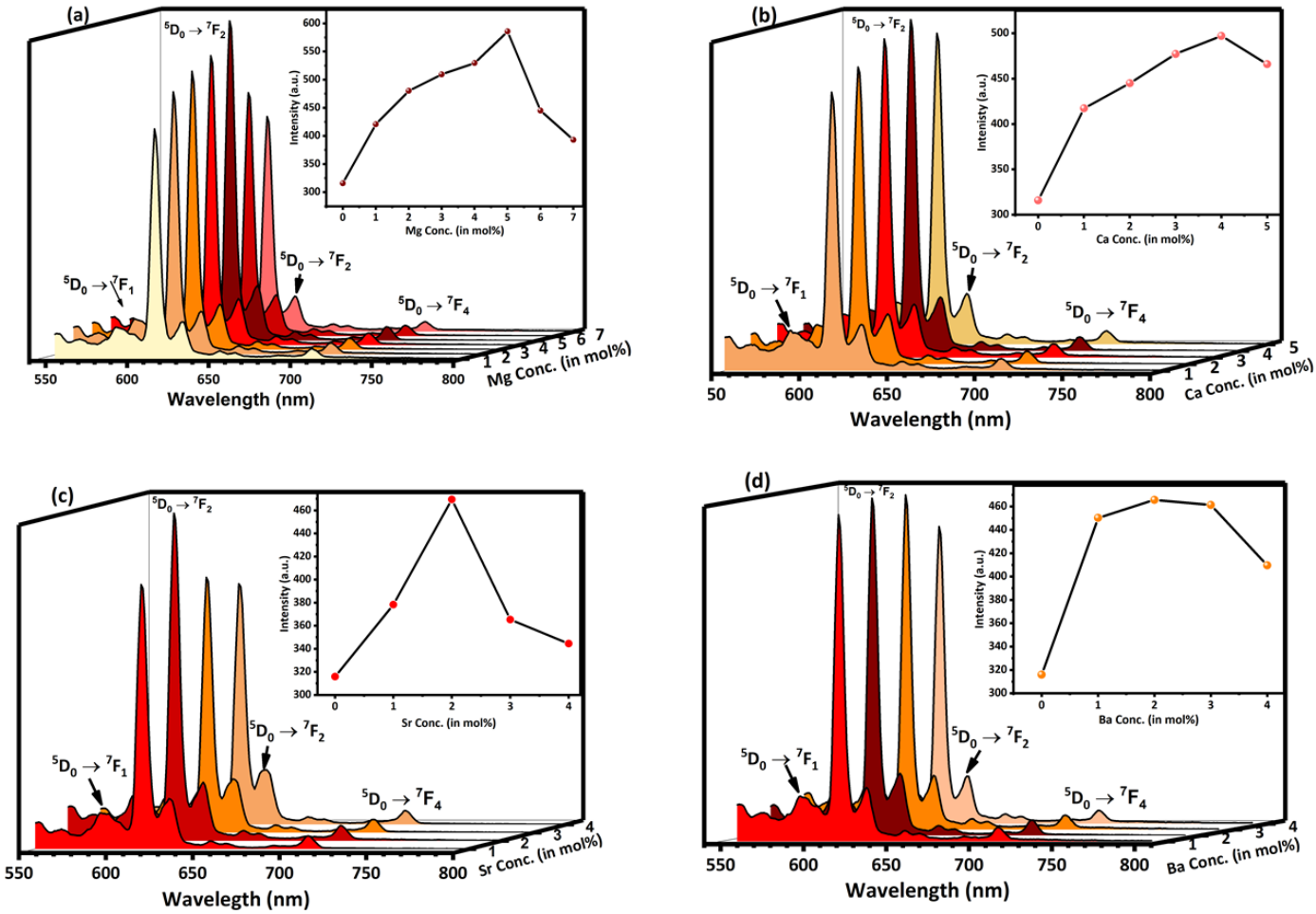

Figure 5.7: PL emission spectra of (a) Mg, (b) Ca, (c) Sr, and (d) Ba co-doped Gd_2O_3:4mol%Eu phosphors.

It can be seen from **Fig. 5.7 (a-d)** that major peaks are observed around 598, 611, 650, and 706 nm corresponding to the $^5D_0 \rightarrow {}^7F_{1,2,3,4}$ transitions of the Eu^{3+} ions [20–25]. Among all the transitions, $^5D_0 \rightarrow {}^7F_2$ transition, also called electric dipole transition, is the most intense and prominent transition. This transition is hypersensitive in nature and depends on the local environment of the Eu^{3+} ions in the host lattice. The other peak around 589 nm corresponds to

the $^5D_0 \rightarrow {}^7F_1$ transition, also known as magnetic dipole transition, which is insensitive to the local environment of europium ions.

In cubic-Gd_2O_3, there are two symmetry sites i.e., C_2 and S_6, which are present in the ratio 3:1, respectively [26]. The C_2 site possesses non-inversion symmetry, and the S_6 site has inversion symmetry, as shown in **Fig. 5.8.** When Eu^{3+} ions are present at non-centrosymmetric (C_2) sites without inversion center, the electric dipole transition ($^5D_0 \rightarrow {}^7F_2$) dominates. On the contrary, if Eu^{3+} ions are present at centrosymmetric site with inversion symmetry at S_6, then magnetic dipole transition ($^5D_0 \rightarrow {}^7F_1$) dominates. The asymmetry ratio ($\frac{\int I_{ed}\, d\lambda}{\int I_{md}\, d\lambda}$), which is the integrated intensity ratio of the electric to magnetic dipole transition, is indicative of the asymmetric environment of the Eu^{3+} in the host matrix. The value of the asymmetry ratio more than 1 indicates the highly asymmetric environment of the Eu^{3+} ions in the AEM co-doped samples [27]. The calculated values of the asymmetry ratio of all the samples are tabulated in **Table 5.2 (b).**

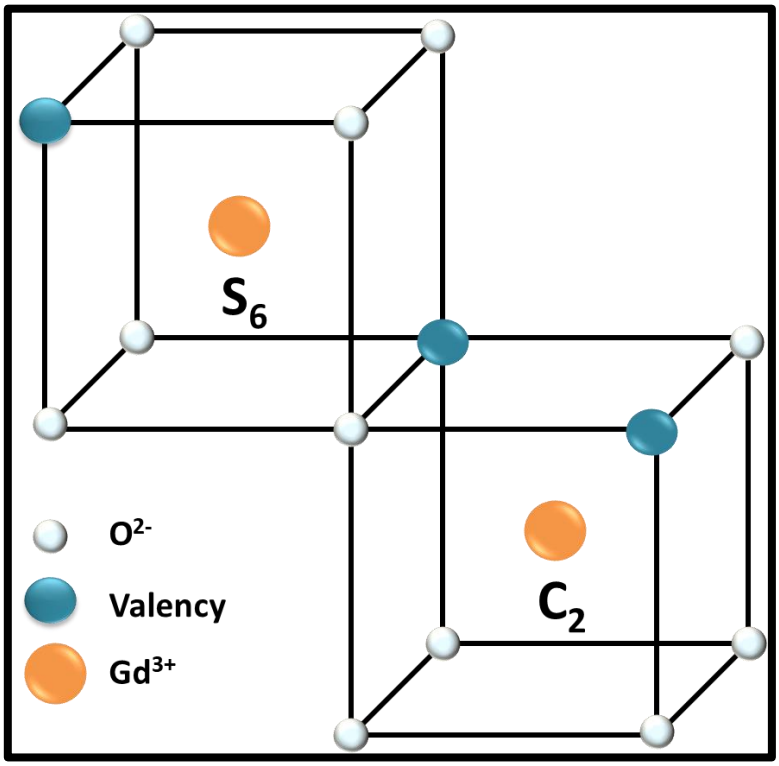

Figure 5.8: Symmetry sites in cubic-Gd_2O_3 lattice.

It can be illustrated from **Fig. 5.7 (a-d)** that there is a significant increase in the luminescent intensity with the co-doping of alkaline-earth metals in Gd_2O_3:Eu. In addition to this, irrespective of different AEM co-doping in the Gd_2O_3:Eu host matrix, shape and position

of all the emission peaks are identical. The only variation found is in the intensity of the peaks. The optimum value of the concentration doping is necessary to know for a particular optoelectronic application. It can be seen from AEM co-doped emission spectra that maximum PL intensity is found at 5, 4, 2, and 2 mol% for Mg, Ca, Sr, and Ba co-doped samples, respectively. The concentration quenching phenomenon occurred thereafter. The integrated intensity for Mg, Ca, Sr, and Ba co-doped samples are increased by factor of 1.85, 1.57, 1.48, and 1.47, as compared to the doped Gd_2O_3:Eu sample, respectively,. It is worth notable that PL intensity increases with the addition of the AEM, but the variation in the PL intensity for different concentrations is very less. The luminescence mechanism is shown in **Fig. 5.9**.

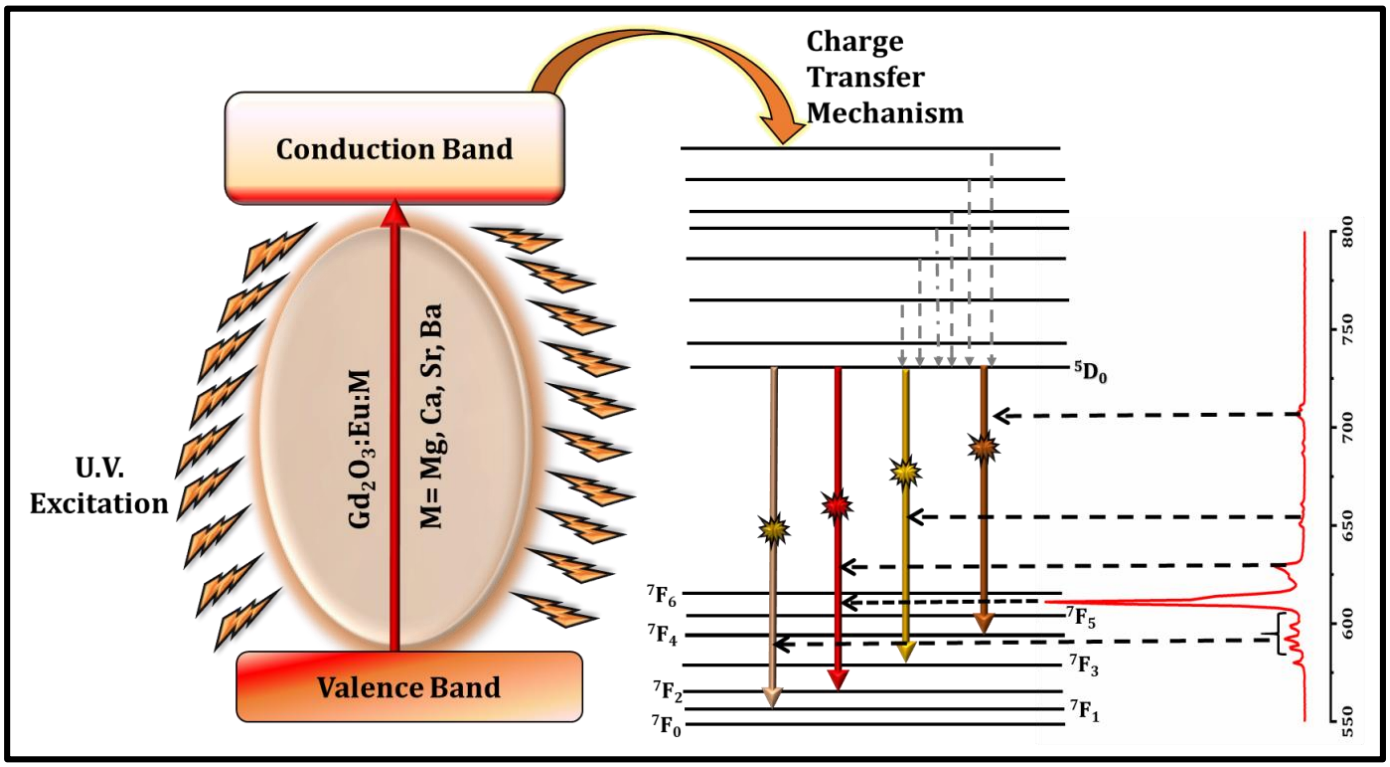

Figure 5.9: Luminescence mechanism in Gd_2O_3:Eu.

The main reason for the decrease in the luminescent intensity after the optimum concentration is the occurrence of the non-radiative transitions. The phenomenon of increase in the non-radiative transitions can be explained by employing Blasse's theory. According to Blasse's theory, the non-radiative transfer may occur due to the multipolar interactions or radiative re-absorption exchange interaction [26,28]. In general, the radiative re-absorption phenomenon comes into existence only when there is broad overlap of emission peaks of activator and sensitizer. In the present case, radiative re-absorption is omitted as there are no broad overlapping peaks. The critical distance (R_c) can be found by the following equation [29]:

$$R_c = 2\left[\frac{3V}{4\pi N X_c}\right]^{1/3} \quad (5.6)$$

where, V is unit cell volume, X_c is the concentration of the activator ions, N is the available sites for the activator in the host. The value of the R_c for Mg, Ca, Sr, and Ba co-doped sample is determined to be 12.304, 12.330, 12.318, and 12.308 Å, respectively. According to Blasse's equation, value of $R_c \leq 5$ Å leads to non-radiative transitions. The value of R_c greater than 5 Å, multipole-multipole transitions are considered for the concentration quenching phenomenon. Thus, in case of AEM co-doped samples, multipole-multipole transitions are responsible for concentration quenching.

The main reason for the variation in the PL intensity is the difference between the ionic radii and the valency of the AEM co-doped and host lattice ions. AEM ions can either occupy interstitial sites or can substitute the Gd^{3+} ions. The size of the AEM ions is close to or greater than the Gd^{3+}. Thus, their probability is to occupy the substitutional sites in the host lattice is more. Among all the alkaline earth metals, Mg^{2+} ions have the smallest ionic radii, so the maximum PL is found for 5 mol% of Mg^{2+} ions, while the size of Sr^{2+} and Ba^{2+} are large, so they can not be accommodated in higher quantity in the host lattice, and the maximum PL is found at 2 mol% for them. Furthermore, PL is highly influenced by the local coordination of the Eu^{3+} ions. The incorporation of the alkaline earth metal ions leads to the change in the coordination conditions such as Eu-O distance. The distortion in the Eu-O and the local symmetry of the Eu^{3+} ions lead to the evolution of the 4f transition probabilities of the Eu^{3+} ions, which leads to the enhancement in the AEM co-doped Gd_2O_3 phosphors. Furthermore, alkaline-earth metal ions are aliovalent ions. The valency of the AEM ions is +2, while Gd has +3 state. The substitution of the AEM in the host lattice results in the formation of electron-hole (e-h) pairs [19,30]. This leads to the formation of oxygen vacancies. The increase in the AEM concentration results in the substantial increase in the oxygen vacancies. These oxygens act as sensitizers and increase the charge transfer rate. The excess oxygen vacancies will destroy the crystallinity of the host and lead to decrease in the luminescence intensity.

The variation in the luminescent behavior of the AEM co-doped samples in Gd_2O_3:4mol% Eu is further investigated by Judd-Ofelt (J-O) analysis [31]. The Judd-Ofelt (Ω_2, Ω_4, Ω_6) and other radiative parameters are also calculated from the emission spectra as given in **Table 5.2 (a)**. Ω_2 depends highy on the local environment and represents the structural changes and covalency of Eu^{3+} ions. Ω_4 and Ω_6 are associated with macroscopic properties like viscosity and the rigidity of the matrix. The magnetic dipole transition ($^5D_0 \rightarrow {}^7F_1$) is considered as reference to calculate the intensity parameters [32].

Table 5.2 (a): Judd-Ofelt parameters of AEM co-doped Gd_2O_3:Eu phosphors.

Judd-Ofelt Intensity Parameters					
Concentration (in mol%)	**Ω_2 (10^{-20} cm^2)**	**Ω_4 (10^{-20} cm^2)**	**A_{0-1} (sec^{-1})**	**A_{0-2} (sec^{-1})**	**A_{0-4} (sec^{-1})**
Gd_2O_3:4mol%Eu,Mg					
1.0	2.747	0.248	50	150.4	6.40
2.0	2.847	0.2531	50	155.9	6.52
3.0	2.992	0.245	50	163.8	6.31
4.0	2.939	0.246	50	160.9	6.33
5.0	3.398	0.290	50	185.8	7.20
6.0	2.933	0.238	50	160.4	6.13
7.0	2.337	0.267	50	129.5	6.88
Gd_2O_3:4mol%Eu,Ca					
1.0	2.764	0.270	50	151.3	6.96
2.0	2.886	0.238	50	157.9	6.13
3.0	2.800	0.245	50	153.2	6.31
4.0	3.282	0.267	50	179.5	6.89
5.0	2.946	0.238	50	161.3	6.15
Gd_2O_3:4mol%Eu,Sr					
1.0	2.732	0.236	50	149.4	6.08
2.0	3.250	0.275	50	177.5	7.07
3.0	2.741	0.247	50	150.0	6.35
4.0	2.909	0.264	50	159.4	6.79
Gd_2O_3:4mol%Eu,Ba					
1.0	3.026	0.278	50	165.3	7.16
2.0	2.933	0.272	50	160.3	7.00
3.0	3.153	0.306	50	171.9	7.89
4.0	3.142	0.324	50	171.2	8.33

Using the method described by Kodaira *et al.* [33], Judd-Ofelt intensity parameters are calculated. According to this method, radiative emission rates ($A_{0-2,4}$ and A_{0-1}) and integrated emission intensities (area under the curve) are related to each other by the following expression:

$$\frac{A_{0-2,4}}{A_{0-1}} = \frac{I_{0-2,4}}{I_{0-1}} \frac{h\nu_{0-1}}{h\nu_{0-2,4}} \tag{5.7}$$

where, I_{0-j} is the integrated emission intensity, and ν_{0-j} is the energy barycentre corresponding to a particular transition. The magnetic dipole transition was taken to be 50 sec^{-1}. The radiative rates of the electric dipole transitions ($^5D_0 \rightarrow {}^7F_2$ and $^5D_0 \rightarrow {}^7F_4$) are calculated. The radiative emission rates ($A_{0-2,4}$) as a function of J-O intensity (Ω_2 and Ω_4) parameters are formulated as:

$$A_{0-J} = \frac{64\pi^4(\nu_{0-2,4})^3 e^2}{3hc^3} \frac{1}{4\pi\varepsilon_0} \chi \sum_j \text{ (j= 2, 4) } [\Omega_j <{}^5D_o|U(J)|{}^7F_{2,4}>^2] \tag{5.8}$$

where, χ is the Lorentz local field correction factor, which is a function of the refractive index of the host. The values of non-zero squared reduced matrix elements ($<^5D_0|U(J)|^7F_{2,4}>^2$) are $<^5D_0|U(J)|^7F_2>^2 = 0.0032$, and $<^5D_0|U(J)|^7F_4>^2 = 0.0023$ corresponding to the $^5D_0 \rightarrow {}^7F_2$, $^7F_4$ transitions, respectively. The other radiative parameters such as transition probabilities, radiative lifetimes, branching ratio, and radiative stimulated cross-section are calculated using Judd-Ofelt parameters. The calculated values of Judd-Ofelt and other radiative parameters are given in **Table 5.2** (a-b).

Table 5.2 (b): Radiative parameters and Asymmetry ratio of AEM co-doped Gd_2O_3:Eu phosphors.

Concentration (in mol%)	**A_T (Ψ_j) (s^{-1})**	**τ_{rad} (ms)**	**Branching ratio** (in %)			**Asymmetry ratio**	**Stimulated emission cross-section (cm^2)**		
			β_{0-1}	**β_{0-2}**	**β_{0-4}**		**σ_{0-1} (10^{-22})**	**σ_{0-2} (10^{-21})**	**σ_{0-4} (10^{-22})**
Gd_2O_3:4mol%Eu,Mg									
1.0	206.8	4.835	24.18	72.73	3.10	2.56	0.845	1.212	0.708
2.0	212.4	4.071	23.54	73.39	3.07	2.65	0.878	1.261	0.746
3.0	220.1	4.543	22.72	74.42	2.87	2.78	0.903	1.322	0.722
4.0	217.2	4.603	23.02	74.07	2.91	2.75	0.879	1.310	0.717
5.0	243.0	4.118	20.57	76.46	2.96	3.10	0.953	1.472	0.879
6.0	216.6	4.617	23.09	74.08	2.83	2.69	0.934	1.268	0.724
7.0	186.3	5.366	26.83	69.48	3.69	2.61	0.799	1.099	0.756
Gd_2O_3:4mol%Eu,Ca									
1.0	208.2	4.08	24.33	72.65	3.34	2.55	0.819	1.214	0.765
2.0	214.1	4.67	21.32	73.78	2.86	2.66	0.934	1.264	0.724
3.0	209.5	4.77	24.23	73.12	3.01	2.59	0.855	1.237	0.702
4.0	236.4	4.23	23.13	75.94	2.91	3.02	0.102	1.431	0.815
5.0	217.4	4.99	24.33	74.18	2.83	2.74	0.816	1.303	0.698
Gd_2O_3:4mol%Eu,Sr									
1.0	205.5	4.86	24.33	72.71	2.96	2.50	0.825	1.184	0.676
2.0	234.6	4.26	21.32	75.67	3.01	2.90	0.101	1.394	0.861
3.0	206.4	4.84	24.23	72.70	3.08	2.55	0.812	1.207	0.700
4.0	216.2	4.62	23.13	73.73	3.14	2.73	0.925	1.295	0.744
Gd_2O_3:4mol%Eu,Ba									
1.0	222.4	4.96	22.48	74.30	3.22	2.69	0.970	1.262	0.843
2.0	217.3	4.60	23.01	73.77	3.22	2.64	0.889	1.249	0.808
3.0	229.8	4.35	21.76	74.81	3.43	2.72	0.102	1.300	0.941
4.0	229.5	4.36	21.79	74.58	3.63	2.67	0.974	1.264	0.980

The total radiative transition probability, radiative lifetime, branching ratio, stimulated emission cross-section are calculated using following expressions:

$$\mathbf{A_T(\Psi_j)} = \Sigma A_{J\text{-}J'} \qquad (5.9)$$

$$\tau_{rad}(\psi_J) = \frac{1}{A_T(\psi_J)} \tag{5.10}$$

$$\beta(\psi_J) = \frac{A(\psi_J, \psi'_{J'})}{\sum A_J(\psi_J)} \tag{5.11}$$

$$\sigma(\lambda_p)(J \rightarrow J') = \frac{\lambda_P^4}{8\, c\, n^2\, \Delta\lambda_{eff}} A_{rad}(J \rightarrow J') \tag{5.12}$$

The calculated values of spectral parameters are given in **Table 5.2 (b)**. It can be observed from **Table 5.2 (a-b)** that trend $\Omega_2 > \Omega_4$ is followed in all the samples. The variation in Ω_2 represents the highly asymmetric environment of the co-doped samples. The $\beta(\psi_J)$ corresponding to the $^5D_0 \rightarrow {}^7F_2$ transition is found to be more than 70% for all the samples, which makes them promising candidates for solid-state lighting devices.

The photometric parameters such as CIE coordinates and CCT values of the AEM co-doped samples are calculated. The calculated CIE coordinates and CCT values of the samples are tabulated in **Table 5.3**.

The CIE coordinates are calculated with the help of the color calculator MATLAB program in MATLAB 9.1 (version R2017b). The calculated CIE coordinates of AEM co-doped Gd_2O_3:Eu phosphors are shown in the CIE chromaticity diagram (**Fig. 5.9**).

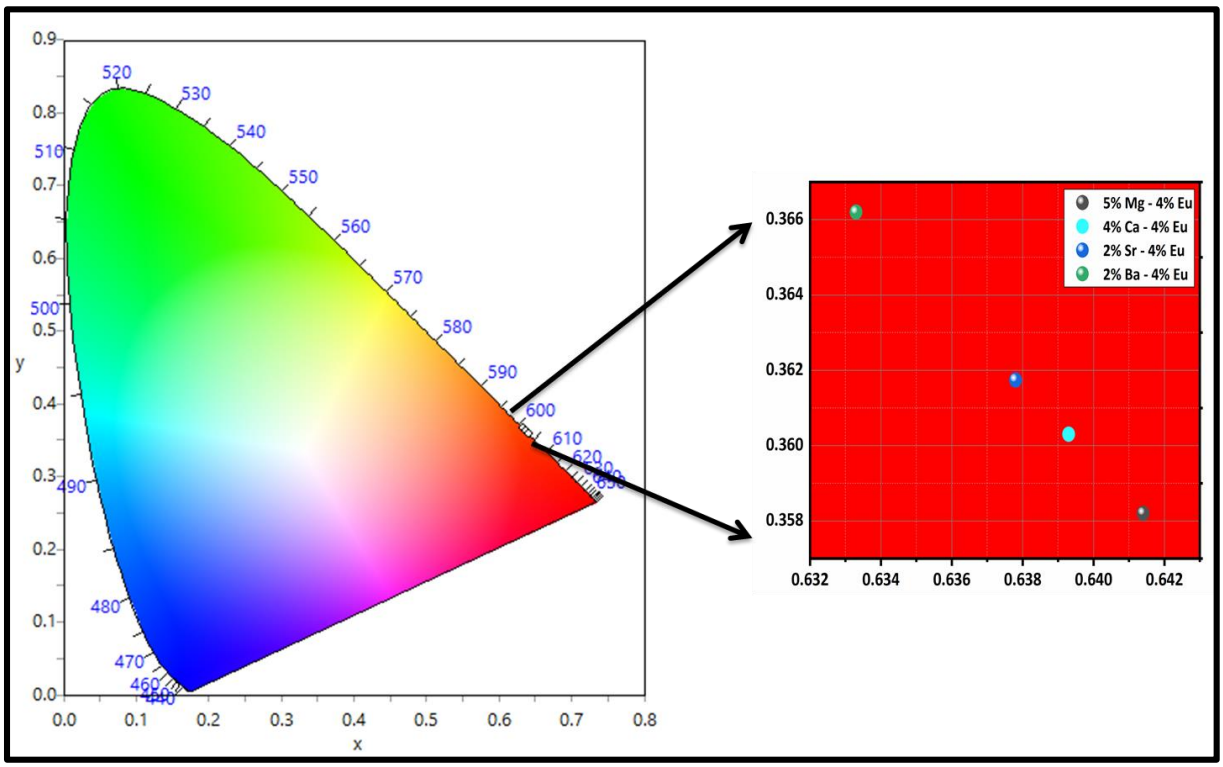

Figure 5.9: Chromaticity diagram of AEM co-doped Gd_2O_3:4mol%Eu phosphors.

The CIE coordinates lie in the deep-red region, which is close to the coordinates of the ideal red color (0.67, 0.33) standardized by NTSC. The calculated CIE coordinates are close to the edge of the CIE diagram indicating the better color purity of the synthesized phosphors for the display devices.

McCamy's empirical formula was used to find CCT values as follows [34]:

$$\mathbf{CCT} = -473\ n^3 + 3601\ n^2 - 6861\ n + 5514.31 \quad (5.13)$$

where, $n = (x-x_e)/(y-y_e)$ and x_e (0.3320) and y_e (0.1858) are the coordinates of the chromaticity epicenter.

Table 5.3: CIE and CCT values of AEM co-doped Gd_2O_3:Eu phosphors.

Sample Name	**CIE Coordinates**		**CCT (K)**
	x	**y**	
Gd_2O_3:4%Eu5%Mg	0.6414	0.3582	1097
Gd_2O_3:4%Eu4%Ca	0.6393	0.3603	1114
Gd_2O_3:4%Eu2%Sr	0.6378	0.3617	1162
Gd_2O_3:4%Eu2%Ba	0.6333	0.3662	1125

CCT values are calculated and found to be less than 5000 K. In general, CCT values less than 5000 K indicate the warm light and are suitable for the solid-state lighting appliances [5]. It can be concluded from the obtained values of the photometric parameters that AEM co-doped Gd_2O_3:Eu phosphors are potential candidates for efficient red light-emitting phosphors in display devices.

References

1 D. Kumar, M. Sharma and O. P. Pandey, *Opt. Mater. (Amst).*, 2014, **36**, 1131–1138.

2 N. Dhananjaya, H. Nagabhushana, B. M. Nagabhushana, B. Rudraswamy, C. Shivakumara and R. P. S. Chakradhar, *J. Alloys Compd.*, 2011, **509**, 2368–2374.

3 K. Mondal, P. Kumari and J. Manam, *Curr. Appl. Phys.*, 2016, **16**, 707–719.

4 M. Manhas, V. Kumar, V. Sharma, O. M. Ntwaeaborwa and H. C. Swart, *Nano-Structures & Nano-Objects*, 2015, **3**, 9–16.

5 P. Kumari and J. Manam, *Spectrochim. Acta - Part A Mol. Biomol. Spectrosc.*, 2016, **152**, 109–118.

6 H. Shi, X.-Y. Zhang, W.-L. Dong, X.-Y. Mi, N.-L. Wang, Y. Li and H.-W. Liu, *Chinese Phys. B*, 2016, **25**, 047802–047806.

7 Z. Liu, Q. Wang, Y. Yang, C. Tao and H. Yang, *J. Nanopart Res*, 2010, **12**, 2233–2240.

8 R. Priya and O. P. Pandey, *J. Lumin.*, 2019, **212**, 342–353.

9 R. A. Mir, P. Sharma and O. P. Pandey, *Sci. Rep.*, 2017, **7**, 1–12.

10 R. A. Mir and O. P. Pandey, *J. Clean. Prod.*, 2019, **218**, 644–655.

11 K. Zhang, H. Dondapati, T. Holloway, W. Cao, A. Kar, A. Patra and A. K.Pradhan, *J. Nanophotonics*, 2010, **4**, 043517.

12 G. Boopathi, S. Gokul Raj, G. Ramesh Kumar, R. Mohan and S. Mohan, *Indian J. Phys.*, 2018, **92**, 715–724.

13 F. Chen, X. H. Zhang, X. D. Hu, W. Zhang, R. Zeng, P. D. Liu and H. Q. Zhang, *J. Alloys Compd.*, 2016, **664**, 311–316.

14 G. Liu, S. Zhang, X. Dong and J. Wang, *J. Nanomater.*, 2010, **2010**, 2–7.

15 J. Tauc, R. Grigobovici and A. Vancu, *Phys. Stat. Sol.*, 1966, **15**, 627–637.

16 N. Dhananjaya, H. Nagabhushana, B. M. Nagabhushana, B. Rudraswamy, C. Shivakumara and R. P. S. Chakradhar, *Bull. Mater. Sci.*, 2012, **35**, 519–527.

17 R. Priya and O. P. Pandey, *Vacuum*, 2018, **156**, 283–290.

18 N. Dhananjaya, H. Nagabhushana, S. C. Sharma, B. Rudraswamy, C. Shivakumara and B. M. Nagabhushana, *J. Alloys Compd.*, 2014, **587**, 755–762.

19 N. Dhananjaya, H. Nagabhushana, B. M. Nagabhushana, B. Rudraswamy, C. Shivakumara, K. Narahari and R. P. S. Chakradhar, *Spectrochim. Acta - Part A Mol. Biomol. Spectrosc.*, 2012, **86**, 8–14.

20 R. S. Ukare, G. D. Zade, B. Deva Prasad Raju and S. J. Dhoble, *Optik (Stuttg).*, 2016, **127**, 1871–1878.

21 G. R. Dillip, S. J. Dhoble, L. Manoj, C. Madhukar Reddy and B. Deva Prasad Raju, *J. Lumin.*, 2012, **132**, 3072–3076.

22 B. Deva Prasad Raju and C. Madhukar Reddy, *Opt. Mater. (Amst).*, 2012, **34**, 1251–1260.

23 J. H. Jeong, J. S. Bae, S. Yi and J. Park, *J. Phys. Condens. Matter*, 2003, **567**, 567–574.

24 L. Li, L. Liu, W. Zi, H. Yu, S. Gan, G. Ji, H. Zou and X. Xu, *J. Lumin.*, 2013, **143**, 14–20.

25 W. Luo, J. Liao, R. Li and X. Chen, *Phys. Chem. Chem. Phys.*, 2010, **12**, 3276–3282.

26 M. Buijs and A. Meyerink, *J. Lumin.*, 1987, **37**, 9–20.

27 D. Kumar and S. J. Manam, *Appl. Phys. A*, 2018, **124**, 261–276.
28 R. A. Barve, N. Suriyamurthy, B. S. Panigrahi and B. Venkatraman, *Phys. B Condens. Matter*, 2015, **475**, 156–161.
29 G. Blasse, *J. Solid State Chem.*, 1986, **62**, 207–211.
30 J. Li, Y. Wang and B. Liu, *J. Lumin.*, 2010, **130**, 981–985.
31 B. M. Walsh, *Adv. Spectrosc. Lasers Sens.*, 2006, **231**, 403–433.
32 M. Chang, Y. Song, Y. Sheng, J. Chen, H. Guan, Z. Shi, X. Zhou, K. Zheng and H. Zou, *J. Phys. Chem. C*, 2017, **121**, 2369–2379.
33 S. Som, A. K. Kunti, V. Kumar, V. Kumar, S. Dutta, M. Chowdhury, S. K. Sharma, J. J. Terblans and H. C. Swart, *J. Appl. Phys.*, 2014, **115**, 0–14.
34 C. S. McCamy, *Color Res. Appl.*, 1992, **17**, 142–144.

CHAPTER 6

RESULTS AND DISCUSSION III

Overview

The photoluminescene intensity of the phosphors depends on many factors in which morphology has a significant role. To engineer the morphology, different surfactants are used during synthesis. The effect of the surfactants on the structural, morphological, and luminescent properties of Gd_2O_3:4mol%Eu phosphors are discussed in this chapter. Trioctylphosphine oxide (TOPO) and cetyltrimethylammonium bromide (CTAB) are used as surfactants in different molar ratios during synthesis. The present chapter illustrates the role of surfactants to modify the morphology and further its effects on altering the luminescent features of the synthesized phosphors.

6.1 Introduction

Lanthanide functionalized rare-earth oxide phosphors form a promising class of luminescent materials that find vast applications in the field of optoelectronic devices, display devices, bio-sensors, bio-imaging, etc. [1–3]. Among the various rare-earth oxide materials, Gd_2O_3 possesses better physical, chemical and thermal stability. It has low phonon energy, paramagnetic behavior, high density, etc. Eu^{3+} doped Gd_2O_3 is a red light-emitting phosphor and finds many potential applications [4–9].

It is a well-known fact that particle size, morphology, crystal structure, and defect-free surface are the critical parameters that determine the luminescent properties of any phosphor [10–17]. To achieve the aforementioned parameters, synthesis route plays an important role. Gd_2O_3 phosphors are synthesized via several synthesis routes [18–21]. Among the chemical routes, co-precipitation method is a facile and economical route to synthesize nanoparticles of uniform size in less time and at low-temperature. This can be done with the variation of the pH, temperature, and time. However, to induce crystallization, the materials obtained through this route are fired at higher temperatures. Also, surfactants play an important to alter the morphological features, which in turn have significant effects on the optical and luminescent properties. These surfactants provide favorable synthesis sites for the growth of precursors and also control the size via electrostatic repulsion and stearic hindrance [22,23]. Thus, a proper choice of surfactant is required to engineer the morphology of nanoparticles. Jadhav *et al*. reported the influence of EDTA on size-controlled emission properties of Y_2O_3:Eu^{3+} synthesized via co-precipitation method [24]. Dhananjaya *et al*. studied the growth of Gd_2O_3:Eu synthesized via hydrothermal method using CTAB [25]. Till date, no report is available on the effect of CTAB and TOPO on the luminescent behavior of Gd_2O_3:4mol%Eu synthesized via co-precipitation method. In the present chapter, we have reported the role of surfactants on the structural, morphological, optical, and magnetic properties of Gd_2O_3:Eu phosphors synthesized via co-precipitation route. The concentration of europium ions is fixed 4 mol% to study the effect of surfactants only. All the results are discussed in detail. The synthesis details of the phosphors are already given in the ***Chapter 3*** (**Table 3.1**), however for simplicity, details of the samples are given in **Table 6.1**.

Table 6.1: Sample labels and synthesis conditions for surfactant assisted/free Gd_2O_3:4mol%Eu samples.

S. No.	Sample ID	Surfactant	Ratio (Metal ion: Surfactant)	Calcination Temperature (℃)
1.	GOE	-	-	800, 1000
2.	GOEC1	CTAB	1:0.5	800, 1000
3.	GOEC2	CTAB	1:1	800, 1000
4.	GOEC3	CTAB	1:2	800, 1000
5.	GOET1	TOPO	1:0.5	800, 1000
6.	GOET2	TOPO	1:1	800, 1000
7.	GOET3	TOPO	1:2	800, 1000

6.2 XRD Study

Fig. 6.1 represents the XRD patterns of GOE samples calcined at different temperatures varying from 200 to 1000 ℃. XRD patterns at 200 ℃ correspond to the $Gd(OH)_3$ phase when compared to standard ICDD (International center for diffraction data) card number 01-083-2037 with hexagonal structure and space group no. P63/m.

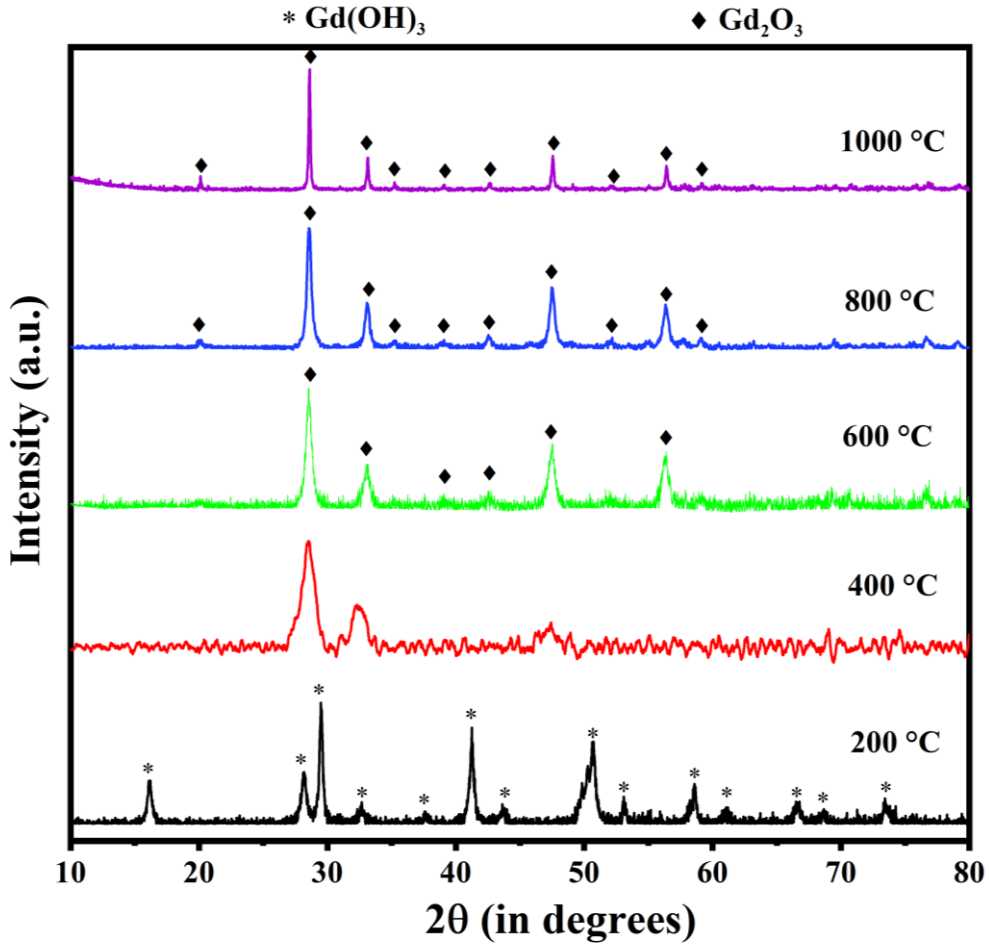

Figure 6.1: XRD patterns of GOE at different temperatures.

As the temperature is increased, cubic Gd_2O_3 phase starts to grow at 600 ℃. However, XRD patterns are not sharp at 600 ℃. When the calcination temperature is 800 ℃, pure Gd_2O_3 phase is observed. All the XRD peaks at this temperature correspond to the pure cubic Gd_2O_3 phase (ICDD card number 03-065-3181) with $Ia\bar{3}$ (206) space group. No impurity peak(s) corresponding to other intermediate phase(s) are observed, indicating the formation of pure cubic Gd_2O_3 phase. The crystallinity of the XRD patterns is enhanced when the temperature is 1000 ℃.

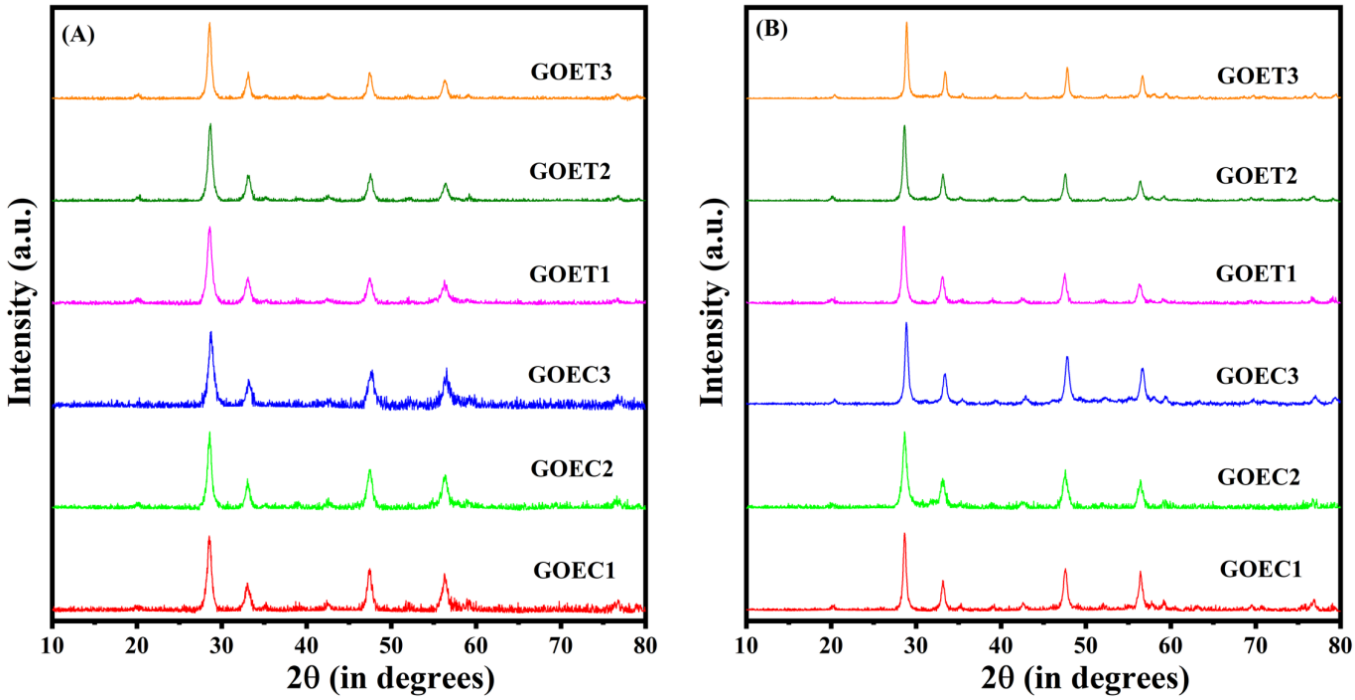

Figure 6.2: XRD patterns of CTAB and TOPO assisted Gd_2O_3:4mol%Eu phosphors calcined at (A) 800 ℃, and (B) 1000 ℃.

Fig. 6.2 (A-B) represents the XRD patterns of the CTAB and TOPO assisted Gd_2O_3:Eu samples calcined at 800 and 1000 ℃. It can be seen from the diffractograms that all the peaks correspond to the cubic Gd_2O_3 phase. No change in the crystal structure is observed even with the use of the surfactants. However, in case of surfactant-assisted samples, better crystallinity is achieved at 1000 ℃. Thus, other structural, optical, and luminescent properties are studied for the samples calcined at 1000 ℃. The average crystallite size is calculated using Scherrer formula [26]. The calculated value of the average crystallite size of GOE, GOEC1, GOEC2, GOEC3, GOET1, GOET2, and GOET3 are 31.83, 20.27, 14.08, 18.88, 17.84, 20.85, and 26.57 nm, respectively. In the case of surfactant capped samples, there is decrease in the crystallite size because surfactants act as size inhibitors during the growth of the particles. Among the CTAB and TOPO capped samples, better crystallinity is found in case of TOPO assisted

samples. It is a well-known fact that PL emission enhances with increase in the crystallization of samples.

6.3 Morphological Studies

Fig. 6.3 (a) represents the micrograph of the Gd_2O_3:Eu synthesized without any aid of surfactant. It can be observed from the figure that the synthesized material consists of the nano-rods. The formation of the rods can be described by the self-rolling mechanism. The addition of the precipitating agent at high pH value results in the formation of elongated structure in one dimension. To observe the effects of the surfactant addition on the morphology of the particles, CTAB and TOPO surfactants are used in different molar ratios. **Fig. 6.3 (b-d)** represents the microstructures of the CTAB assisted Gd_2O_3:Eu phosphors. When the concentration of CTAB is low as 1:0.5 (metal ion:CTAB), morphology of the particles is slightly changed. The morphology is slightly deviated from the rod-like morphology. The micrographs appear to be more like particles embedded on the surface of the rods, giving them a non-uniform elongated structure. As CTAB concentration is increased by 1:1 (metal:surfactant), morphology represent the particles sticking together with each other. The particle size is found in the range 50-80 nm. When CTAB concentration is 1:2 (metal:surfactant), micrographs consist of particles with non-uniform round shape spheres. The particle size is also reduced due to the high concentration of the surfactants. It can be observed that the introduction of the CTAB during synthesis alters the morphology. However, no such better microstructures are obtained with monodispersity and less agglomeration in case of CTAB assisted samples.

Fig. 6.3 (e-g) represents the TOPO assisted Gd_2O_3:Eu microstructures. When the concentration of TOPO is low as 0.5 (metal:surfactant), monodispersed and uniform rod-like morphology can be observed. When the concentration of the TOPO is increased as 1:1, rod-like morphology is observed. At higher concentration (1:2), the morphology consists of mostly non-uniform elongated structures. Thus, at higher concentrations of TOPO, microstructures are non-uniform and agglomerated. It can be observed that in the case of CTAB assisted samples; microstructures have rod-like to spherical features. However, in the case of TOPO assisted samples, morphology consists of almost elongated structures. This can be ascribed to the fact that CTAB is a cationic surfactant with a positive charge consisting of the long hydrocarbon chain. This leads to the repulsion with the metal ions and increases stearic hindrance in the system [14,27,28]. In the case of TOPO, it has a weak polar P=O bond, since TOPO is a non-ionic surfactant and weakly soluble in water. Thus, it has high stability and leads to the formation of better morphology than the ionic surfactant [29,30]. In conclusion, the samples prepared with

TOPO have better morphology than the samples prepared with CTAB surfactants. **Fig. 6.3 (a-b)** represents the TEM microstructures of the CTAB and TOPO assisted Gd_2O_3:Eu samples. The presence of particles and monodispersity can also be observed from these microstructures.

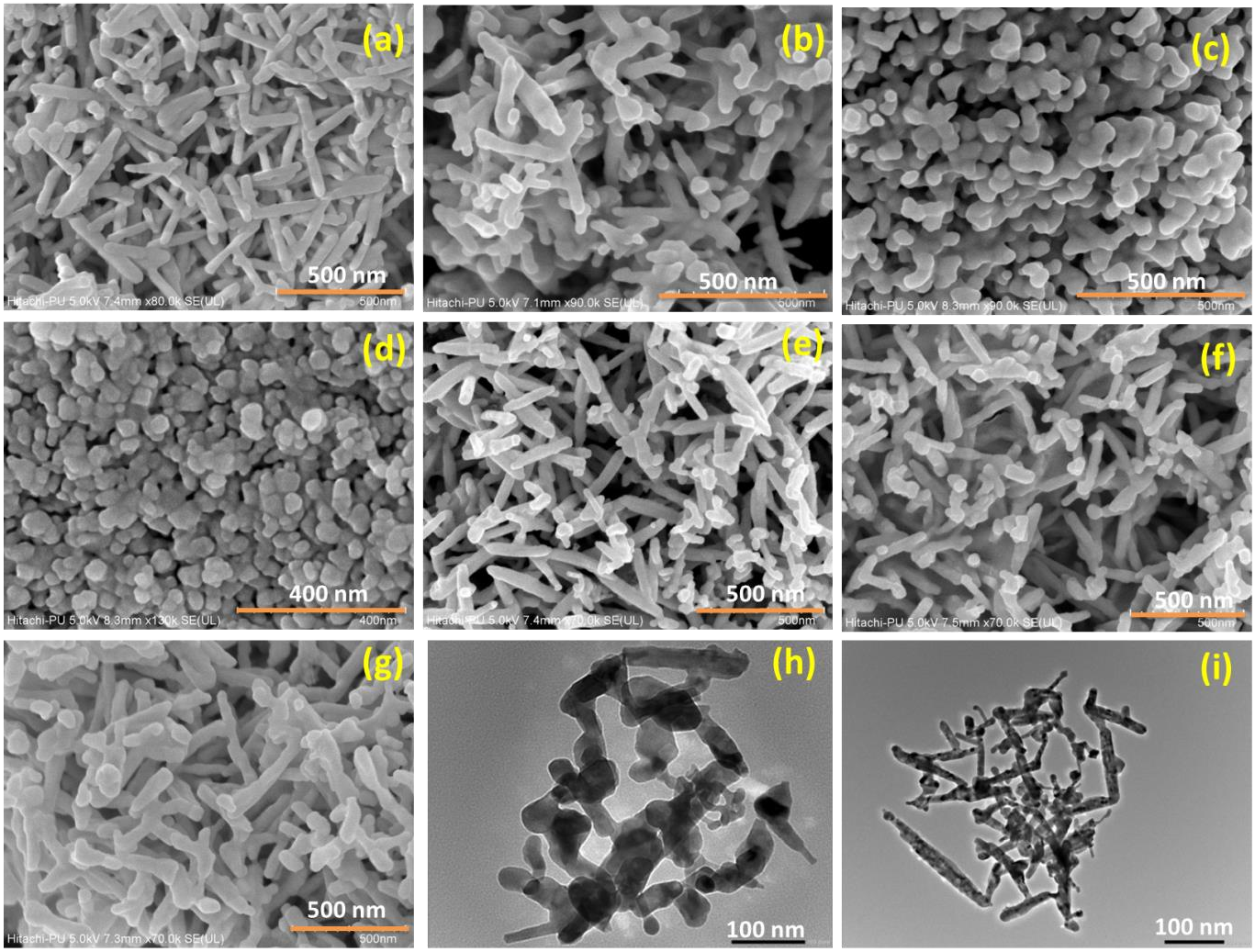

Figure 6.3: FESEM micrographs of Gd_2O_3:Eu with (a) No surfactant (GOE), (b) GOEC1, (c) GOEC2, (d) GOEC3, (e) GOET1, (f) GOET2, (g) GOET3, TEM micrographs of (h) GOEC1 and (i) GOET1 sample.

6.4 Fourier Transform Infrared (FTIR) Analysis

The IR-vibrational spectra and presence of the other functional groups of Gd_2O_3:Eu is shown in **Fig. 6.4.** GOE sample exhibits major bands at 435, 538, 897, 1398, and 1520 cm^{-1}. The peak around 897 cm^{-1} is attributed to the out of plane O-H vibrations, which are due to the presence of adsorbed water molecules from the atmosphere [31]. The small peak around 1398 and 1520 cm^{-1} are due to the N-O stretching vibrations [17]. The weak band around 435 cm^{-1} and strong absorption band around 538 cm^{-1} are due to Gd-O vibrations [32]. The similar peaks can also be observed in other samples, which are synthesized using surfactants. However, it can be

seen that there is change in the intensity and position of the bands in the surfactant-assisted samples. Also, the bandwidth of the peaks is changed. The observed band position of the samples GOE, GOEC1, GOEC2, GOEC3, GOET1, GOET2, and GOET3, are 538.19, 537.50, 539.49, 533.57, 539.32, 540.39, and 541.67 cm^{-1}, respectively. The change in band positions confirms the change in the interaction of capping agents on the surface of nanoparticles.

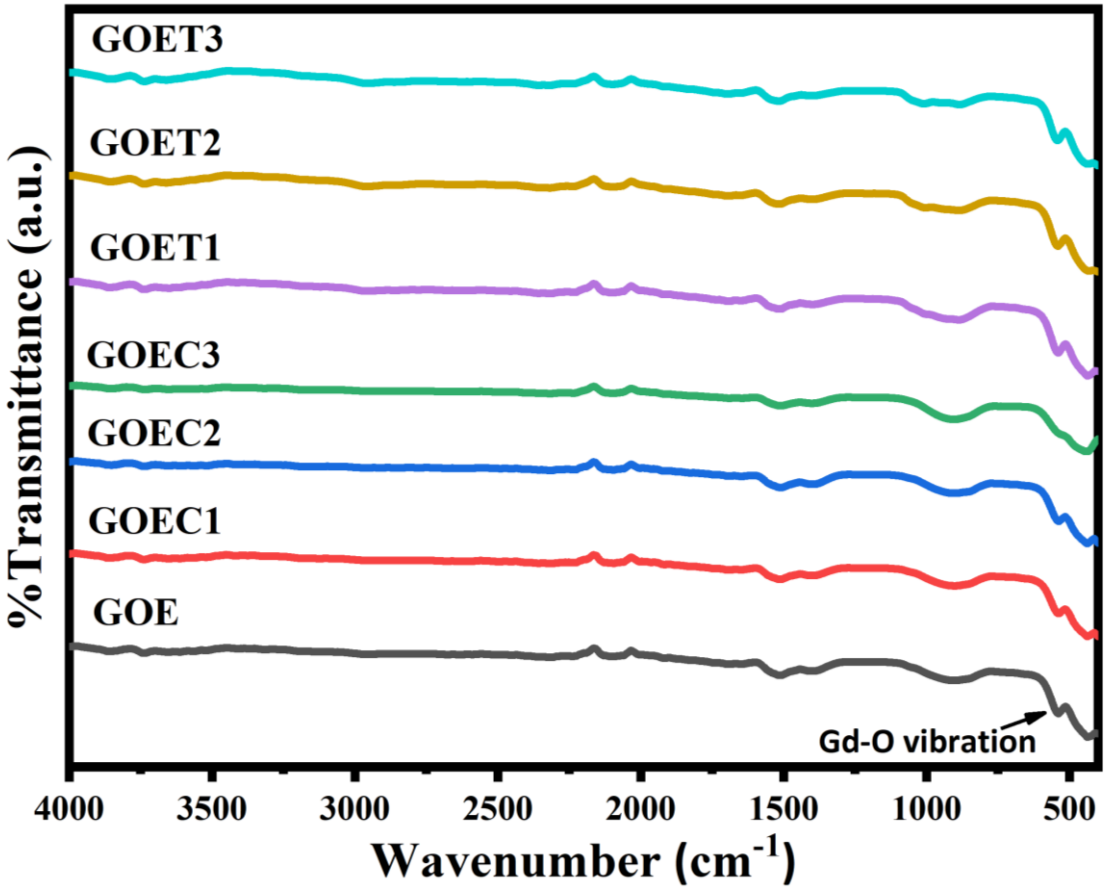

Figure 6.4: FTIR spectra of surfactant assisted/free Gd_2O_3:4mol%Eu phosphors.

6.5 UV-Vis Measurements

The UV-Visible absorbance spectra of the surfactant-free and assisted Gd_2O_3:4mol%Eu are shown in **Fig. 6.5**. All the samples exhibit maximum absorbance in the UV range. The bandgap (E_g) of all the samples is determined by using Tauc's formula, which is expressed following [33]:

$$\alpha (h\upsilon) = A (h\upsilon - E_g)^n \quad (6.1)$$

Here, in expression (6.1), hυ corresponds to the photon energy, A is a constant, α is the absorption coefficient, and the value of n is taken to be 2 [34–36]. A graph is plotted between $(\alpha h\upsilon)^2$ (along y-axis) versus E_g (in eV, along x-axis).

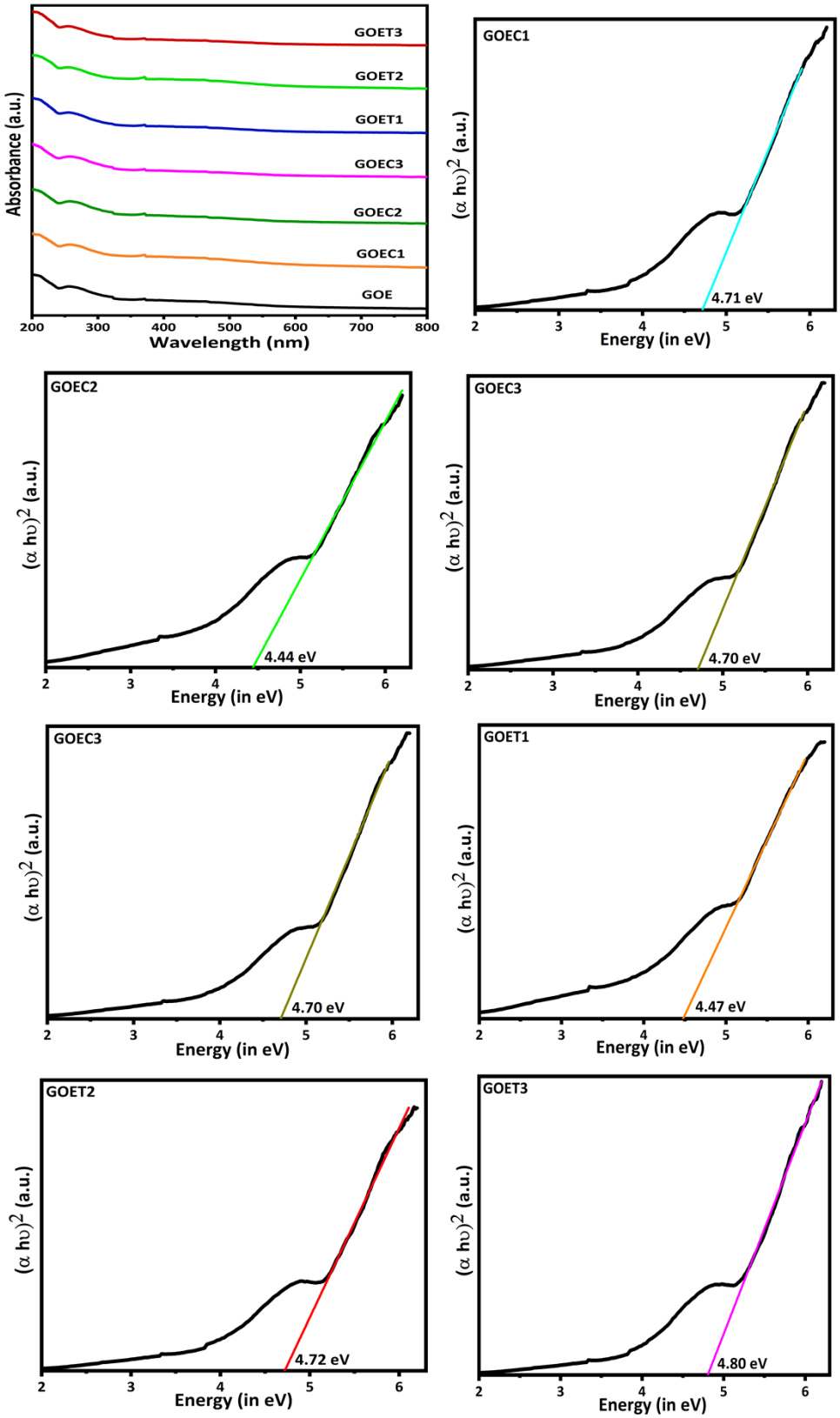

Figure 6.5: UV absorbance spectra and Tauc plots of surfactants assisted/free Gd_2O_3:4mol%Eu phosphors.

The bandgap is calculated by extrapolating the linear portion of the graph to the abscissa where, hυ = 0. The calculated values of the bandgap energies are 4.82, 4.71, 4.44, 4.70, 4.47,

4.72, and 4.80 eV for GOE, GOEC1, GOEC2, GOEC3, GOET1, GOET2, and GOET3, respectively. The variation in E_g can be related to the degree of structural order-disorder in the lattice, which leads to the change in the distribution of the energy levels within the bandgap. Moreover, bandgap depends on various factors such as type of surfactants, calcination temperature, holding time, etc. Thus, the bandgap values are decreased with the use of surfactants. This will lead to the variation in the luminescent intensity due to change in the oxygen density resulted from the use of surfactants [11,37,38].

6.6 Photoluminescence Studies

The excitation spectra of Gd_2O_3:Eu with and without surfactants in the different molar ratios are shown in **Fig. 6.6**.

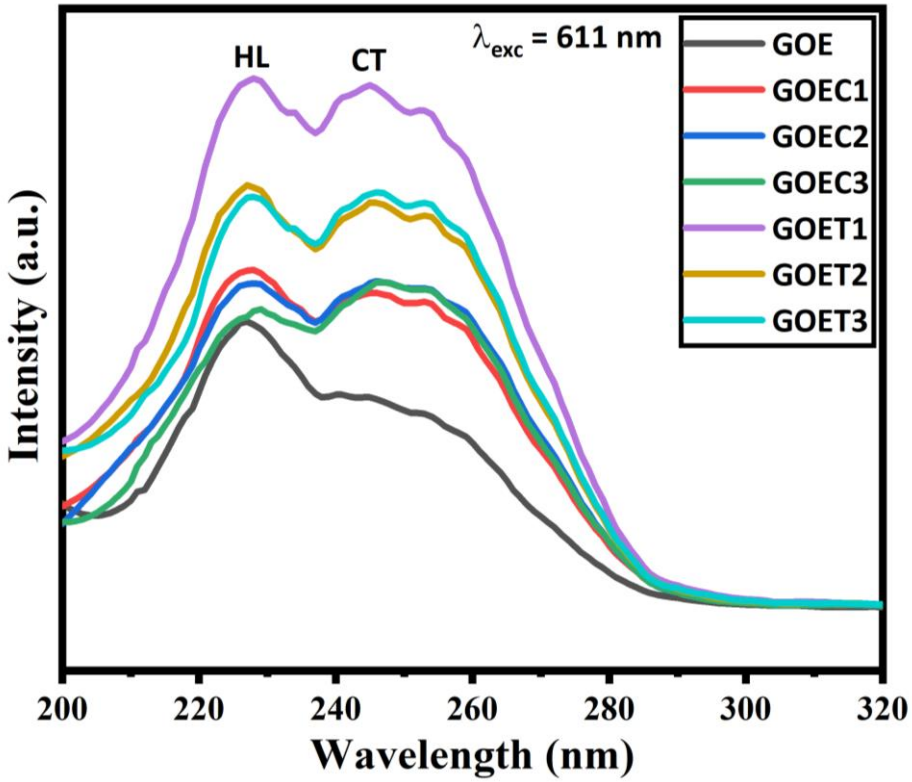

Figure 6.6: Excitation spectra of surfactant assisted/free Gd_2O_3:Eu samples.

All the spectra were recorded under the same emission wavelength λ_{emi}= 611 nm in the range of 200-320 nm. The peak around 250 nm is Eu-O charge transfer band. The band at 228 nm is the host transfer (HT) band, originated due to absorption of Gd_2O_3 host lattice [18,39]. The band shape of the HL and CT are the same for all the samples. However, the only change observed is in the intensity of the bands. It can be illustrated from the spectra that the intensity of the CT band is more for the surfactant assistant samples as compared to surfactant-free Gd_2O_3:Eu.

Fig. 6.7 (A) and **Fig. 6.7 (B)** represent the emission spectra of CTAB and TOPO assisted Gd_2O_3:4mol%Eu samples, respectively. The spectra were recorded under 250 nm UV excitation in 500-800 nm spectral range. The main peaks are observed at 595, 611, 625, 649, and 705 nm, respectively corresponding to the $^5D_0 \rightarrow ^7F_{1,2,3}$ transitions of Eu^{3+} ion [40–42].

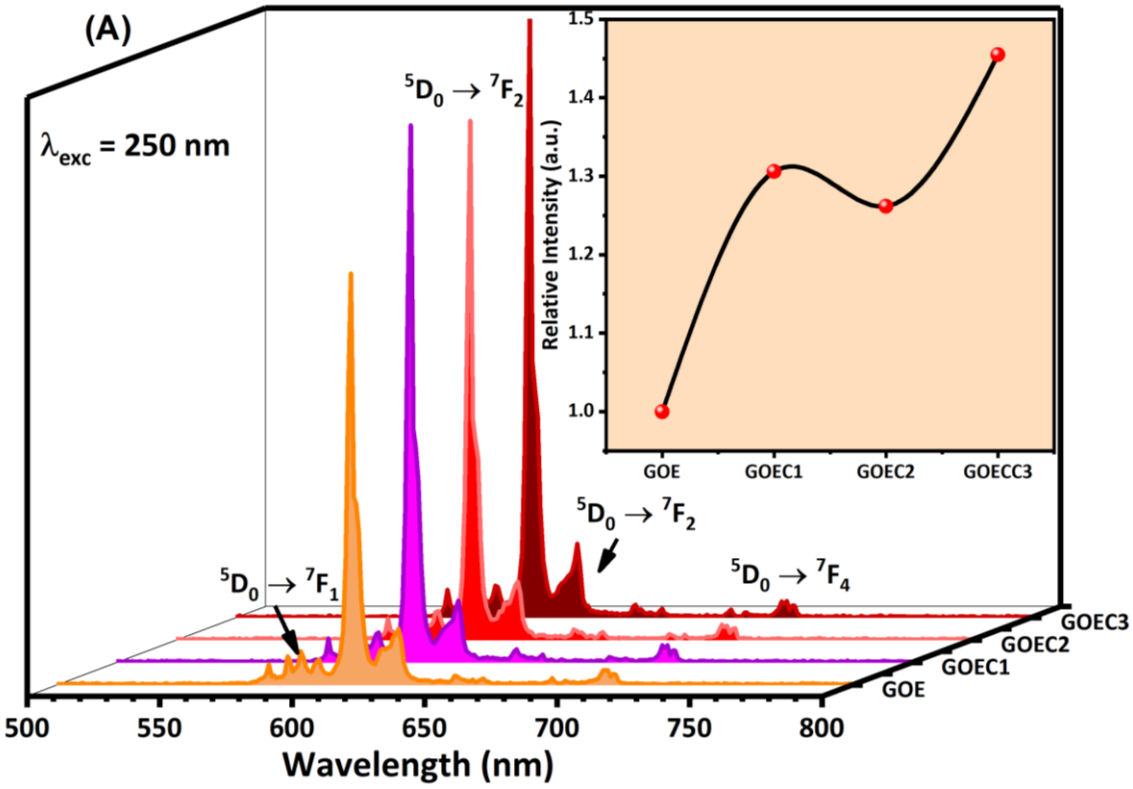

Figure 6.7 (A): PL emission spectra of CTAB assisted Gd_2O_3:4mol%Eu phosphors and inset showing the variation in the PL intensity.

The highly intense peak among the other peaks is observed at 611 nm. The nature of the emission peaks is same in all the samples prepared with and without surfactants. The peak appearing at 611 nm is forbidden electric dipole ($^5D_0 \rightarrow ^7F_2$) transition, which is hypersensitive to the local crystal field symmetry of europium ions in the host lattice. The transition $^5D_0 \rightarrow ^7F_1$ is magnetic dipole transition and insensitive to the local crystal field symmetry. It is a well-known fact that there are two crystal symmetry sites in the case of cubic Gd_2O_3 i.e., C_2 and S_6, respectively [43–45]. These are present in the ratio 3:1. C_2 site possesses non-inversion symmetry, while S_6 has inversion symmetry. When europium ions occupy C_2 sites, due to lack of symmetry, electric dipole transition $^5D_0 \rightarrow ^7F_2$ originates with selection rule $\Delta J = 2$. On the contrary, when europium ions occupy S_6 sites with inversion symmetry, magnetic dipole transition $^5D_0 \rightarrow ^7F_1$ with $\Delta J=1$ takes place.

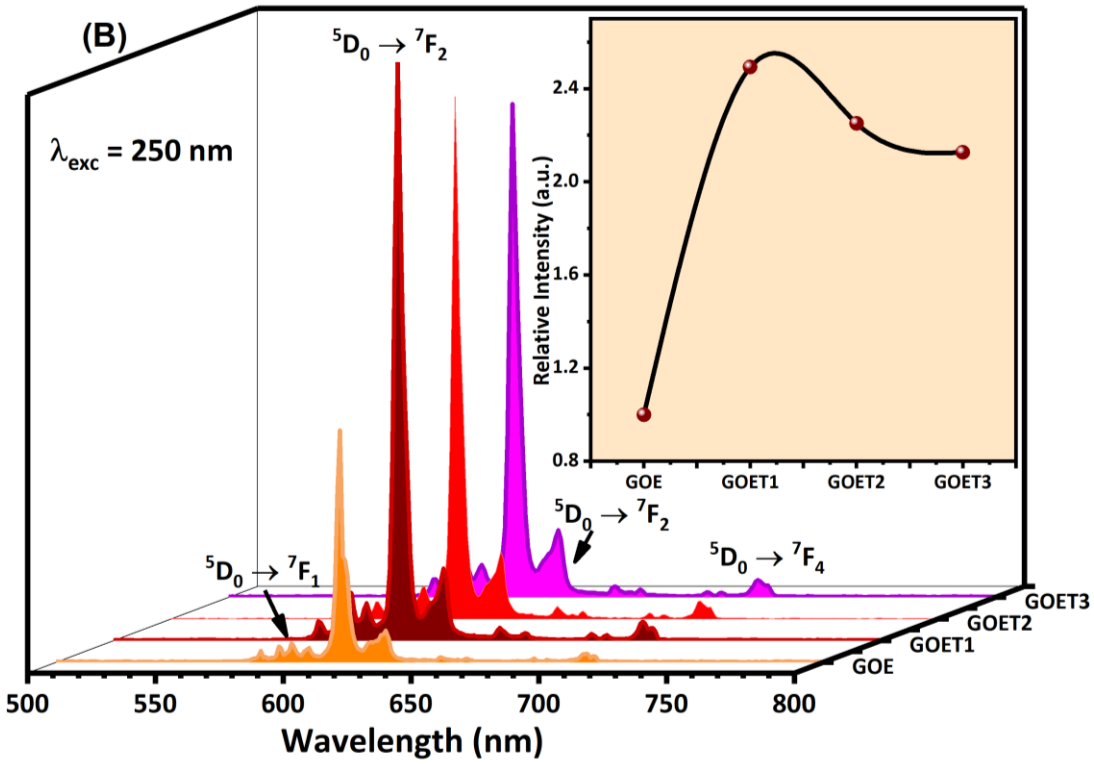

Figure 6.7 (B): PL emission spectra of TOPO assisted Gd_2O_3:4mol%Eu phosphors and inset showing the variation in the PL intensity.

It can be illustrated from **Fig. 6.7** (A-B) that emission intensity of samples synthesized with the use of surfactants is more than the surfactant-free samples. The maximum intensity in case of CTAB assisted samples is found for GOEC3 sample, while in the case of TOPO assisted samples, maximum intensity is found for GOET1 sample. The variations in intensity with the use of surfactants in different molar ratios are represented in the inset of **Fig. 6.7 (A-B)**. The variation in PL intensity is ascribed to the different morphologies, crystallinity and structural changes observed due to the use of different surfactants. The PL intensity is more for TOPO assisted samples when compared to CTAB assisted samples. In the present case, variation in the morphology with the use of surfactants in different molar ratios had remarkable effects on the emission intensity of Gd_2O_3:Eu phosphors. TOPO surfactant improved the morphology, crystallinity and degree of crystal structural order-disorder, thus resulted in higher PL intensity as compared to CTAB assisted samples. The use of surfactants decreased the surface defects, which decreased the non-radiative transitions and increased the radiative transitions [22,23]. Thus, the intensity of surfactant-assisted samples is enhanced as compared to bare samples.

The CIE coordinates of all the samples are calculated using CIE calculator MATLAB program {MATLAB 9.1 (version R2017b)}. The calculated CIE values are represented on the CIE diagram, as shown in **Fig. 6.8**.

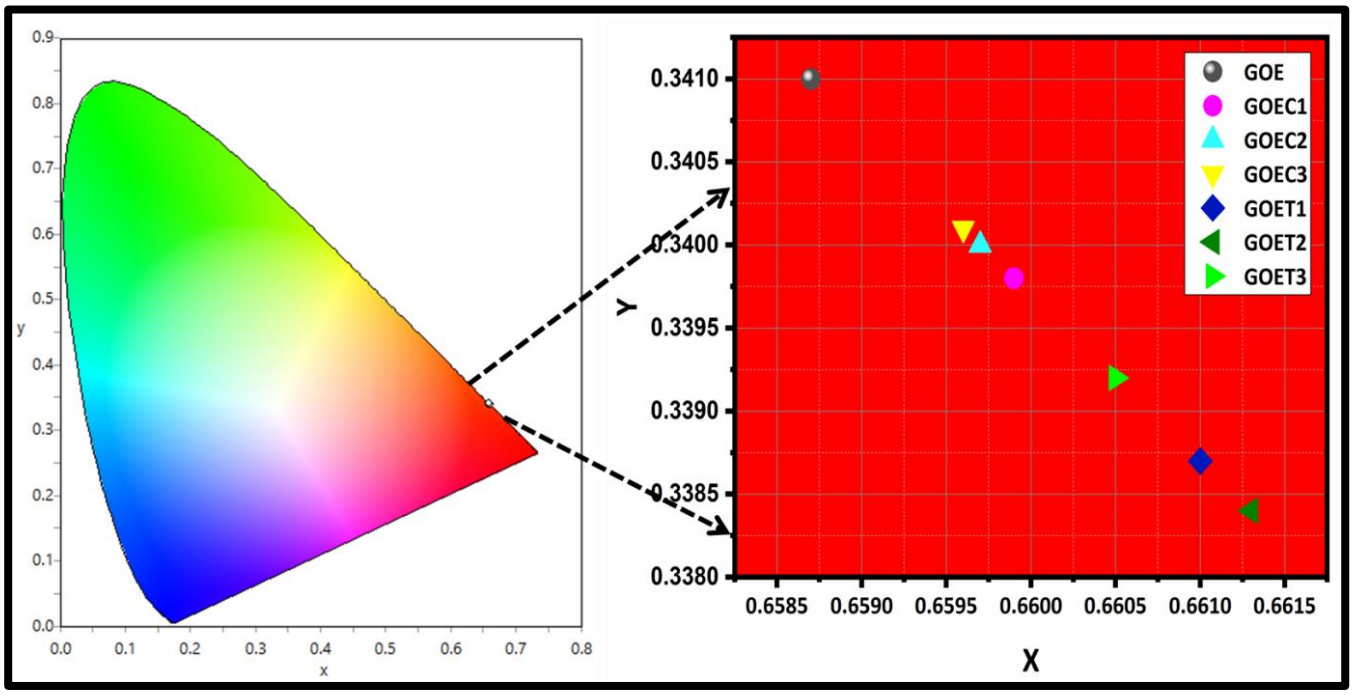

Figure 6.8: Chromaticity diagram of surfactant assisted/free Gd_2O_3:Eu phosphors.

The calculated CIE coordinates of all the samples are summarized in **Table 6.2**. It can be observed from **Table 6.2** that calculated CIE coordinates are close to the ideal red color coordinates (0.67, 0.33) standardized by NTSC [46]. The calculated CIE values also lie on the edge of the chromaticity diagram signifying the superior color purity of the sample and their potential to use for optoelectronic devices.

Table 6.2: CIE and CCT values of surfactant assisted/free Gd_2O_3:Eu phosphors.

Sample ID	Chromaticity coordinates		CCT values (K)
	x	y	
GOE	0.6587	0.3410	2952
GOEC1	0.6599	0.3398	3013
GOEC2	0.6597	0.3400	3002
GOEC3	0.6596	0.3401	2997
GOET1	0.6610	0.3387	3070
GOET2	0.6613	0.3384	3086
GOET3	0.6605	0.3392	3044

The CCT values are calculated by employing McCamy's empirical formula [47]. According to this formula:

$$\mathbf{CCT} = -473\ n^3 + 3601\ n^2 - 6861\ n + 5514.31 \qquad (6.2)$$

where, $n = (x-x_e)/(y-y_e)$ and (x_e, y_e) are the coordinates of the chromaticity epicenter.

CCT values of all the with and without surfactant assisted Gd_2O_3:4mol%Eu samples are calculated and enlisted in **Table 6.2**. CCT values of the phosphors lie in the range 2900-

3100 K. In general, CCT values less than 5000 K indicate warm light and are suitable for the fabrication of optoelectronic and display devices [48]. It is also observed that CIE and CCT values are more for TOPO assisted Gd_2O_3:4mol%Eu samples, indicating the better photometric parameters exhibited by these phosphors.

References

1 T. Justel, H. Nikol and C. Ronda, *Angew. Chem. Int. Ed.*, 1998, **37**, 3084–3103.

2 D. Singh and S. Kadyan, *J. Mater. Sci. Mater. Electron.*, 2017, **28**, 11142–11150.

3 J. G. Li, X. Li, X. Sun and T. Ishigaki, *J. Phys. Chem. C*, 2008, **112**, 11707–11716.

4 K. Lee, Y. Bae and S. Byeon, *Bull. Korean Chem. Soc*, 2008, **29**, 2161–2168.

5 E. M. Goldys, K. Drozdowicz-Tomsia, S. Jinjun, D. Dosev, I. M. Kennedy, S. Yatsunenko and M. Godlewski, *J. Am. Chem. Soc.*, 2006, **128**, 14498–14505.

6 B. Mutelet, P. Perriat, G. Ledoux, D. Amans, F. Lux, O. Tillement, C. Billotey, M. Janier, C. Villiers, R. Bazzi, S. Roux, G. Lu, Q. Gong and M. Martini, *J. Appl. Phys.*, 2011, **110**, 094317–094326.

7 S. Majeed and S. A. Shivashankar, *J. Mater. Chem. B*, 2014, **2**, 5585.

8 C. C. Lin, K. M. Lin and Y. Y. Li, *J. Lumin.*, 2007, **126**, 795–799.

9 N. Dhananjaya, H. Nagabhushana, B. M. Nagabhushana, B. Rudraswamy, C. Shivakumara, K. Narahari and R. P. S. Chakradhar, *Spectrochim. Acta - Part A Mol. Biomol. Spectrosc.*, 2012, **86**, 8–14.

10 D. Wawrzynczyk, M. Nyk, A. Bednarkiewicz, W. Strek and M. Samoc, *J. Nanoparticle Res.*, 2014, **16**, 2690–2703.

11 R. G. A. Kumar, S. Hata and K. G. Gopchandran, *Ceram. Int.*, 2013, **39**, 9125–9136.

12 X. Zhou and X. Wang, *Opt. - Int. J. Light Electron Opt.*, 2015, **126**, 4800–4803.

13 Y. Foo, A. Z. Abdullah, B. A. Horri and B. Salamatinia, *Ceram. intenational*, 2019, **45**, 9082–9091.

14 H. Lai, Y. Du, M. Zhao, K. Sun and L. Yang, *Mater. Sci. Eng. B*, 2014, **179**, 66–70.

15 X. Zhou and X. Wang, *Opt. - Int. J. Light Electron Opt.*, 2013, **124**, 1038–1040.

16 Y. Yang, X. Li, W. Feng, W. Yang, W. Li and C. Tao, *J. Alloys Compd.*, 2011, **509**, 845–848.

17 T. Prabhakaran, R. V Mangalaraja, J. C. Denardin and K. Varaprasad, *J. Mater. Sci. Mater. Electron.*, 2018, **29**, 11774–11782.

18 R. K. Tamrakar, D. P. Bisen and N. Brahme, *J. Radiat. Res. Appl. Sci.*, 2014, **7**, 550–559.

19 G. Liu, S. Zhang, X. Dong and J. Wang, *J. Nanomater.*, 2010, **2010**, 2–7.

20 R. Priya and O. P. Pandey, *Spectrochim. Acta Part A Mol. Biomol. Spectrosc.*, 2020, **231**, 118078.

21 Z. Xu, J. Yang, Z. Hou, C. Li, C. Zhang, S. Huang and J. Lin, *Mater. Res. Bull.*, 2009, **44**, 1850–1857.

22 G. S. R. Raju, E. Pavitra, G. P. Nagaraju, R. Kandimalla, B. F. El-Rayes and J. S. Yu, *Cryst. Growth Des.*, 2013, **2**, 4051–4058.

23 E. Pavitra, G. S. R. Raju and J. S. Yu, *Mater. Lett.*, 2015, **156**, 173–176.

24 A. P. Jadhav, A. Pawar, C. W. Kim, H. G. Cha, U. Pal and Y. S. Kang, *J. Phys. Chem. C*, 2009, **113**, 16652–16657.

25 N. Dhananjaya, H. Nagabhushana, S. C. Sharma, B. Rudraswamy, C. Shivakumara and B. M. Nagabhushana, *J. Alloys Compd.*, 2014, **587**, 755–762.

26 R. A. Mir, P. Sharma and O. P. Pandey, *Sci. Rep.*, 2017, **7**, 1–12.

27 M. Kabir, M. Ghahari and M. S. Afarani, *Ceram. intenational*, 2014, **40**, 10877–10885.
28 A. Aldalbahi, M. Rahaman and A. A. Ansari, *J. Sol-Gel Sci. Technol.*, 2019, **89**, 785–795.
29 D. Kumar, M. Sharma and O. P. Pandey, *J. Lumin.*, 2015, **158**, 268–274.
30 E. Odella, R. D. Falcone, M. Ceolin, J. J. Silber and N. M. Correa, *J. Phys. Chem. B*, 2018, **122**, 4366–4375.
31 R. Priya and O. P. Pandey, *Vacuum*, 2018, **156**, 283–290.
32 E. Hemmer, H. Takeshita, T. Yamano, T. Fujiki, Y. Kohl, K. Löw, N. Venkatachalam, H. Hyodo, H. Kishimoto and K. Soga, *J. Mater. Sci. Mater. Med.*, 2012, **23**, 2399–2412.
33 J. Tauc, R. Grigobovici and A. Vancu, *Phys. Stat. Sol.*, 1966, **15**, 627–637.
34 J. Li, Q. Zhu, X. Li, X. Sun and Y. Sakka, *Acta Mater.*, 2011, **59**, 3688–3696.
35 Q. Zhu, J.-G. Li, X. Li and X. Sun, *Curr. Nanosci.*, 2010, **6**, 496–504.
36 D. Xu, D. Haranath, H. He, S. Mishra, I. Bharti, D. Yadav, B. Sivaiah, B. Gahtori, N. Vijayan, A. Dhar, J. Zhu, V. Shanker and R. Pandey, *CrystEngComm*, 2014, **16**, 1652.
37 S. V. Motloung, F. B. Dejene, H. C. Swart and O. M. Ntwaeaborwa, *Ceram. Int.*, 2015, **41**, 6776–6783.
38 A. Kumar, D. Kumar and J. Manam, *J. Mater. Sci. Mater. Electron.*, 2018, **30**, 2360–2372.
39 G. Seeta Rama Raju, E. Pavitra, G. Nagaraju and J. S. Yu, *Dalt. Trans.*, 2015, **44**, 1790–1799.
40 S. Som, S. Dutta, V. Kumar, A. Pandey, V. Kumar, A. K. Kunti, J. Priya, S. K. Sharma, J. J. Terblans and H. C. Swart, *J. Alloys Compd.*, 2015, **622**, 1068–1073.
41 R. S. Ukare, G. D. Zade, B. Deva Prasad Raju and S. J. Dhoble, *Optik (Stuttg).*, 2016, **127**, 1871–1878.
42 M. Bettinelli, F. Piccinelli, A. Speghini, J. Ueda and S. Tanabe, *J. Lumin.*, 2012, **132**, 27–29.
43 Y. Liu, P. Yang, W. Wang, H. Dong and J. Lin, *CrystEngComm*, 2010, **12**, 3717–3723.
44 M. Jayasimhadri, B. V. Ratnam, K. Jang, H. S. Lee, B. Chen, S. S. Yi, J. H. Jeong and L. Rama Moorthy, *Int. J. Appl. Ceram. Technol.*, 2011, **8**, 709–717.
45 O. Meza, E. G. Villabona-Leal, L. A. Diaz-Torres, H. Desirena, J. L. Rodríguez-López and E. Pérez, *J. Phys. Chem. A*, 2014, **118**, 1390–1396.
46 S. Som, A. K. Kunti, V. Kumar, V. Kumar, S. Dutta, M. Chowdhury, S. K. Sharma, J. J. Terblans and H. C. Swart, *J. Appl. Phys.*, , DOI:10.1063/1.4876316.
47 C. S. McCamy, *Color Res. Appl.*, 1992, **17**, 142–144.
48 P. Kumari and J. Manam, *Spectrochim. Acta - Part A Mol. Biomol. Spectrosc.*, 2016, **152**, 109–118.

CHAPTER 7

RESULTS AND DISCUSSION IV

Overview

The morphology of the materials can be altered with the aid of different templates during synthesis. For this purpose, three water-soluble soft templates, such as Thioglycerol (TG), Dextran, and Polyvinylpyrrolidone (PVP) are used during the synthesis of phosphors. The amount of all the templates is varied from 1 to 2.5 wt% during synthesis. The influence of different templates on the structural, morphological, and optical characteristics of Gd_2O_3:4mol%Eu are studied in detail. The photometric parameters such as CIE coordinates and CCT values are determined to check their applicability for practical applications. In brief, the present chapter elucidates the efforts to engineer the morphology using different templates and their impact on the optical and luminescent properties of the phosphors.

7.1 Introduction

Inorganic phosphors have attracted more attention in the display and optoelectronic devices. Among the various phosphors, rare-earth oxides are suitable host lattices due to their physical and chemical stability, low phonon energy, and long lifetimes [1–5]. Like Y_2O_3, Gd_2O_3 is a sesquioxide rare-earth oxide and finds potential applications in flat panel displays, cathode ray tubes, field emission displays, biosensors, fluorescent lamps, etc. [6–9]. Among all the rare-earth dopants, Gd_2O_3 is an excellent host matrix for Eu^{3+} ions due to the similarity in the ionic radii. Gd_2O_3:Eu is a red light-emitting phosphor and emits sharp, narrow, and intense spectra under UV illumination [9,10].

The emission intensity of the phosphors depends on many factors such as shape, size, crystal structure, and presence of defects. The size, shape and dimensionality of the phosphors depend on the synthesis route to be followed. For this purpose, sol-gel, co-precipitation, hydrothermal, and combustion methods have been opted [11–14]. To engineer the morphological features, different templates and additives are used. These result in the formation of varying nano/micro-structures depending on the formation of micelle and forces of interactions. **Table 7.1** represents the morphology variation with different templates used during the synthesis of phosphors. It can be observed from **Table 7.1** that different templates result in the formation of different structures depending on their type and the synthesis route followed.

Table 7.1: Morphology of phosphors using different templates.

Authors' name	Phosphor	Synthesis method	Template	Morphology	Ref.
Xu *et al.*	$Y_2O_3:Ln^{3+}$ (Ln^{3+}= Eu^{3+}, Tb^{3+})	Urea assisted Co-precipitation method	Polystyrene	Hollow microspheres	[15]
Kumar *et al.*	$Y_2O_3:Tb^{3+}$	Co-precipitation method	TG and PVP	Spheres	[16]
Vidya *et al.*	Gd_2O_3:Eu	Combustion method	E. tirucalli	Nanoplates and rose like nanoflowers	[17]
Jeet and Pandey	BAM:Eu^{2+}	Combustion method	Thioglycerol and β-cyclodextrin	Rods and plates	[18]
Pavitra and Xu	Gd_2O_3:Eu	Wet chemical route	Polyethylene glycol (PEG)	Nanoflowers	[19]
Zhai *et al.*	$ZnWO_4$:Sm	Hydrothermal method	PEG	Irregular size particles	[20]
Venkataravanappa *et al.*	Sr_2SiO_4:Eu	Ultrasound method	AV gel (bio-template)	Super Hierarchical Structures	[21]
Wu *et al.*	Eu_2O_3	Sol-gel method	PAA	Nanotubes	[22]
Venkataravanappa *et al.*	Ca_2SiO_4:Eu	Ultrasound method	EGCG	Spheres	[23]

Till date, no investigations on the morphological variation of Gd_2O_3:Eu phosphors using PVP, TG, and Dextran as sacrificial templates are reported. In the present chapter, effect of water-soluble templates on the structural, morphological, optical, and luminescent properties

of Gd_2O_3:Eu phosphors are studied. The concentration of the europium ions is fixed as 4 mol% in the host lattice to study the effect of templates only. The varying amounts (0.5 to 2.5 wt%) of TG, PVP, and Dextran polymers are used during the synthesis. All the samples are synthesized using co-precipitation route. The synthesis details of these templates (PVP, Dextran and TG) assisted/free Gd_2O_3:4mol%Eu samples, are already given in ***Chapter 3*** (**Table 3.1**). However, for simplicity, sample labels and synthesis conditions are given in **Table 7.2**.

Table 7.2: Sample labels and synthesis conditions for template (TG, Dextran, and PVP) assisted/free Gd_2O_3:4mol%Eu phosphors.

S. No.	Template used	Amount of Template (in wt%)	Calcination Temperature (°C)	Sample ID
1.	-	-	1000	GE4
2.	Dextran	0.5, 1.0, 1.5, 2.0, 2.5	1000	D0.5, D1, D1.5, D2, D2.5
3.	PVP	0.5, 1.0, 1.5, 2.0, 2.5	1000	PVP0.5, PVP1, PVP1.5, PVP2, PVP2.5
4.	TG	0.5, 1.0, 1.5, 2.0, 2.5	1000	TG0.5, TG1, TG1.5, TG2, TG2.5

7.2 XRD Study

To study the influence of the templates (PVP, Dextran and TG) on the crystal structure, phase purity, and crystallinity; XRD patterns of all the samples are recorded. **Fig. 7.1 (A-C)** shows the XRD patterns of the Gd_2O_3:4mol%Eu phosphors synthesized using PVP, Dextran, and TG templates, respectively. XRD patterns of all the samples are well indexed with standard International center for diffraction data (ICDD) card number 03-065-3181, indicating the formation of single phase pure cubic Gd_2O_3 with $Ia\bar{3}$ group symmetry. However, in the case of TG-assisted Gd_2O_3:4mol%Eu samples, small peaks of low intensity are observed corresponding to the monoclinic phase of Gd_2O_3, matching with the ICDD card number 00-043-1015 as shown in **Fig. 7.1 (C)**. The sharp and distinct XRD patterns represent the crystalline nature of the synthesized samples. It is observed that the crystalline nature is more in case of PVP-assisted Gd_2O_3:4mol%Eu samples and least in the case of TG assisted samples. No other impure phase(s) corresponding to the initial precursors are observed in the XRD patterns, indicating the formation of the Gd_2O_3 phase only.

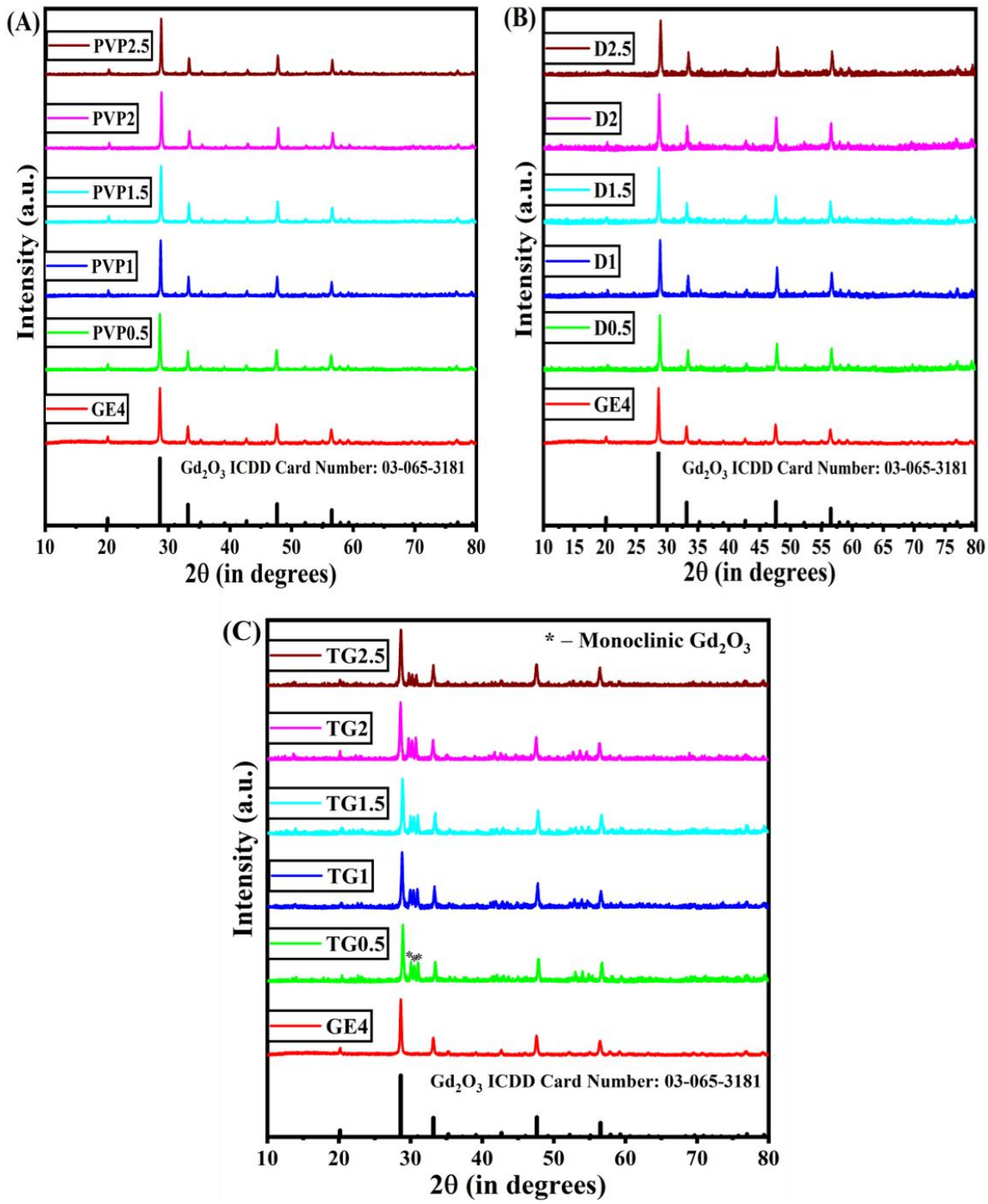

Figure 7.1: XRD patterns of (A) PVP, (B) Dextran and (C) TG assisted Gd_2O_3:4mol%Eu phosphors.

The average crystallite size (D) is calculated with respect to the most intense peak corresponding to the (222) plane using Scherrer's criterion [24].

$$\mathbf{D} = \frac{0.9\,\lambda}{\beta\,cos\theta} \tag{7.1}$$

$$\text{where, } \boldsymbol{\beta}=\sqrt{\beta^2_{observed} - \beta^2_{instrumental}} \quad (7.2)$$

The unit cell parameter (a) is determined using the following expression:

$$4\, a^2 \sin^2\theta = \lambda^2 (h^2+k^2+l^2) \quad (7.3)$$

where, the term symbols have their usual meaning.

The full width at half maxima (FWHM), average crystallite size, and lattice parameter (a) of all the samples are determined and summarized in **Table 7.3**. It can be seen from **Table 7.3** that in case of PVP-assisted Gd_2O_3:4mol%Eu samples, average crystallite size increases with the increasing amount of PVP. However, in the case of TG and Dextran assisted Gd_2O_3:4mol%Eu samples, average crystallite size does not follow any trend. It decreases or increases with different amounts of templates used during synthesis. The variation is observed because of the different stearic stabilization offered by the templates during synthesis.

Table 7.3: Structural parameters of template assisted/free Gd_2O_3:4mol%Eu phosphors.

Sample ID	Plane	2θ (in degrees)	FWHM (in degree)	Crystallite size (nm)	Lattice parameter (Å)
GE4	(222)	28.637	0.2022	40.52	10.785
PVP0.5	(222)	28.634	0.1745	46.96	10.786
PVP1	(222)	28.744	0.1586	51.67	10.746
PVP1.5	(222)	28.804	0.1627	50.36	10.724
PVP2	(222)	28.883	0.1512	54.22	10.695
PVP2.5	(222)	28.379	0.1493	54.86	10.881
D0.5	(222)	28.854	0.1869	43.85	10.705
D1	(222)	28.895	0.1926	42.57	10.690
D1.5	(222)	28.696	0.2074	39.51	10.763
D2	(222)	28.757	0.2174	37.70	10.741
D2.5	(222)	28.970	0.2405	34.08	10.664
TG0.5	(222)	28.916	0.1879	43.63	10.683
TG1	(222)	28.806	0.2006	40.85	10.723
TG1.5	(222)	28.876	0.2159	37.97	10.697
TG2	(222)	28.595	0.2254	36.35	10.800
TG2.5	(222)	28.644	0.2491	32.89	10.782

7.3 Morphological Studies

The effect of the templates (PVP, Dextran, and TG) on the morphological features of Gd_2O_3:4mol%Eu samples are studied using field emission electron spectroscopy. The recorded micrographs of the template (PVP, Dextran, and TG) assisted/free Gd_2O_3:4mol%Eu samples are shown in **Fig. 7.2 (A-I)**. **Fig. 7.2 (A)** represents the micrograph of the GE4 sample, synthesized without any template. The sample consists of nanorods with length in the range

500-700 nm and diameter in the range 100-150 nm. The addition of the templates resulted in the variation in the morphology and agglomeration in the synthesized samples.

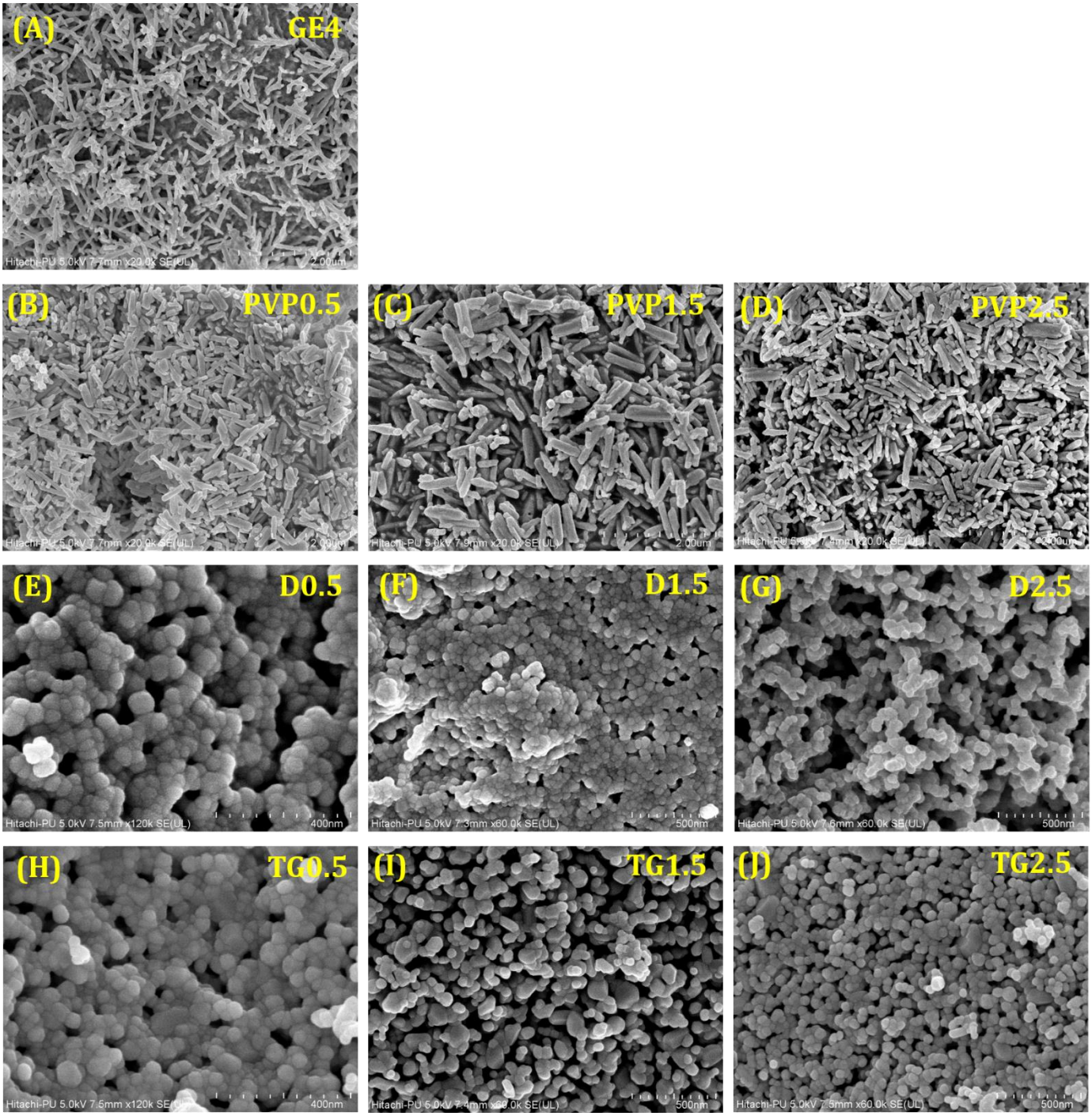

Figure 7.2 (A-J): FESEM micrographs of template (PVP, Dextran, and TG) assisted/free Gd_2O_3:4mol%Eu phosphors.

The samples which are synthesized using PVP also exhibit rod-like morphology, as shown in **Fig. 7.2 (B-D)**. However, with increasing PVP amount, length of the rods decreases, and diameter increases. Moreover, the extent of monodispersity increases with increasing PVP amount because of the stearic hindrance offered by the PVP ligands. PVP ligands have long

alkali chains and act as capping agents. These alkali chains get attached to the surface of the particles and offer stearic repulsive force. This stearic hindrance results in the better dispersion of the particles in the solution by balancing the surface tension [25]. Thus, monodisperse particles are observed in PVP assisted Gd_2O_3:4mol%Eu samples. The intensity of the XRD peaks also reflected the better crystallinity in the case of PVP assisted Gd_2O_3:4mol%Eu samples. Better crystallinity, less agglomeration and uniform morphology are the favorable conditions to exhibit better luminescent properties.

Fig. 7.2 (E-G) represents the micrographs of the Gd_2O_3:4mol%Eu samples synthesized using Dextran. It can be observed from the micrographs that for the lower concentration of Dextran, the rod-like morphology of the phosphors is vanished and transformed to quasi-spherical or hexagonal-shaped particles. The extent of the agglomeration is also increased with increasing dextran concentration. Moreover, pores are also observed in these samples. Dextran is a polysaccharide, consists of D-glucose with alpha-1,6-linkages. The chain-like structure of the Dextran combines with the hydroxide nanocrystals anisotropically as building blocks. The reductive aldehyde groups of Dextran are exploited in-situ for nucleation of monodisperse metallic clusters. During synthesis, Dextran undergoes hydrolysis with condensation reactions and forms long chains. The in-situ reduction of aldehydic groups results in the formation of porous structures [26,27]. **Fig. 7.2 (H-J)** represents the micrographs of Gd_2O_3:4mol%Eu samples synthesized using TG template. In these samples, rod-like morphology has disappeared for even low concentration of TG and transformed completely into semi-spherical and hexagonal shaped particles. The extent of agglomeration is observed for a high amount of TG used during synthesis. Thioglycerol is also a capping agent, and it has large coordination numbers (4, 5, and 6). The thiol (-SH) group in TG molecules provides chelating complexes with Gd^{3+}. The surface of the particle is covered by the carboxyl groups, and this controls the shape and size of the particles [28]. Thus, hexagonal or quasi-spherical particles are observed. The porous structures formed with the use of TG and Dextran templates have potential applications in biomedical applications for drug loading, delivery, and targeting.

7.4 Fourier Transform Infrared (FTIR) Analysis

Fig. 7.3 (A-C) represents the FTIR spectra of the samples recorded in the range 400-4000 cm^{-1}. It is observed that FTIR spectra consist of bands around 475 and 546 cm^{-1}, which are attributed to the Gd-O vibrations [29]. In template (PVP, Dextran and TG) assisted Gd_2O_3:4mol%Eu samples, the peak around 546 cm^{-1} is either blue or red shifted. The possible

reason for this shifting is variation in the lattice parameters of all the samples. The weak band around 1523 cm^{-1} in all the samples is due to the C-O stretching vibration [30].

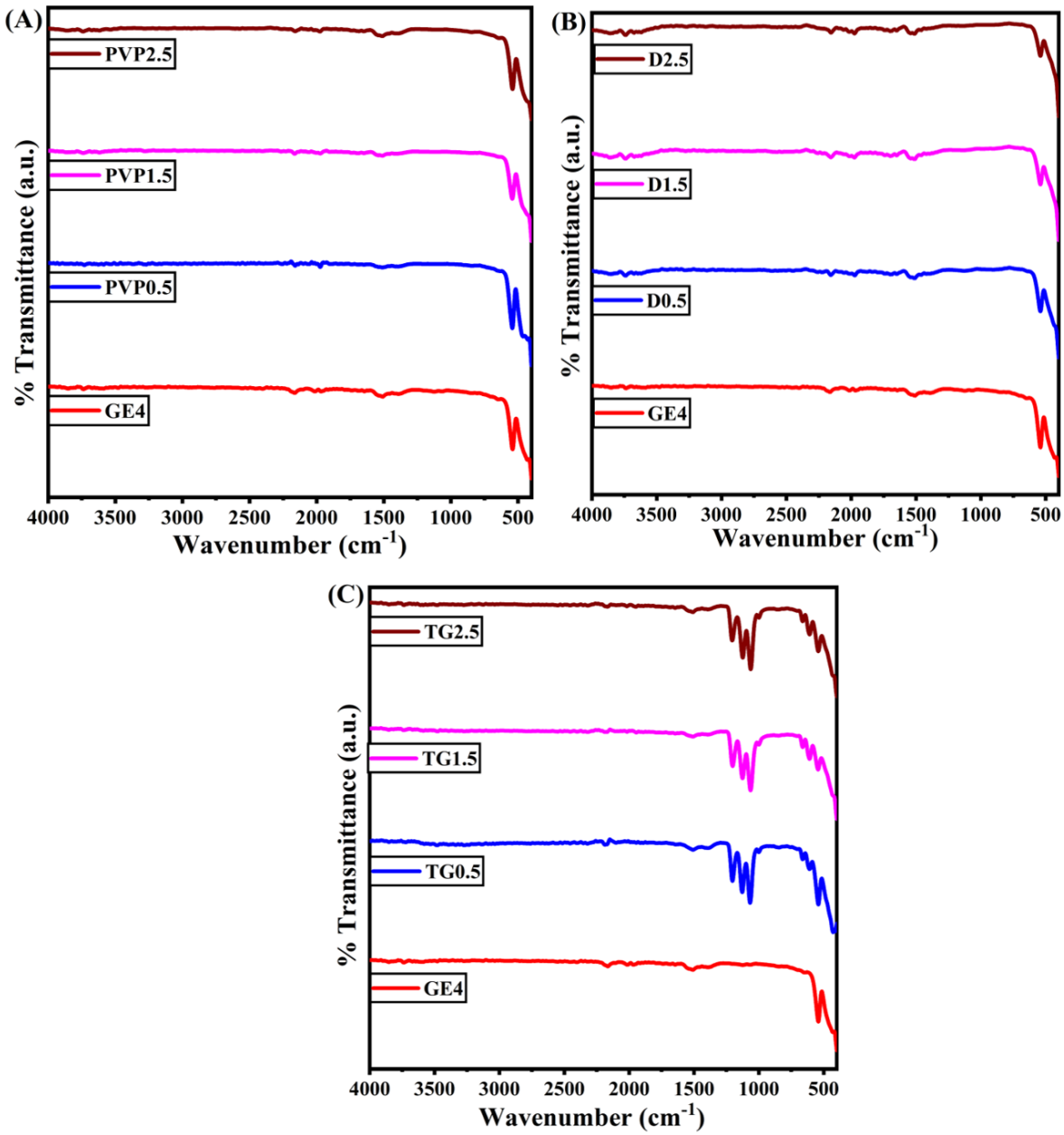

Figure 7.3 (A-C): FTIR spectra of template assisted/free Gd_2O_3:4mol%Eu phosphors.

It is interesting to observe that the characteristic peaks due to PVP and Dextran are not observed in the FTIR spectra. However, in the case of TG assisted Gd_2O_3:4mol%Eu samples, many other peaks are observed. The peak around 662 cm^{-1} observed in TG samples is due to C-S vibration [28]. The characteristic peaks of TG, i.e., peak at 2555 cm^{-1} corresponding to the S-H vibration, is found to be absent. This represents the deprotonation of the TG molecule and attachment to the surface of Gd_2O_3 surface. The other peaks are observed around 1066, 1125, and 1202 cm^{-1}. These bands are attributed to the C=O symmetric stretching vibrations [31,32]. Moreover, the peak around 609 cm^{-1}, corresponding to Gd-O vibration, is observed only in the

case of TG assisted Gd_2O_3:4mol%Eu samples [33]. This peak might be evolved due to the presence of minor monoclinic-Gd_2O_3 phase. This result is highly consistent with XRD results, where low-intensity peaks of monoclinic Gd_2O_3 are observed in the case of TG directed samples.

7.5 UV-Vis Measurements

Fig. 7.4 (A-C) represents the UV-Vis absorbance spectra of template (PVP, Dextran and TG) directed/free Gd_2O_3:4mol%Eu samples recorded in the range of 200-800 nm.

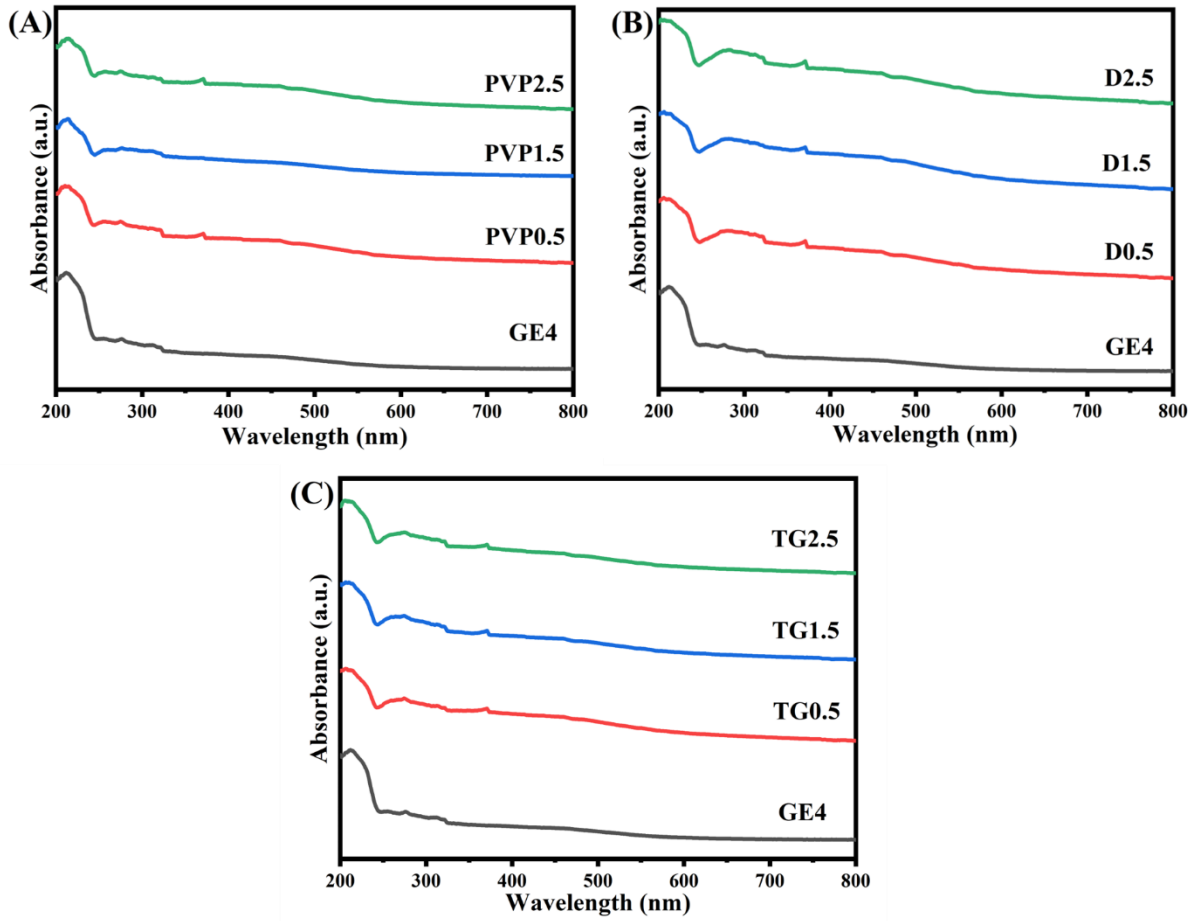

Figure 7.4 (A-C): Absorbance spectra of template assisted/free Gd_2O_3:4mol%Eu phosphors.

All the samples exhibit maximum absorption in the UV region. The optical bandgap (E_g) of the samples is determined using Tauc's equation, as follows [34]:

$$(\alpha h\nu) = A\,(h\nu - E_g)^n \qquad (7.3)$$

where, A is a constant, h is Planck's constant, α is absorption coefficient, ν is frequency, and value of the n depends on the type of transition. The value of E_g is determined by extrapolating the linear portion of the graph (plotted between $(\alpha h\nu)^2$ along the y-axis and hν along the x-axis), where $(\alpha h\nu)^2=0$. The Tauc plots of different template assisted/free

Gd_2O_3:4mol%Eu samples are shown in **Fig. 7.5 (A-C)**. The calculated bandgap values are given in **Table 7.4**.

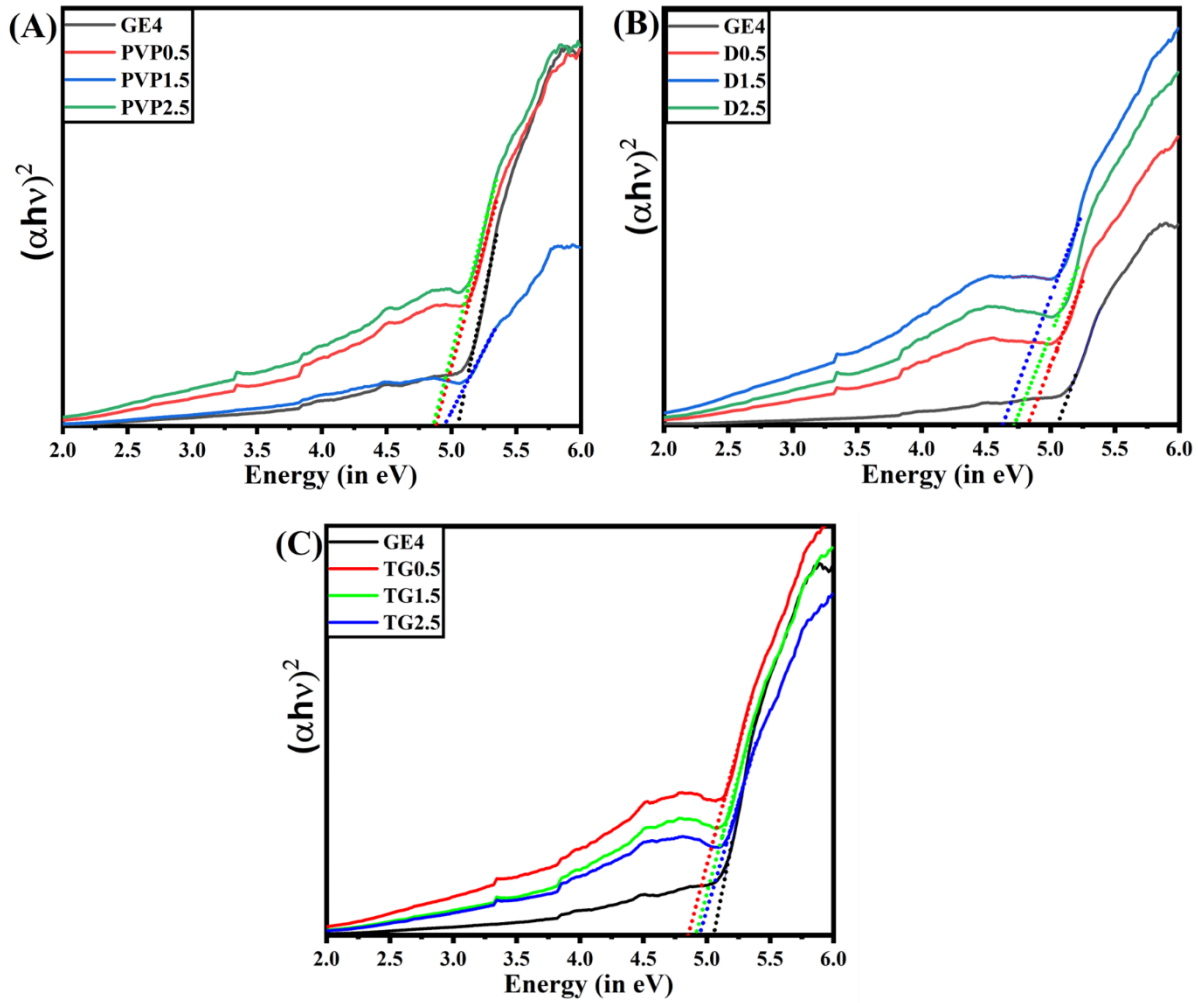

Figure 7.5 (A-C): Tauc plots of template assisted/free Gd_2O_3:4mol%Eu phosphors.

It can be observed from **Table 7.4** that bandgap values for the template assisted Gd_2O_3:4mol%Eu samples are less than the bare one (GE4). The variation in bandgap is attributed to the degree of structural order-disorder in the lattice. This results in variation in the intermediate energy level distribution within the bandgap. Moreover, bandgap variation is also related to the type of morphology, crystallite size, and type of defects present in the lattice. The narrowing of the bandgap is also associated with the presence of existing oxygen vacancies.

Table 7.4: Calculated bandgap values of template assisted/free Gd_2O_3:4mol%Eu phosphors.

Sample ID	**GE4**	**PVP0.5**	**PVP1.5**	**PVP2.5**	**D0.5**	**D1.5**	**D2.5**	**TG0.5**	**TG1.5**	**TG2.5**
Bandgap (eV)	5.05	4.94	4.88	4.86	4.82	4.72	4.63	4.94	4.92	4.85

7.6 Photoluminescence Studies

Fig. 7.6 represents the PL excitation spectra of template assisted/free Gd_2O_3:4mol%Eu phosphors recorded at 611 nm. The excitation spectra consist of broadband ranging from 200

to 300 nm. This band consists of several peaks. The band around 220 nm is HAB, and the band centered around 250 nm is CT band [35]. The excitation peaks around 275, 309, and 311 are due to the transitions of Gd^{3+} ions, respectively [36]. The occurrence of these peaks indicates the efficient energy transfer from the host to activator ions. The shape of PVP and Dextran assisted templates are identical to that of Gd_2O_3:4mol%Eu, except for small shifts in the position and intensity of the peaks.

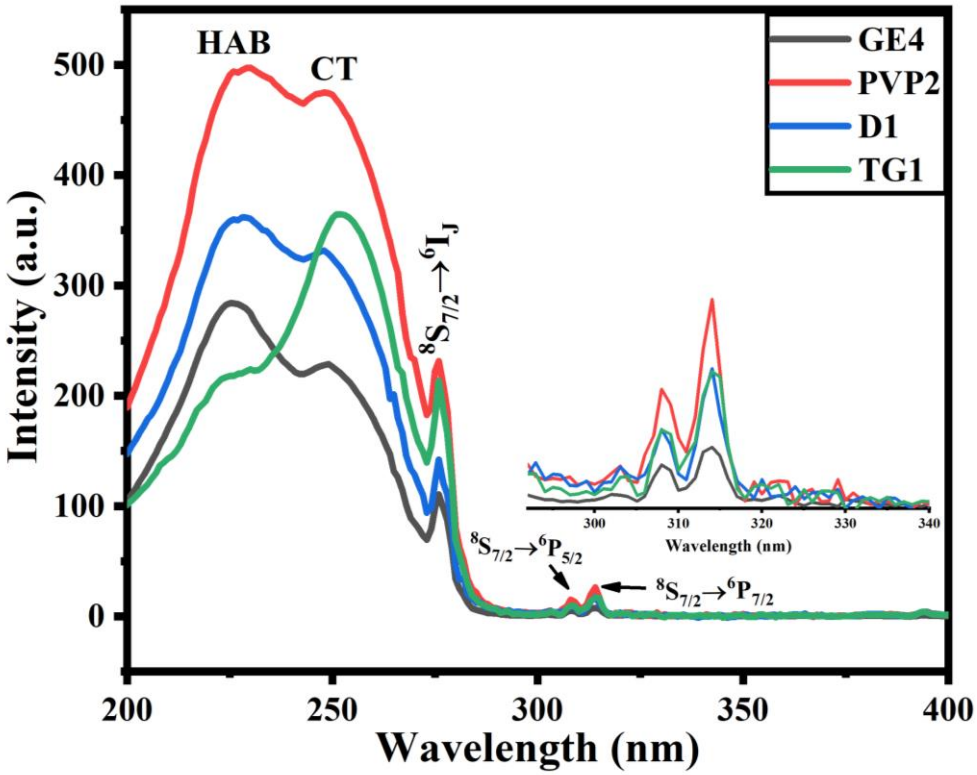

Figure 7.6: Excitation spectra of template assisted/free Gd_2O_3:4mol%Eu phosphors.

This is because of variation in the crystal structure parameters, which lead to change in the surrounding conditions of metal-ligand bond. However, the shape of the excitation spectra for TG assisted samples is different as compared to the other samples. This has arisen due to the presence of another phase, which leads to change in the spectral properties. Another observation from the excitation spectra is that HAB and CT bands for the template (PVP, Dextran and TG) assisted Gd_2O_3:4mol%Eu samples are red shifted. The positions of the HAB are 225, 227, 229, 225.5 nm and for CT are 248.8, 248.02, 248.79, and 251.9 nm for GE4, D1, PVP2, and TG1, respectively. The red shifting in these bands is observed due to the increase in the crystallite size as observed in XRD results and different morphologies of the samples.

PL emission spectra for all the samples are recorded under excitation at 250 nm in the range 500-800 nm, as shown in **Fig. 7.7 (A-C)**. It can be seen from emission spectra that all the samples exhibit sharp emission peaks around 590, 611, 625, 650, and 704 nm [8,9,37]. The

position and shape of the peaks are found to be identical except for the variation in the intensity. Among all the emission peaks, the peak around 611 nm is found to be the most intense one. This transition is hypersensitive forced electric dipole transition.

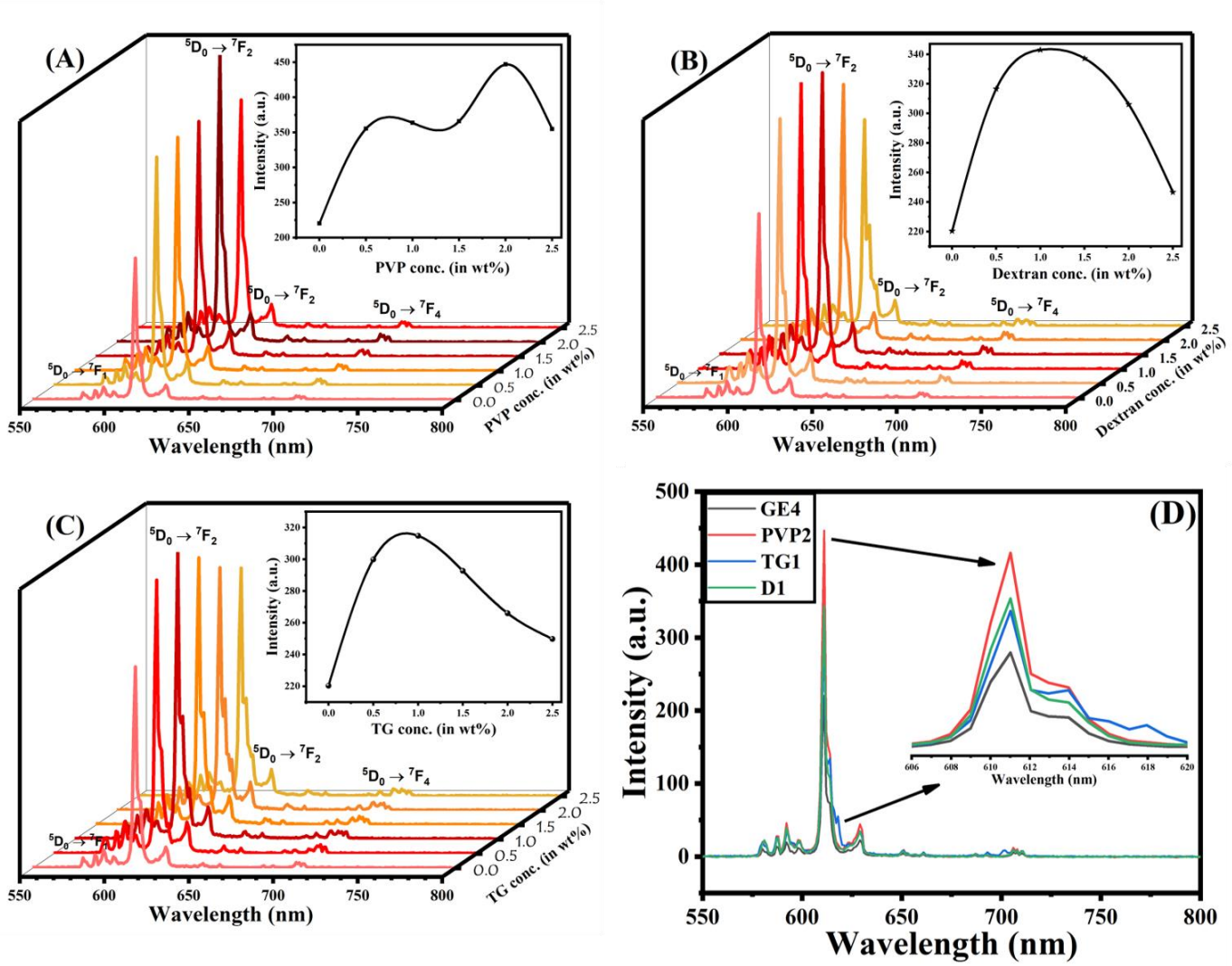

Figure 7.7: PL emission spectra of (A) PVP, (B) Dextran, and (C) TG assisted Gd_2O_3:4mol%Eu phosphors. The inset of the figures is representing the variation in the PL intensity with varying template concentration. (D) Comparison of emission intensity of template assisted/free Gd_2O_3:4mol%Eu phosphors.

Cubic-Gd_2O_3 has two crystallographic sites with six-fold coordination symmetry, i.e. C_2 (inversion symmetry) and S_6 (non-inversion symmetry). These sites are present in the ratio 3:1. If the europium ions occupy C_2 symmetry site, $^5D_0$-$^7F_2$ transition dominates, and if they occupy S_6 sites, then $^5D_0$-$^7F_1$ transition takes place. However, in the case of monoclinic-Gd_2O_3, there are three A, B, and C sites, all are having C_s symmetry [38]. It can be seen from emission spectra that the peak corresponding to the $^5D_0$-$^7F_2$ transition can be deconvoluted into two peaks for GE4, PVP and Dextran assisted samples. However, this peak can be deconvoluted into three peaks for TG assisted Gd_2O_3:4mol%Eu phosphors. The difference in the shape of this peak

represents the occupancy of europium ions at different sites in the host lattice and on the extent of crystal field splitting. The amount of the templates (PVP, Dextran, and TG) is varied from 1 to 5 wt% during synthesis. The different templates resulted in different morphologies of the phosphors. The maximum PL intensity for PVP, TG, and Dextran assisted Gd_2O_3:4mol%Eu samples are observed for 2, 1, and 1 wt%, respectively, as shown in insets of **Fig. 7.7 (A-C)**. The comparison of PL emission intensity in optimized samples is shown in **Fig. 7.7 (D)**. The variation in the PL intensity is attributed to several factors, such as variation in the crystallite size, morphology, and crystal structure. Among all the samples, PVP assisted Gd_2O_3:4mol%Eu samples exhibited maximum PL intensity. This is owing to the mono-dispersity, less agglomeration, and formation of pure cubic- Gd_2O_3 phase. However, in the case of TG assisted Gd_2O_3:4mol%Eu samples, PL intensity is found to be minimum. The plausible reason for this analogous behavior is the presence of minor monoclinic-Gd_2O_3 phase along with cubic-Gd_2O_3 phase. The different phases of the same host lattice result in the different occupancies of the europium ions, which leads to energy distribution via various channels and enhance the chances of non-radiative transitions. Thus, PL intensity is found to be minimum in TG assisted Gd_2O_3:4mol%Eu. This result is consistent with existing reports in the literature that PL intensity is less in case of monoclinic-Gd_2O_3:Eu as compared to cubic- Gd_2O_3:Eu [38]. In the present case, the fraction of the monoclinic-Gd_2O_3 phase is less, so its effect is less.

The photometric parameters such as CIE coordinates and CCT values of all the samples are calculated from the emission spectra to know the quality of the synthesized phosphors for device applications. CIE coordinates of the samples are determined using the CIE calculator through standard MATLAB program {MATLAB 9.1 (version R2017B)}. The calculated values of the CIE coordinates are summarized in **Table 7.5**. CIE coordinates lie in the red region which is close to the values of ideal red coordinates (0.67, 0.33), as standardized by the National Television Standard Committee (NTSC). The calculated values of the CIE coordinates are represented on the CIE diagram and shown in **Fig. 7.8**. Moreover, CIE values lie on the edge of the chromaticity diagram, which illustrates high color purity of the synthesized samples. CCT values are determined using McCamy's empirical formula [39]:

$$\mathbf{CCT} = -473\, n^3 + 3601\, n^2 - 6861\, n + 5514.31 \qquad (7.4)$$

where, $n = (x-x_e)/(y-y_e)$ and (x_e, y_e) are the coordinates of chromaticity epicenter.

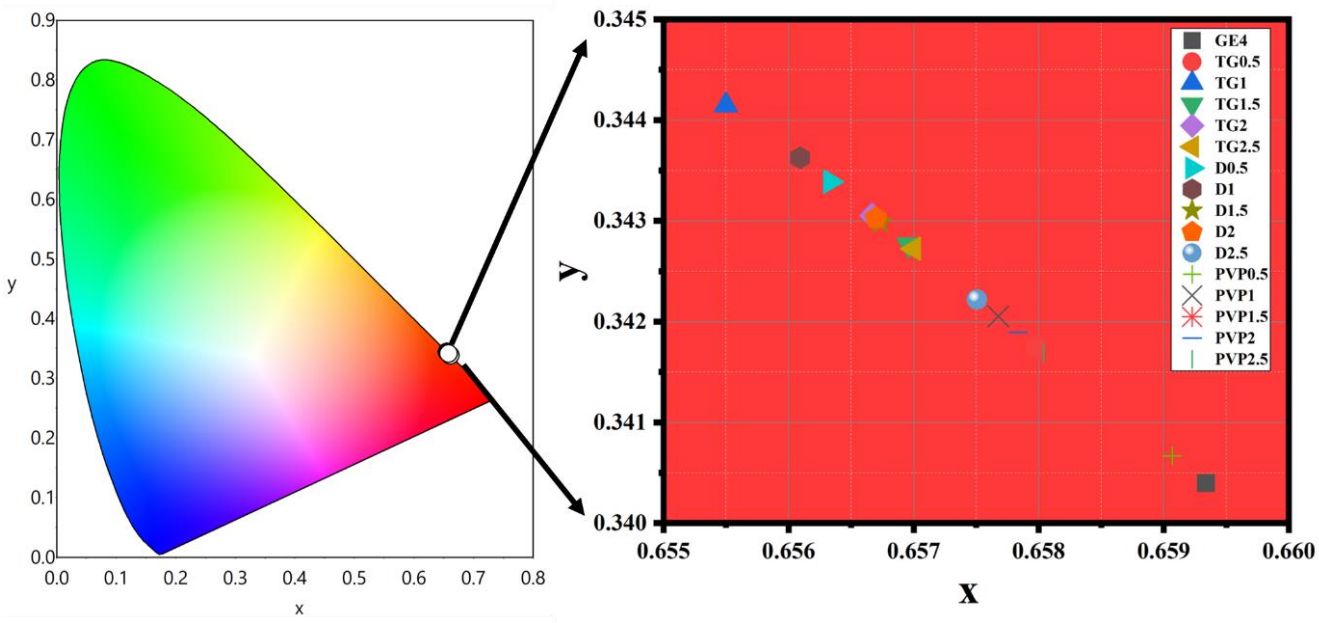

Figure 7.8: CIE diagram of template assisted/free Gd_2O_3:4mol%Eu phosphors.

Table 7.5: CIE and CCT values of template assisted/free Gd_2O_3:4mol%Eu phosphors.

Sample ID	CIE coordinates		CCT values (K)
	x	y	
GE4	0.6593	0.3404	2983
PVP0.5	0.6591	0.3407	2969
PVP1	0.6577	0.3420	2901
PVP1.5	0.6609	0.3389	3062
PVP2	0.6578	0.3419	2908
PVP2.5	0.6580	0.3417	2918
D0.5	0.6563	0.3434	2837
D1	0.6561	0.3436	2825
D1.5	0.6567	0.3430	2856
D2	0.6567	0.3430	2854
D2.5	0.6575	0.3422	2893
TG0.5	0.6580	0.3418	2915
TG1	0.6555	0.3441	2801
TG1.5	0.6570	0.3428	2866
TG2	0.6567	0.3430	2852
TG2.5	0.6570	0.3427	2868

The calculated CCT values of all the samples are given in **Table 7.5**. The determined CCT values lie in the range 2800-3100 K, which are less than 5000 K, indicating warm white light. Thus, these are suitable phosphors for the fabrication of various solid-state optical and display devices. Moreover, among all the samples, the photometric parameters are higher for PVP assisted Gd_2O_3:4mol%Eu samples. This represents the better luminescent properties of the phosphors synthesized using PVP templates.

References

1 G. Li, Y. Liang, M. Zhang and D. Yu, *CrystEngComm*, 2014, **16**, 6670–6679.

2 N. Dhananjaya, H. Nagabhushana, B. M. Nagabhushana, B. Rudraswamy, S. C. Sharma, D. V. Sunitha, C. Shivakumara and R. P. S. Chakradhar, *Spectrochim. Acta - Part A Mol. Biomol. Spectrosc.*, 2012, **96**, 532–540.

3 Y. Liu, Y. Ruan, L. Song, W. Dong and C. Li, *J. Alloys Compd.*, 2013, **581**, 590–595.

4 F. Li, L. Li, C. Guo, T. Li, H. Mi Noh and J. H. Jeong, *Ceram. Int.*, 2014, **40**, 7363–7366.

5 Y. Zhang, Q. Cui, Z. Wang, G. Liu, T. Tian and J. Xu, *Front. Mater. Sci.*, 2016, **10**, 328–333.

6 D. Kumar, M. Sharma and O. P. Pandey, *AIP Conf. Proc.*, 2013, **1536**, 119–120.

7 T. R. Jeena, A. Moses Ezhil Raj and M. Bououdina, *Mater. Res. Express*, 2017, **4**, 025019.

8 S. Som, S. Das, S. Dutta, H. G. Visser, M. K. Pandey, P. Kumar, R. K. Dubey and S. K. Sharma, *RSC Adv.*, 2015, **5**, 70887–70898.

9 K. Lee, Y. Bae and S. Byeon, *Bull. Korean Chem. Soc*, 2008, **29**, 2161–2168.

10 O. Meza, E. G. Villabona-Leal, L. A. Diaz-Torres, H. Desirena, J. L. Rodríguez-López and E. Pérez, *J. Phys. Chem. A*, 2014, **118**, 1390–1396.

11 D. Hreniak, W. Strek, J. Amami, Y. Guyot, G. Boulon, C. Goutaudier and R. Pazik, *J. Alloys Compd.*, 2004, **380**, 348–351.

12 R. Priya and O. P. Pandey, *J. Lumin.*, 2019, **212**, 342–353.

13 S. Hazarika, N. Paul and D. Mohanta, *Bull. Mater. Sci.*, 2014, **37**, 789–796.

14 Y. Zou, L. Tang, J. L. Cai, L. T. Lin, L. W. Cao and J. X. Meng, *J. Lumin.*, 2014, **153**, 210–214.

15 J. M. Chem, Z. Xu, Y. Gao, T. Liu, L. Wang and J. Lin, *J. Mater. Chem.*, 2012, **22**, 21695–21703.

16 D. Kumar, M. Sharma, D. Haranath and O. P. Pandey, *J. Alloys Compd.*, 2017, **695**, 726–736.

17 Y. S. Vidya, K. S. Anantharaju, H. Nagabhushana and S. C. Sharma, *J. Alloys Compd.*, 2015, **619**, 760–770.

18 S. Jeet and O. P. Pandey, *Vacuum*, 2019, **161**, 119–124.

19 E. Pavitra and J. S. Yu, *Mater. Lett.*, 2013, **90**, 134–137.

20 Y. Zhai, M. Wang, Q. Zhao, H. Yang and H. Ding, *J. Mater. Sci. Mater. Electron.*, 2015, **27**, 279–285.

21 M. Venkataravanappa, H. Nagabhushana, B. D. Prasad, G. P. Darshan and R. B. Basavaraj, *Ultrason. - Sonochemistry*, 2017, **34**, 803–820.

22 G. Wu, L. Zhang, B. Cheng, T. Xie and X. Yuan, *J.AM. CHEM. SOC.*, 2004, **126**, 5976–5977.

23 M. Venkataravanappa, H. Nagabhushana, G. P. Darshan, B. D. Prasad and G. R. Vijayakumar, *Ultrason. - Sonochemistry*, 2016, **33**, 226–239.

24 R. A. Mir, P. Sharma and O. P. Pandey, *Sci. Rep.*, 2017, **7**, 1–12.

25 K. M. Koczkur, S. Mourdikoudis, L. Polavarapu and S. E. Skrabalak, *Dalt. Trans.*, 2015, **44**, 17883–17905.

26 A. G. Meguerdichian, A. Shirazi-amin, E. Moharreri, L. A. Achola, S. C. Murphy, J.

Macharia, W. Zhong, T. Jafari and S. L. Suib, *Inorg. Chem.*, 2018, **57**, 6946–6956.
27 D. Walsh, L. Arcelli, T. Ikoma, J. Tanaka and S. Mann, *Nat. Mater.*, 2003, 2, 386–390.
28 A. S. Ethiraj and D. J. Kang, *Nanoscale Res. Lett.*, 2012, **7**, 1–5.
29 N. Dhananjaya, H. Nagabhushana, S. C. Sharma, B. Rudraswamy, C. Shivakumara and B. M. Nagabhushana, *J. Alloys Compd.*, 2014, **587**, 755–762.
30 N. Dhananjaya, H. Nagabhushana, B. M. Nagabhushana, B. Rudraswamy, C. Shivakumara and R. P. S. Chakradhar, *Phys. B Condens. Matter*, 2011, **406**, 1639–1644.
31 G. Xia, S. Wang, S. Zhou and J. Xu, *Nanotechnology*, 2010, **21**, 345601.
32 D. Yang, G. Li, X. Kang, Z. Cheng, C. Peng, H. Lian and J. Lin, *Nanoscale*, 2012, **4**, 3450–3459.
33 S. Majeed and S. Shivashankar, *J. Mater. Chem. C*, 2014, **2**, 2965.
34 J. Tauc, R. Grigobovici and A. Vancu, *Phys. Stat. Sol.*, 1966, **15**, 627–637.
35 G. Seeta Rama Raju, E. Pavitra, G. Nagaraju and J. S. Yu, *Dalt. Trans.*, 2015, **44**, 1790–1799.
36 A. P. de Moura, L. H. Oliveira, I. C. Nogueira, P. F. S. Pereira, M. S. Li, E. Longo, J. A. Varela and I. L. V. Rosa, *Adv. Chem. Eng. Sci.*, 2014, **04**, 374–388.
37 V. R. Bandi, B. K. Grandhe, K. Jang, H. S. Lee, D. S. Shin, S. S. Yi and J. H. Jeong, *J. Alloys Compd.*, 2012, **512**, 264–269.
38 R. Priya, O. P. Pandey and S. J. Dhoble, *Opt. Laser Technol.*, 2021, **135**, 106663.
39 C. S. McCamy, *Color Res. Appl.*, 1992, **17**, 142–144.

CHAPTER 8
CONCLUSIONS AND FUTURE SCOPE

Overview

This chapter summarizes the results obtained in Chapters 4, 5, 6, and 7. The conclusions drawn from the results obtained due to variation in synthesis parameters, co-doping of alkali and alkaline-earth metals, and use of different surfactants/templates on the structural, morphological, optical properties of Gd_2O_3:Eu phosphors are presented in this chapter. Based on the conclusions drawn from different observations in this work, some suggestions for future work to be done in this field are given at the end of the chapter.

8.1 Conclusions

In the proposed thesis work, Gd_2O_3 doped with Eu^{3+} ions were successfully synthesized via a simple, facile, efficient, and economic co-precipitation route by varying various synthesis parameters. It was observed that the samples synthesized at pH=8 had irregular morphology, while samples prepared at pH=10 had uniform rod-like morphology. The as-synthesized products were hydroxides of the metal ions, which upon calcination at higher temperatures transformed to pure cubic Gd_2O_3 phase. It was observed that maximum PL intensity was observed for samples that were synthesized at pH=10 and calcined at 800 ℃. The enhanced PL was observed because of the uniform morphology and defect-free surface under these synthesis conditions.

The concentration of the europium ions in the Gd_2O_3 was varied from 1 to 5 mol%, and the maximum PL was obtained for 4 mol% concentration of europium ions, after which concentration quenching occurred. The main reason behind the concentration quenching was observed to be dipole-dipole interactions among the Eu^{3+} ions. Since the maximum PL was observed for 4mol% of Eu^{3+} ions in Gd_2O_3 lattice, alkali metal ions (Li^+, Na^+, and K^+) in varying molar ratios were co-doped in Gd_2O_3:4mol%Eu to study the PL variation beyond the concentration quenching. The incorporation of the alkali metal ions did not alter the crystal structure and morphology of the Gd_2O_3:4mol%Eu phosphors. However, change in the crystal lattice parameter, and the dimensions of the rods were observed in the co-doped samples. It was found that luminescent intensity was enhanced with the incorporation of the alkali metal ions. This was due to creation of oxygen vacancies by alkali metal ions due to charge imbalance and difference in ionic radii. Moreover, structural parameters were also changed, which influenced the strength of the crystal field around the metal-ligand bond. The maximum intensity for Li^+, Na^+, and K^+ co-doped Gd_2O_3:4mol%Eu was found to be at 5, 3, and 2 mol%, respectively. The luminescent intensity was enhanced by a factor of 1.75, 1.56, and 1.32 times in the case of Li^+, Na^+, and K^+ co-doped Gd_2O_3:4mol%Eu samples, respectively, as compared to Gd_2O_3:4mol%Eu samples. Judd-Ofelt parameters were calculated. The value of Ω_2 was found to be greater than Ω_4 for all the samples, and the stimulated emission cross-section was more for $^5D_0 \rightarrow {}^7F_2$ transition. CIE coordinates of Gd_2O_3:4mol%Eu lie in the red region, and after alkali metal co-doping, the coordinates fall in the deep-red region as the color purity improved with alkali metal ions co-doping. The spectroscopic investigations and photometric calculations indicate that synthesized samples are highly suitable for red light component in white light-emitting diodes.

Further, in continuation of the work, alkaline-earth metal (Mg^{2+}, Ca^{2+}, Sr^{2+}, and Ba^{2+}) ions were co-doped in Gd_2O_3:4mol%Eu phosphors. The co-doping of alkaline-earth metals also did not alter the crystal structure of the Gd_2O_3 matrix, although variation in the crystal structure parameters was observed due to the different ionic radii of the co-doped and host matrix ions. The micrographs of the co-doped samples confirmed the rod-like morphology of all the co-doped samples. The PL intensity was also enhanced in the alkaline-earth metal co-doped samples. The maximum PL intensity was found at 5, 4, 2, and 2 mol% for Mg, Ca, Sr, and Ba co-doped Gd_2O_3:4mol%Eu samples, respectively. The luminescent intensity was enhanced by 1.85, 1.57, 1.48, and 1.47 times in the case of Mg, Ca, Sr, and Ba co-doped Gd_2O_3:4mol%Eu samples, respectively. Judd Ofelt and other radiative parameters were higher for co-doped samples. The CIE coordinates were found to lie in the deep-red region. The maximum PL intensity was observed in case of Mg^{2+} and Li^{+} co-doped Gd_2O_3:4mol%Eu phosphors. The results inferred that other co-dopants can be effectively used to improve luminescent intensity.

The aforementioned studies have shown that the doping concentration of the dopants and co-dopants affect the PL intensity of phosphors by a significant margin. The PL intensity of the phosphors also depends on many other factors such as shape, size, presence of defects, crystal structures, and so on. To alter the morphology of Gd_2O_3:Eu phosphors, different surfactants and templates were used. The concentration of the Eu^{3+} ions was fixed 4 mol% in the Gd_2O_3 host lattice to investigate the effect of surfactants/templates only. For this purpose, cetyltrimethylammonium bromide (CTAB) and trioctylphosphine oxide (TOPO) were used as surfactants in varying the molar ratio of metal ions to surfactants (1:0.5, 1:1, 1:2) during synthesis. Also, crystal structure of the phosphors remained the same, while crystallite size decreased with the use of surfactants. The surfactants were found to have a large impact on morphological features. The micrographs of the samples revealed that CTAB assisted samples were agglomerated and non-uniform in shape as compared to TOPO assisted samples, which were almost in rod shape and mono-dispersed. The introduction of the TOPO during synthesis improved the crystallinity, decreased surface defects and less agglomeration when compared to surfactant-free and CTAB assisted samples. The maximum intensity was observed in the samples in which the metal ion to TOPO ratio was 1:0.5. The luminescent intensity enhanced several folds with the use of surfactants, and CIE coordinates were close to the ideal red color coordinates.

Further, the shape and size of the Gd_2O_3:Eu phosphors were altered using three water-soluble soft templates, i.e., Polyvinylpyrrolidone (PVP), Dextran, and 1-Thioglycerol (TG)

during synthesis. The amount of the templates was varied from 0.5 to 2.5 wt%. The crystal structures of the samples synthesized using PVP and Dextran had a pure cubic phase, while the samples which were synthesized using TG had few peaks of monoclinic phase along with cubic-Gd_2O_3. The morphological results inferred that the samples synthesized using PVP were having rod-like morphology, except for the variation in the dimensions with varying amounts of PVP content during synthesis. However, the samples synthesized using Dextran and TG had quasi-spherical and hexagonal particles. The use of these templates totally changed the shape and morphology of the particles. The extent of the agglomeration also increased with the increasing amount of these templates. The maximum PL intensity for PVP, Dextran, and TG assisted samples were found for 2, 1, and 1 wt% concentration of these templates, respectively. The maximum intensity was found for PVP template-directed samples and less in the case of TG directed samples. The enhanced intensity in the case of PVP assisted sample was observed because of uniform morphology, less agglomeration, and pure phase Gd_2O_3. However, in the case of TG and Dextran directed Gd_2O_3:4mol%Eu samples, the agglomeration increased with the increasing amount of these templates. The presence of a minor monoclinic Gd_2O_3 phase, which inferred the PL characteristics of Gd_2O_3:4mol%Eu was also observed. The photometric parameters were also higher for PVP directed Gd_2O_3:4mol%Eu phosphors.

In brief, the main aim of the proposed thesis work was to synthesize uniform, pure phase, and highly intense Gd_2O_3:Eu phosphors. All the doped, co-doped, and surfactant/template assisted Gd_2O_3:Eu phosphors were synthesized using facile, efficient, and high yield co-precipitation route. The doping concentration and calcination temperatures had significant impacts on the luminescent intensity of Gd_2O_3:Eu. The incorporation of the alkali and alkaline-earth metal ions enhanced the PL intensity by several folds. The properties of the phosphors were engineered with the aid of surfactants/templates. They had affected the crystal structure, morphology, and optical properties of Gd_2O_3:Eu phosphors in different ways. The as-synthesized phosphors exhibited better luminescent properties and hold potential applications in optoelectronic devices and biomedical applications.

8.2 Future Scope

In the present work, different parameters were optimized to enhance the luminescent properties of Gd_2O_3:Eu phosphors. There are still possibilities for future work that can be undertaken. It is observed that the alkali and alkaline-earth metal co-doped Gd_2O_3:Eu exhibited enhanced photoluminescence. The transition metal ions co-doping can also be investigated to study their impact on the luminescent features of Gd_2O_3:Eu via different energy mechanisms. Gd_2O_3:Eu is also a paramagnetic material. This dual paramagnetic and luminescent behavior of Gd_2O_3:Eu phosphors can be investigated for various biomedical applications such as bio-imaging, MRI, in-vivo and in-vitro studies. In the present study, surfactants such as CTAB and TOPO and templates such as PVP, Dextran, and TG were used to alter the morphological features of Gd_2O_3:Eu phosphors and their influence on the luminescent properties. Other surfactants or templates can be considered to modify the dimensionality, shape, and size of the Gd_2O_3:Eu. The core-shell and hetero-structures of Gd_2O_3:Eu can be developed for various optoelectronic and biomedical device applications. Gd_2O_3:Eu is a pristine red light-emitting phosphor. It can be incorporated in the different glass matrix to form scintillating glasses. The samples can be irritated under different radiations like UV, β, and γ to investigate their effect on the optical and morphological variations of Gd_2O_3:Eu phosphors.